SSSTJ
VOL.9 NO.2
July 2022
ISSN 2351-0889

SSSTJ

Suan Sunandha Science and Technology Journal
Volume 9, Number 2, July 2022

Suan Sunandha Science and Technology Journal
©2022 Faculty of Science and Technology, Suan Sunandha Rajabhat University

General Information

The Suan Sunandha Science and Technology Journal (SSSTJ) is a double-blind peer reviewed (at least two reviewers) scientific journal published twice a year (January and July) by the Faculty of Science and Technology, Suan Sunandha Rajabhat University. Submissions of manuscripts should be sent to the Editor of the SSSTJ by online system: http://www.ssstj.sci.ssru.ac.th. The manuscript will be taken that all contributing authors attest that manuscripts and material submitted to the SSSTJ are original and have not been published or submitted elsewhere and the authors concede to the open-access distribution of the manuscript, including all contents contained therein.

Aim and scope:

Suan Sunandha Science and Technology Journal (SSSTJ) is an international academic journal that gains foothold at Suan Sunandha Rajabhat University, Thailand and opens to scientific communications in Southeast Asia, Asia and worldwide. It aims to contribute significant articles in science and technology researches. Published papers are focused on state of the art science and technology. Committee of the journal and association will review submitted papers. The authors may include researchers, managers, operators, students, teachers and developers.

Following areas are considered for publication:

1. Biology
2. Biotechnology
3. Environmental Science and Technology
4. Food Science and Technology
5. Microbiology
6. Applied Science
7. Computer Science and Information Technology
8. Other related fields

QR CODE Journal

Suan Sunandha Science and Technology Journal
©2022 Faculty of Science and Technology, Suan Sunandha Rajabhat University

Editorial Board

Editor-in -Chief

C. Tharasawatdipipat, Suan Sunandha Rajabhat University, Thailand

Editorial Board:

B. Prapagdee, Mahidol University, Thailand

N. Sriubolmas, Eastern Asia University, Thailand

N. Hieu Trung, Can Tho University, Vietnam

S. C. Pandey, Journal of Environmental Research and Development (JERAD), India

S.Kim, Kyungpook**,** National University, Korea

S.Morley, Leicester Royal Infirmary, United Kingdom

S. Roytrakul, National Center for Genetic Engineering and Biotechnology, Thailand

S.Senapin, Mahidol University, Thailand

T. Dao, Vietnam National University, Vietnam

V. Kanokantapong, Chulalongkorn University, Bangkok, Thailand

Y. Lorjaroenphon, Kasetsart University, Thailand

Y. Tsai, Chia Nan University of Pharmacy and Science, Taiwan

Editorial Managers:

K. Poonsilp, Suan Sunandha Rajabhat University, Thailand

K. Thongkao, Suan Sunandha Rajabhat University, Thailand

N. Chamchoi, Suan Sunandha Rajabhat University, Thailand

S. Sansiribhan, Suan Sunandha Rajabhat University, Thailand

T. Chuacharoen, Suan Sunandha Rajabhat University, Thailand

T. Utarasakul, Suan Sunandha Rajabhat University, Thailand

R. Pattanayaiying, Suan Sunandha Rajabhat University, Thailand

Editorial Liaisons:

P. Nitutorn, Suan Sunandha Rajabhat University, Thailand

N. Chewpraditkul, Suan Sunandha Rajabhat University, Thailand

K. Srivareerat, Suan Sunandha Rajabhat University, Thailand

Suan Sunandha Science and Technology Journal
©2022 Faculty of Science and Technology, Suan Sunandha Rajabhat University

SSSTJ Authors Guide

Types of paper:

Full length articles are typically 4 - 10 manuscript pages (including tables, figures, equations and formulas). The articles may cover a variety of topics which are related to science or technology. Articles must use previously published works to support the discussion of a particular subject or topic.

Plagiarism:

Submission of an manuscript implies that the work described has not been published previously (except in the form of an abstract or as part of a published lecture or academic thesis), that it is not under consideration for publication elsewhere, that its publication is approved by all authors and tacitly or explicitly by the responsible authorities where the work was carried out, similiarity idex not more than 30% and that, if accepted, it will not be published elsewhere in the same form, in English or in any other language, without the written consent of the copyright-holder.

Articles and any other materials published in the SSSTJ should be the opinions of the author(s) and should not be construed to reflect the opinions of the editor(s) or the publisher. Manuscripts that do not meet the general criteria or standards for publication in the SSSTJ will be immediately returned to the authors, without detailed review. At their discretion, editors may request from the corresponding author a statement describing specific original contributions made by each co-author.

Ethics in publishing:

By submitting this manuscript, the authors agree that text, equations, or figures from previously published articles or books have been clearly identified in full and their origin clearly explained in the adjacent text, with appropriate references given at the end of the paper. Duplication of text is rarely justified, even with diligent referencing. Exceptions may be made for descriptions of standard experimental techniques, or other standard methods used by the author in the investigation; but an appropriate citation is preferable. Authors who duplicate material from their own published work in a new article, without clearly identifying the repeated material and its source as outlined above, are self-plagiarising.

Manuscript submission:

For submission of all manuscripts, follow the instructions of the online submission system. Hard copy submissions cannot be accepted. Before submission, prepare and keep ready all information on the manuscript (title, full name and affiliation of all authors, corresponding author email, abstract, name of all files to be submitted).The author submitting the manuscript will be the corresponding author. Manuscripts are accepted only in American English. All submitted articles should report original, previously unpublished research results, experimental or theoretical, and will be peer-reviewed.

Role of the funding agency:

You are requested to identify who provided financial support for conducting the research and/or preparation of the article and to briefly describe the role of the sponsor(s), if any, in study design; in the collection, analysis and interpretation of data; in the writing of the report; and in the decision to submit the article for publication. If the funding source(s) had no such involvement then this should be stated.

Suan Sunandha Science and Technology Journal
©2022 Faculty of Science and Technology, Suan Sunandha Rajabhat University

Journal access:

Open access:

- Articles are freely available to both subscribers and the wider public.
- Articles are made available to subscribers at http://www.ssstj.sci.ssru.ac.th.

Regardless of how you choose to publish your article, the journal will apply the same peer review criteria and acceptance standards.

Peer review:

All published journal papers are refereed by the international competent researchers and scientists. Therefore, a full double - blind international refereeing process is used in which 1) Papers are sent to reviewers for their peer review process. 2) The reviewers' recommendations determine whether a paper will be accepted / accepted subject to change / subject to resubmission with significant changes/rejected.

For papers which require changes, the same reviewers will be used to ensure that the quality of the revised paper is acceptable. All papers are refereed, and the Editor-in-Chief reserves the right to refuse any typescript, whether on invitation or otherwise, and to make suggestions and/or modifications before publication.

Additional information:

Manuscripts must be submitted by the senior author, who must accept responsibility on behalf of all authors for all ethical requirements. The author submitting the manuscript will be listed as the corresponding author in the published version of each accepted manuscript. There are no submission fees or page charges.

Revised manuscripts should be returned including revision notes. The revision notes should address the issues raised in the referee report and clearly state per page (indicate paragraph and line) which changes have been made. Additional materials may be requested at the discretion of the editor. Authors requested to revise their submission to SSSTJ will be given 4 weeks in which to submit the revised submission. Revised submissions received after 4 weeks from the time at which the revision was requested will be considered as new submissions.

References:

There are no strict requirements on reference formatting at submission. But the authors are expected to follow the American Psychological Association (APA 6th edition) style. Where applicable, author(s) name(s), journal title/book title, chapter title/article title, year of publication, volume number/book chapter and the pagination must be present. Use of DOI is highly encouraged.

Article structure:

Subdivision - numbered sections

Divide your article into clearly defined and numbered sections. Subsections should be numbered 1.1, 1.2, etc. (the abstract is not included in section numbering). Use this numbering also for internal cross-referencing: do not just refer to 'the text'. Any subsection may be given a brief heading. Each heading should appear on its own separate line.

Suan Sunandha Science and Technology Journal
©2022 Faculty of Science and Technology, Suan Sunandha Rajabhat University

Article formatting:

Full-length articles published in the SSSTJ should include a title, the author's name, the author's address, the corresponding author email, Abstract, Introduction, Materials and Methods, Results and Discussion, Acknowledgements and References.

- **Font:** Times New Roman (headings 11pt and normal text 10pt)
- **Title:** Concise and informative. This should briefly summarize the scope of the article. Avoid abbreviations and formulas where possible. The title should be centered at the top of the page. e.g., Notes on the Biology of *Varanus semiremix*
- **Authors name and affiliation:** The full names referenced by numerical superscripts with affiliation and addresses of all authors, and the full address of the corresponding author. The name of the corresponding author along with phone, fax and e-mail information. e.g.

  Author's Name
  Author's affiliation
  Author's address
  Corresponding author email
- **Corresponding author:** Clearly indicate who will handle correspondence at all stages of refereeing and publication, also post-publication. Ensure that the e-mail address is given and that contact details are kept up to date by the corresponding author.
- **Abstract:** The abstract should contain brief information on purpose, methods, results and conclusion (without subheadings). It indicates significant data, and point out major findings and conclusions. Provide 200 – 250 words in length.
- **Keywords:** 3 – 6 keywords should be listed.
- **Introduction**: The introduction should provide sufficient background knowledge and information to allow the reader to understand and evaluate the value of the study. It must also supply a rationale for the study. Cite references to provide the most salient background rather than an exhaustive review of the topic.
- **Materials and Methods:** Specific details about materials, instrumentation and experimental protocols should be given here. This section should contain sufficient details so that others are able to reproduce the experiment(s). The source of special equipment or chemicals should also be given with the name and location of manufacturers, e.g. (Merck, Germany) or (Sigma, USA). Techniques previously published or standardized can be simplified by literature citations. The statistical procedures used should be explained. Primary headings for this section are in bold, indented, with numbering. The text is run from a new line under the heading with an indentation.
- **Results and Discussions:** The results should be presented with clarity and precision. The discussions should provide an interpretation of the data and relate them to existing knowledge. Emphasis should be given to important new findings and new hypotheses should be described clearly. This section may be subdivided and headed as in the Materials and Methods section. At the end of this section, the authors should state the conclusion in a few sentences.
- **Conclusion:** The main conclusions of the study may be presented in a short conclusion section, which may stand alone or form a subsection of a Results and Discussions section.
- **Acknowledgment:** The acknowledgments should be stated in separate section at the end of the article before the references.

Suan Sunandha Science and Technology Journal
©2022 Faculty of Science and Technology, Suan Sunandha Rajabhat University

- **References:** Please make sure that every reference cited in the text is also present in the reference list and vice versa.
- **Appendices (optional):** If there is more than one appendix, they should be identified as A, B, etc. Formulae and equations in appendices should be given separate numbering: Eq. (A.1), Eq. (A.2), etc.; in a subsequent appendix, Eq. (B.1) and so on. Similarly for tables and figures: Table A.1; Figure. A.1, etc.

  Tables and Figures:

  Tables: Please submit tables as editable text and not as image. Tables must be embedded into text. Headings should be in bold letters, and aligned in the text left. Vertical lines are not used. A table should not exceed one page when printed. Use lower case letters in superscripts a, b, c ... for special remarks.

  Figure legends: It should be typed in numerical order. Begin each legend with a title and include sufficient description so that the figure is understandable without reading the text of the manuscript.

  Figures: Each figure must be embedded into text. It should be prepared using applications capable of generating high resolution TIFF, JPEG, PNG.

  - Color or grayscale photographs: minimum of 300 dpi
  - Bitmapped line drawings: minimum of 1000 dpi
  - Combination bitmapped line (color or grayscale photographs: minimum of 500 dpi)
  - Headings should be in bold letters, and aligned in the text Centre

Checklist before submission:

The following list will be useful during the final checking of an article prior to sending it to the journal for review.

Ensure that the following contents are present:

One author has been designated as the corresponding author with contact details:

- E-mail address
- Affiliation
- Full postal address
- Corresponding author email

All necessary files have been uploaded, and contain:

- Keywords
- All figure captions
- All tables (including title, description)
- Manuscript has been 'spell-checked' (Spellchecker tool of MS word) and 'grammar-checked'.
- All references mentioned in the reference list are cited in the text, and vice versa.

Additional information:

For additional information regarding format, content, submissions, or authoring guidelines, please contact the editor (e-mail: ssstj.contact@gmail.com).

Suan Sunandha Science and Technology Journal
©2022 Faculty of Science and Technology, Suan Sunandha Rajabhat University

Proofs:

Proofs will be sent to the author and should be promptly returned to the editor. A total of 200 copies of each issue of the journal will be printed. Authors will receive pdf files of their article.

Biannual
ISSN 2351-0889
Subject: Science and Technology
Published by: Faculty of Science and Technology, Suan Sunandha Rajabhat University

SUAN SUNANDHA SCIENCE AND TECHNOLOGY JOURNAL

Suan Sunandha Rajabhat University, Faculty of Science and Technology
1 U-thong Nok Road, Dusit, Bangkok 10300 THAILAND

CONTENTS

July 2022, Volume 9, No.2

Available online at http://www.ssstj.sci.ssru.ac.th

Suan Sunandha Science and Technology Journal
©2022 Faculty of Science and Technology, Suan Sunandha Rajabhat University

Preparation, Characterization and Antiradical Activity of Zinc Oxide Nanoparticles

Kanyarat Kumnoedauy[1], Pattareeya Damrongsak[1], Kitsakorn Locharoenrat[1], Badin Damrongsak[2*]

[1]Biomedical Physics Research Unit, Department of Physics, Faculty of Science, King Mongkut's Institute of Technology Ladkrabang, Bangkok, 10520, Thailand

[2]Department of Physics, Faculty of Science, Silpakorn University, Nakornpathom, 73000, Thailand

***Corresponding author e-mail: badin@rocketmail.com**

Received: *9 February 2022* / **Revised**: *27 April 2022* / **Accepted:** *26 May 2022*

Abstract

Zinc oxide nanoparticles (ZnO NPs) have recently been studied as a multi-functional and multi-target nanomedicine for cancer treatment. They can be used not only as a nanocarrier for delivery of the chemotherapy drug but also as an antiradical agent due to their photo-catalytic and photo-oxidizing abilities. Our previous work showed a potential use of commercial-available ZnO NPs without and with carboplatin for the treatment of retinoblastoma. The aim of this work was to synthesize ZnO NPs having smaller particle size than the commercial ones, i.e., 100 nm average diameter, in order to improve the reaction time. ZnO NPs were prepared by a sol-gel technique and calcined with different calcination conditions. The structure and particle size of ZnO powders were characterized using an x-ray diffractometer and a particle size analyzer. Average nanoparticle sizes of 16.32 ± 1.64 nm were achieved at a calcination temperature of 300 degree Celsius and 1 hour holding time. The antiradical activity of prepared ZnO NPs in cooperation with ultraviolet irradiation was assessed using a putative model of cancer cells, i.e., 2,2(diphenyl-1-picryhydrazyl) radicals (DPPH*). An optical spectroscopy was used to detect the decrease in peak absorbance of the antiradical solution at a wavelength of 515 nm, which in turn can be used to calculate the percent remaining of DPPH*. The disappearance of DPPH* with respect to the reaction time revealed that prepared ZnO NPs (16.32 ± 1.64 nm) improved response time as compared with ZnO NPs (100 nm). Moreover, the effective ZnO concentrations to reduce the initial DPPH* concentration by 50%, also known as the EC50 value in the present study, is lower indicating the improvement of anti-proliferative activity when compared to the commercial ZnO NPs.

Keywords: Antiradical, DPPH, Sol-gel, ZnO nanoparticles

1. Introduction

Zinc oxide nanoparticles (ZnO NPs) are a wide band gap semiconductor with a particle size less than 100 nm. They are one of the most abundant metal oxides, making them relatively inexpensive. ZnO NPs have, moreover, been proven non-toxic and safe to be used in food and drugs, approved by FDA (The US Food and Drug Administration). Therefore, they have received an extensive research for a long period in wide varieties of applications, from semiconductor devices (Bhati, Hojamberdiev, & Kumar, 2020; Narayana et al., 2020; Rahman, 2019; Shashanka, Esgin, Yilmaz, & Caglar, 2020) and cosmetic products (Awan et al., 2018; Nguyen, Nguyen, Le, & Le, 2020) to biomedical applications (da Silva, Caetano, Chiari-Andreo, Pietro, & Chiavacci, 2019; Martínez-Carmona, Gun'ko, & Vallet-Regi, 2018; Mishra, Mishra, Ekielski, Talegaonkar, & Vaidya, 2017;). Currently, ZnO NPs play a significant role in modern anticancer applications (Bisht & Rayamajhi, 2016; Chen et al., 2019; Singh, Das, & Sil, 2020; Wahab et al., 2014). They not only show relatively high biocompatibility but also selective cytotoxicity against cancerous cells.

It was reported that the cytotoxicity of ZnO NPs is size-dependent. The nanoparticles with a diameter below 10 nm can penetrate more deeply in tumors and affect the cell viability; however, these small-diameter ZnO NPs can penetrate and cause toxicity to normal tissues as well. The target size for ZnO NPs is in a range of 10 – 100 nm, which is considered suitable for biomedical applications. Several methods have been studied to prepare the ZnO NPs (Devi & Velu, 2016; Manikandan, Endo, Kaneko, Murali, & John, 2018; Wallace, Brown,

Suan Sunandha Science and Technology Journal
©2022 Faculty of Science and Technology, Suan Sunandha Rajabhat University

Brydson, Wegner, & Milne, 2013; Wasly, Abd El-Sadek, & Henini, 2018). Among them, a chemical sol-gel process has many advantages due to ease of synthesis, cost-effectiveness and excellent homogeneity and purity. The most common precursors for synthesis of ZnO NPs are zinc acetate dihydrate, methanol and sodium hydroxide. It was reported that the size of ZnO NPs was affected by the variation in pH value of the solution (Alias, Ismail, & Mohamad, 2010). The particle size was found to decrease with an increase in the pH value.

The most widely used method for evaluating the antiradical properties of ZnO NPs is by scavenging free radicals of 2,2–diphenyl–1–picrylhydrazyl hydrate (DPPH*) with varying the concentration of the nanoparticles (Brand-Williams, Cuvelier, & Berset, 1995). UV-visible spectrometry is typically employed to measure the absorbance of the mixtures as the indirect measurement of the antiradical activity.

In our previous study (Pairoj et al., 2019), the antiradical performance of commercial ZnO NPs was investigated for being used as an anticancer drug for retinoblastoma treatment. The results showed that the nanoparticles alone had low antiradical efficiency and the number of reduced DPPH* increased by applying UV illumination. In this work, we aimed to prepare ZnO NPs with a diameter less than 100 nm (the size of the commercially available ZnO NPs) in order to improve the antiradical activity. The sol-gel method was chosen to synthesize ZnO NPs. The synthesized NPs were characterized and compared with those results obtained from the commercially available nanoparticles.

2. Materials and Methods

2.1 Materials

Precursors used for the formation of the zinc oxide nanoparticles were zinc acetate dihydrate ($Zn(CH_3COO)_2 \cdot 2H_2O$) with ≥ 99.5% purity and sodium hydroxide (NaOH) with ≥97% purity. Both were purchased from KemAus. Sodium hydroxide was used to control the pH of the solution. Methanol (> 99.9%, from Labsupplies) was used as a reagent and DI water was used for dilution.

2.2 Methods

(1) Synthesis of ZnO NPs

The ZnO sols were prepared by adding 0.15 M ($Zn(CH_3COO)_2 \cdot 2H_2O$) to methanol at room temperature. The solution was stirred at a temperature of 70°C for 90 min using a magnetic stirrer until a clear solution without turbidity was obtained. The pH level of the solution affects the particle size of synthesized ZnO powders (Alias et al., 2010; Rani, Suri, Shishodia, & Mehra, 2008). Therefore, the prepared solution was adjusted to the pH value of 10 by adding 1.5 M NaOH, aiming to control the size of ZnO particles close to 10 nm. The resulting milky white gel was then stirred at a temperature of 70°C for 60 minutes. After this process, the sol was centrifuged for 15 minutes at 5000 rpm. The sample was washed with a 40:60 mixture of DI water and ethanol in order to remove organic materials left on the surface of synthesized ZnO powders. The sediment was dried at 100°C for 8 hours. Finally, the dried precipitate was calcined in air at 300°C for 60 minutes.

(2) Physical characterization

The crystal structure of the synthesized samples was determined by the Rigaku X-ray diffractometer (XRD). The X-ray source of Cu Kα radiation, having the monochromatic wavelength of 1.5406 Å, was used. The diffraction pattern was recorded in the range of 20-80° for the ZnO samples. The XRD results were compared to the Joint Committee on Powder Diffraction Standards (JCPDS) data file. The crystallite size of the samples was estimated using the Scherrer formula:

$$d_{XRD} = \frac{K\lambda}{Bcoscos\,\theta} \qquad (1)$$

where d_{XRD} is the average diameter of nanoparticles, K is a shape factor (0.9 for spherical particles), λ is the wavelength of X-ray source (1.5406 Å), B is the line broadening of the strong XRD peak (101) at half its peak height, and θ is the Bragg angle.

(3) Determination of antiradical activity

The antiradical activity of the prepared ZnO NPs was determined by a spectrophotometric method, also called DPPH method. In this method, a solution of 2,2-diphenyl-1-picrylhydrazyl (DPPH*) was used as the putative model of cancer cells (Aruoma & Cuppett, 1997), acting as a free radical source. Prior adding a solution of synthesized ZnO NPs into the solution, the DPPH* the solution had a deep violet color. When a solution of synthesized ZnO NPs was added into the DPPH* solution, the

Suan Sunandha Science and Technology Journal
©2022 Faculty of Science and Technology, Suan Sunandha Rajabhat University

free radicals were scavenged resulting in a change of the color in the solution as shown in Figure 1. This process was quantitatively monitored by measuring the absorbance spectra of the solution using Avantes UV-visible spectrometer.

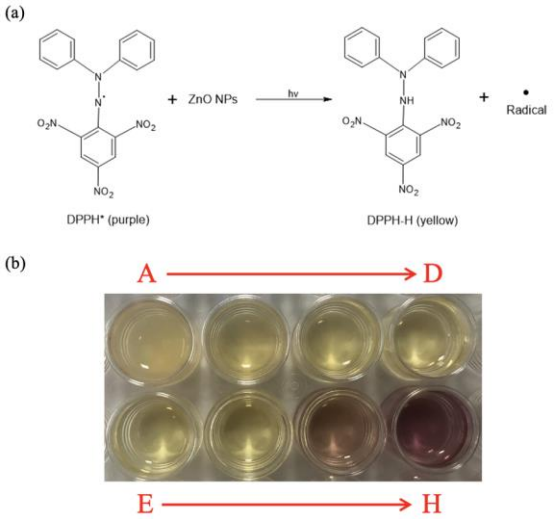

Figure 1. (a) Mechanism of the DPPH* scavenging activity of the ZnO NPs. (Marin-Flores et al., 2021) (b) The color change of DPPH* with respect to the different concentrations of ZnO NPs at 1440 min. A, B, C, D, E, F, G, and H represent 1.000, 0.500, 0.250, 0.125, 0.0625, 0.03125, 0.0156, and 0.0078 mg/ml respectively.

In this experiment, a 100 µM solution of the DPPH* Methanol was prepared and then added with a solution of the synthesized nanoparticles at various concentrations, ranging from 0.0078 to 1.000 mg/ml. The mixture was sonicated for 90 minutes at room temperature. Each mixed solution was illuminated by an 8 W, 254 nm UV lamp (Spectroline: CX-21, Germany) in order to introduce the photoexcitation process. After that, the solution was taken for measuring the absorbance at a peak wavelength of 515 nm for a time duration from 0 to 1440 minutes (no decrease in the absorbance can be observed). The percentage of residual DPPH* with respect to the reaction time was calculated using:

$$\%RemainingDPPH^{*} = \frac{C_{ss}}{C_{is}} \times 100 \qquad (2)$$

where C_{is} and C_{ss} are to concentration of DPPH* at initial state and steady state, respectively. The concentrations of DPPH* were determined by using the linear equation obtained from the calibration curve reported in Pairoj et al., 2019.

$$C_{DPPH^{*}} = (Abs_{515nm} - 0.0132)/0.0072 \qquad (3)$$

3. Results and Discussion

The X-ray diffraction pattern of prepared ZnO NPs was shown in Figure 2. It showed the diffraction peaks at angles of 31.78°, 33.9°, 36.8°, 47.63°, 56.67°, 62.94° and 67.98°, respectively, corresponding to the Bragg reflections (100), (002), (101), (102), (110), (103) and (112) of ZnO having a typical hexagonal wurtzite structure. All peaks were in good agreement with the standard JCPDS file no. 01-084-6784 (Kinnunen, Lahtinen, Arstila, & Sajavaara, 2021). From Scherrer formula, the average crystalline size of the prepared ZnO NPs was 16.32 ± 1.64 nm. The size of the synthesized nanoparticles was approximately 5 times smaller than that of commercial ZnO NPs (Sigma Aldrich, USA having a diameter of 100 nm) which was used as a reference.

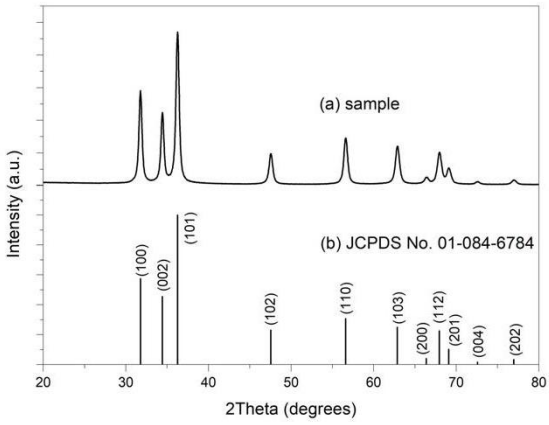

Figure 2. XRD pattern of the synthesized ZnO NPs.

The antiradical activity of prepared ZnO NPs was measured by monitoring the color of the DPPH* solution after adding the ZnO NPs for some period of time until the reaction reaches a steady state. The solution was illuminated by a constant power UV light source at a room temperature. At every 10 minutes, one tube of the samples was taken out in order to measure the absorbance spectrum. Figure 3

Suan Sunandha Science and Technology Journal
©2022 Faculty of Science and Technology, Suan Sunandha Rajabhat University

shows an example of the monitored absorbance spectra for the DPPH* solution in the presence of ZnO NPs with the concentration of 0.25 mg/ml. It can be observed that a peak intensity at 515 nm moderately decreases with time and starts reaching a steady state after 250 minutes. A decrease of the peak absorbance is related to a change in color of the solution, which can be implied that the added ZnO NPs scavenged the free radicals in the DPPH* solution over time. The peak absorbance values at the wavelength of 515 nm were recorded to determine the antiradical activity of the tested ZnO NPs.

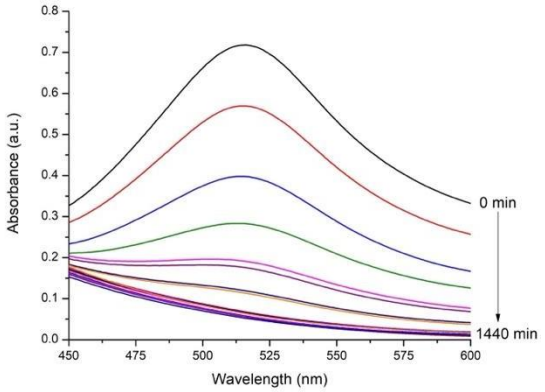

Figure 3. Absorbance spectra for the DPPH* solution in the presence of ZnO NPs with the concentration of 0.25 mg/ml at a different time interval.

The peak absorbance at 515 nm as a function of exposed time for the prepared ZnO NPs with different concentrations was plotted and compared with those obtained from the reference commercial ZnO NPs. For a quantitative comparison, the DPPH* concentration that calculated from equation (3) was plotted against the exposed time in order to estimate the rate of reaction (Rs). For a sake of clarity, only the linear region was considered. The rate of reaction at which the DPPH* concentration decreased over the exposed time can then be estimated from the slope. Figure 4 shows the peak absorbance of the DPPH* solution and DPPH* concentration in the presence of ZnO NPs. The rate of reaction corresponding to the concentration of the synthesized and the reference ZnO NPs was shown in Figure 5. As can be seen, the rate of reaction increases when the nanoparticle concentration increases, having a similar trend for both the ZnO NPs prepared in this work and the commercial ones. The rate of reaction obtained from the nanoparticles in this work, which have much smaller particle size (16 nm), was slightly higher. Interestingly, it was observed that the rate of reaction of the commercial ZnO NPs reached the saturation state when the solution concentration was over 0.25 mg/ml. On the other hand, the smaller size of the prepared ZnO NPs still kept attacking the free radicals even though the concentration was as high as 1 mg/ml.

To summarize, the ability of the free radical scavenging activity of the prepared ZnO NPs was better than the reference nanoparticles. This was due to the relatively smaller size of the prepared nanoparticles, making them be able to penetrate more deeply in the putative model or in our case the DPPH*. In addition, the smaller size leads to a high surface area to volume ratio, which in turn increases a surface contact to the targeted radicals. In addition, under UV irradiation, the prepared nanoparticles were able to release much more amount of toxic Zn2+ ions into the DPPH* due to the large surface area.

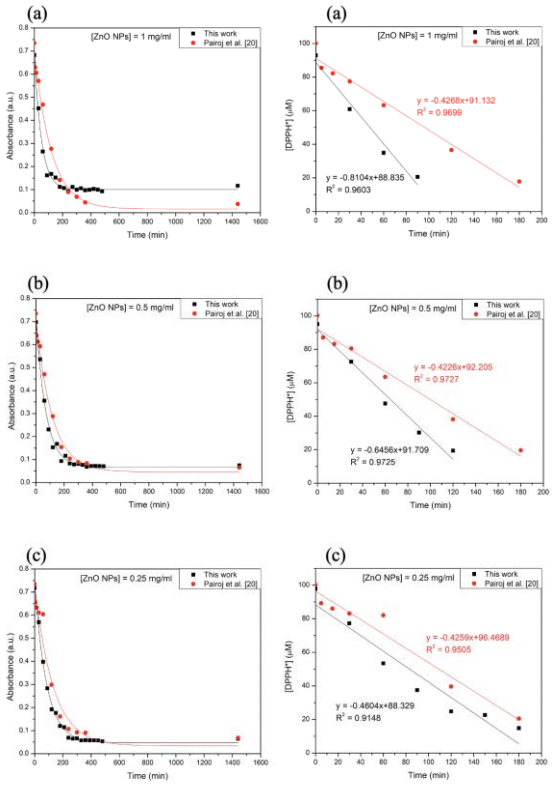

Suan Sunandha Science and Technology Journal
©2022 Faculty of Science and Technology, Suan Sunandha Rajabhat University

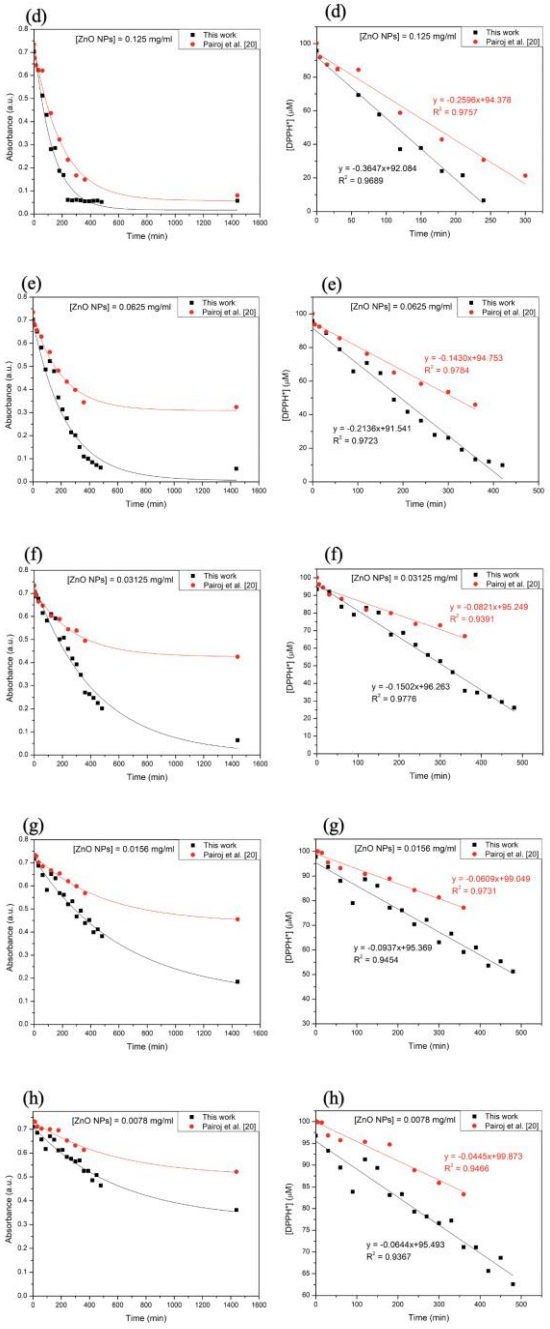

Figure 4. Peak absorbance at 515 nm and DPPH* concentration corresponding to the exposed time for the DPPH* solution in the presence of ZnO NPs with the concentration of (a) 1.000 mg/ml, (b) 0.500 mg/ml, (c) 0.250 mg/ml, (d) 0.125 mg/ml, (e) 0.0625 mg/ml, (f) 0.03125 mg/ml, (g) 0.0156 mg/ml, and (h) 0.0078 mg/ml.

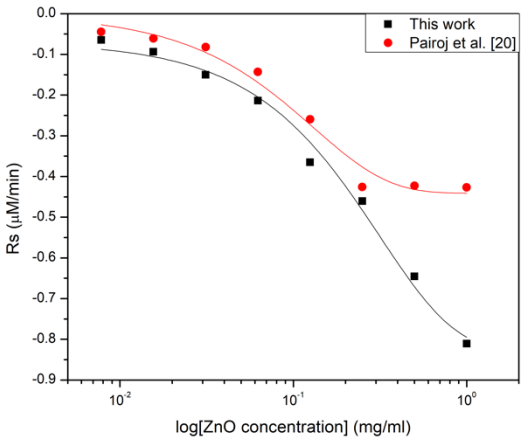

Figure 5. Rate of reaction (Rs) corresponding to the concentrations of ZnO NPs; a black line represents the data from the prepared ZnO NPs in this work, while a red line represents the data obtained from the reference commercial ZnO NPs.

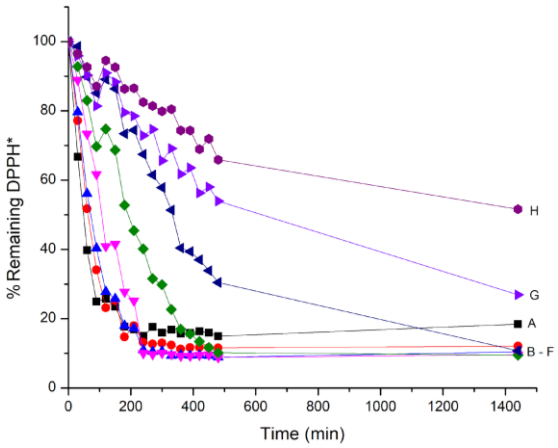

Figure 6. The percentage of residual DPPH* with respect to the reaction time at the different concentration. A, B, C, D, E, F, G, and H represent 1.000, 0.500, 0.250, 0.125, 0.0625, 0.03125, 0.0156, and 0.0078 mg/ml respectively.

Suan Sunandha Science and Technology Journal
©2022 Faculty of Science and Technology, Suan Sunandha Rajabhat University

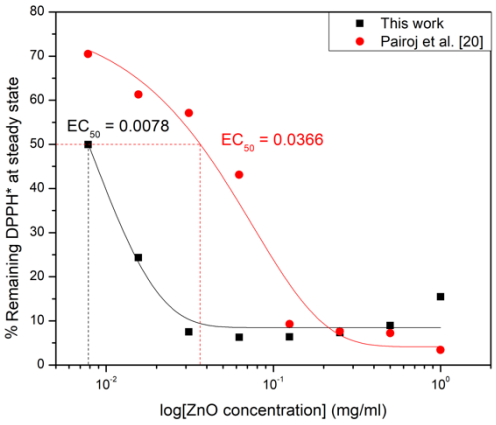

Figure 7. The percentage of residual DPPH* with respect to a mole ratio of antiradical agent to DPPH*. The effective concentration (EC50) value of each antiradical agent is also presented.

In biological studies, a half maximal effective concentration (EC50), which is defined as the concentration of ZnO NPs sample required for a 50% decrease in the DPPH* concentration, is typically used to express and compare the efficiency of the antiradical activity with different other samples. Thus, the amount of residual DPPH* in the presence of the prepared ZnO NPs at different concentrations was calculated using equations (2) and the percent remaining of the DPPH* corresponding to the reaction time was shown in Figure 6. In Figure 7, The percentage of residual DPPH* at a steady state (1440 minutes of the reaction) with regard to the concentration of ZnO NPs was plotted in order to estimate the EC50 value. As can be seen, the EC50 value in this work was approximately 5 times lower than the EC50 obtained from the commercial ZnO NPs. This can be implied that the antiradical activity had significantly improved.

4. Conclusions

ZnO NPs were synthesized by using a sol-gel method. By adjusting the pH of the solution, ZnO NPs with an average particle size of 16.32 ± 1.64 nm were achieved. The free radical scavenging capacity of the ZnO NPs at different concentrations was analyzed using the DPPH test; in this study, the rate of reaction and EC50 value were determined and compared with results obtained from the commercial ZnO NPs used in our previous work. According to the experimental results, the ability of the free radical scavenging activity of the prepared ZnO NPs was significantly improved over the reference nanoparticles. The EC50 value of the ZnO NPs in this work was approximately 5 times better than the results from the commercial ZnO NPs (100 nm in diameter). This was obvious that the relatively smaller size of the prepared ZnO NPs made them penetrating deeper into the DPPH*. Because of the large surface area, the particles had more chance to contact the targeted radicals and, under the UV photoexcitation, were able to produce many toxic Zn^{2+} ions, increasing the antiradical activity.

5. Acknowledgement

Authors would like to thank the National Research Council of Thailand (NRCT), Silpakorn University and King Mongkut's Institute of Technology Ladkrabang for financial support.

6. References

Alias, S. S., Ismail, A. B., & Mohamad, A. A. (2010). Effect of pH on ZnO nanoparticle properties synthesized by sol–gel centrifugation. *Journal of Alloys and Compounds*, *499*(2), 231-237. doi:10.1016/j.jallcom.2010.03.174

Aruoma, O. I., & Cuppett, S. L. (Eds.). (1997). *Antioxidant methodology: In vivo and in vitro concepts*. The American Oil Chemists Society.

Awan, F., Islam, M. S., Ma, Y., Yang, C., Shi, Z., Berry, R. M., & Tam, K. C. (2018). Cellulose nanocrystal–ZnO nanohybrids for controlling photocatalytic activity and UV protection in cosmetic formulation. *ACS Omega*, *3*(10), 12403-12411. doi:10.1021/acsomega.8b01881

Bhati, V. S., Hojamberdiev, M., & Kumar, M. (2020). Enhanced sensing performance of ZnO nanostructures-based gas sensors: A review. *Energy Reports*, *6*, 46-62. doi:10.1016/j.egyr.2019.08.070

Bisht, G. , & Rayamajhi, S. (2016) . ZnO nanoparticles: A promising anticancer agent. *Nanobiomedicine*, *3*. doi:10.5772/63437

Brand-Williams, W., Cuvelier, M. E., & Berset, C. (1995). Use of a free radical method to evaluate antioxidant activity. *LWT-Food Science and Technology*, *28*(1), 25-30. doi:10.1016/S0023-6438(95)80008-5

Chen, P., Wang, H., He, M., Chen, B., Yang, B., & Hu, B. (2019). Size-dependent cytotoxicity study of ZnO nanoparticles in HepG2

cells. *Ecotoxicology and Environmental Safety*, *171*, 337-346. doi:10.1016/j.ecoenv.2018.12.096

da Silva, B. L., Caetano, B. L., Chiari-Andréo, B. G., Pietro, R. C. L. R., & Chiavacci, L. A. (2019). Increased antibacterial activity of ZnO nanoparticles: Influence of size and surface modification. *Colloids and Surfaces B: Biointerfaces*, *177*, 440-447. doi:10.1016/j.colsurfb.2019.02.013

Devi, P. G., & Velu, A. S. (2016). Synthesis, structural and optical properties of pure ZnO and Co doped ZnO nanoparticles prepared by the co-precipitation method. *Journal of Theoretical and Applied Physics*, *10*(3), 233-240. doi:10.1007/s40094-016-0221-0

Kinnunen, S., Lahtinen, M., Arstila, K., & Sajavaara, T. (2021). Hydrogen and deuterium incorporation in ZnO films grown by atomic layer deposition. *Coatings*, *11*(5), 542. doi:10.3390/coatings11050542

Manikandan, B., Endo, T., Kaneko, S., Murali, K. R., & John, R. (2018). Properties of sol gel synthesized ZnO nanoparticles. *Journal of Materials Science: Materials in Electronics*, *29*(11), 9474-9485. doi:10.1007/s10854-018-8981-8

Marin-Flores, C. A., Rodríguez-Nava, O., García-Hernández, M., Ruiz-Guerrero, R., Juárez-López, F., & Morales-Ramírez, A. D. J. (2021). Free-radical scavenging activity properties of ZnO sub-micron particles: Size effect and kinetics. *Journal of Materials Research and Technology*, *13*, 1665-1675. doi:10.1016/j.jmrt.2021.05.050

Martínez-Carmona, M., Gun'ko, Y., & Vallet-Regí, M. (2018). ZnO nanostructures for drug delivery and theranostic applications. *Nanomaterials*, *8*(4), 268. doi:10.3390/nano8040268

Mishra, P. K., Mishra, H., Ekielski, A., Talegaonkar, S., & Vaidya, B. (2017). Zinc oxide nanoparticles: A promising nanomaterial for biomedical applications. *Drug Discovery Today*, *22*(12), 1825-1834. doi:10.1016/j.drudis.2017.08.006

Narayana, A., Bhat, S. A., Fathima, A., Lokesh, S. V., Surya, S. G., & Yelamaggad, C. V. (2020). Green and low-cost synthesis of zinc oxide nanoparticles and their application in transistor-based carbon monoxide sensing. *RSC Advances*, *10*(23), 13532-13542. doi:10.1039/D0RA00478B

Nguyen, N. T., Nguyen, T. M. N., Le, N. T., & Le, T. K. (2020). Suppressing the photocatalytic activity of ZnO nanoparticles by Al-doping for the application in sunscreen products. *Materials Technology*, *35*(6), 349-355. doi:10.1080/10667857.2019.1684733

Pairoj, S., Damrongsak, P., Damrongsak, B., Jinawath, N., Kaewkhaw, R., Leelawattananon, T., ... & Locharoenrat, K. (2019). Antiradical properties of chemo drug, carboplatin, in cooperation with ZnO nanoparticles under UV irradiation in putative model of cancer cells. *Biocybernetics and Biomedical Engineering*, *39*(3), 893-901. doi:10.1016/j.bbe.2019.08.004

Rahman, F. (2019). Zinc oxide light-emitting diodes: A review. *Optical Engineering*, *58*(1). doi:10.1117/1.OE.58.1.010901

Rani, S., Suri, P., Shishodia, P. K., & Mehra, R. M. (2008). Synthesis of nanocrystalline ZnO powder via sol–gel route for dye-sensitized solar cells. *Solar Energy Materials and Solar Cells*, *92*(12), 1639-1645. doi:10.1016/j.solmat.2008.07.015

Shashanka, R., Esgin, H., Yilmaz, V. M., & Caglar, Y. (2020). Fabrication and characterization of green synthesized ZnO nanoparticle based dye-sensitized solar cells. *Journal of Science: Advanced Materials and Devices*, *5*(2), 185-191. doi:10.1016/j.jsamd.2020.04.005

Singh, T. A., Das, J., & Sil, P. C. (2020). Zinc oxide nanoparticles: A comprehensive review on its synthesis, anticancer and drug delivery applications as well as health risks. *Advances in Colloid and Interface Science*, *286*. doi:10.1016/j.cis.2020.102317

Wahab, R., Siddiqui, M. A., Saquib, Q., Dwivedi, S., Ahmad, J., Musarrat, J., ... Shin, H. S. (2014). ZnO nanoparticles induced oxidative stress and apoptosis in HepG2 and MCF-7 cancer cells and their antibacterial activity. *Colloids and Surfaces B: Biointerfaces*, *117*, 267-276. doi:10.1016/j.colsurfb.2014.02.038

Wallace, R., Brown, A. P., Brydson, R., Wegner, K., & Milne, S. J. (2013). Synthesis of ZnO nanoparticles by flame spray pyrolysis and characterisation protocol. *Journal of Materials Science*, *48*(18), 6393-6403. doi:10.1007/s10853-013-7439-x

Wasly, H. S., Abd El-Sadek, M. S., & Henini, M. (2018). Influence of reaction time and synthesis temperature on the physical properties of ZnO nanoparticles synthesized by the hydrothermal method. *Applied Physics A*, *124*, 1-12. doi:10.1007/s00339-017-1482-4

Available online at http://www.ssstj.sci.ssru.ac.th

Suan Sunandha Science and Technology Journal
©2022 Faculty of Science and Technology, Suan Sunandha Rajabhat University

Bio-based Polyurethane Derived from Carbon Dioxide and Epoxidized Soybean Oil

Naruebhorn Piyataksanon[1], Manus Seadan[2], Supakij Suttiruengwong[1*]

[1]Department of Materials Science and Engineering, Faculty of Engineering and Industrial Technology, Silpakorn University, Nakhon Pathom, Thailand
[2]Department of Physics, Faculty of Science, Silpakorn University, Nakhon Pathom, Thailand
***Corresponding author e-mail:** suttiruengwong_s@su.ac.th

Received: *15 February 2022* /**Revised:***27 April 2022* / **Accepted:** *26 May 2022*

Abstract

The synthesis of polyurethane relies on a toxic and petroleum-based isocyanate reactant. The aim of this research was to synthesize Polyurethane using environment-benign and renewable starting materials such as carbon dioxide and soybean oil. The carbonated soybean oil was first prepared from carbon dioxide (CO_2) and epoxidized soybean oil (ESBO) using zinc glutarate (ZnGA) as a catalyst but the result of FTIR indicated the absence of the peak of cyclic carbonate around 1800 cm^{-1}. Therefore, in this work, the synthesis of Polyurethane was modified from A. Lee (Lee & Deng, 2015) using tetramethylammonium bromide (TBAB) as a catalyst. The as-synthesized carbonated soybean oil (CSBO) was allowed to react with two types of substances, 3-aminopropyltriethoxysilane or diethylenetriamine with the molar ratios of cyclic carbonate:NH_2 of 1:1 with THF or DMF as solvents to obtain Polyurethanes (U1THF, U1DMF, U2THF, U2DMF). After 3 hours lignin solution was added to form a film. Raman spectra confirmed the catalyst removal from CSBO. FTIR spectra showed the peak around 1800 cm^{-1} assigned to cyclic carbonate of CSBO, and a new peak of urethane linkage around 1700 cm^{-1} (C=O stretching) of Polyurethanes. The conversion of epoxide to cyclic carbonate was also confirmed by ^{1}H-NMR. Upon adding lignin into the Polyurethanes, the lignin-urethane U1THF, and U1DMF formed films whereas U2THF, and U2DMF formed viscous liquids. In terms of applications, all four formulations can be potentially applied as bioadhesives.

Keywords: Non-isocyanate polyurethanes, Bio-based polyurethane, Epoxidized soybean oil, Bioadhesives

1. Introduction

The conventional polyurethanes are usually synthesized by a polycondensation reaction between a diol and a diisocyanate (Caraculacu & Coseri, 2001; Kathalewar, Joshi, Sabnis, & Malshe, 2013). However, isocyanates are derived from non-renewable resources and notably toxic chemicals. In addition, that is synthesized from an even more toxic substance phosgene which causes environmental hazards. The exposure to isocyanates can cause health effects (Gupta & Upadhyaya, 2014).

Due to the use of isocyanate in conventional polyurethanes, there is a substantial interest to develop alternative, environmentally friendly methods and materials for preparing polyurethanes (non-isocyanate routes). Polycondensation, rearrangement, and ring opening routes still use toxic agents such as phosgene, aziridine, acyl azide, etc. Among these routes, one of the most attractive methods is the polyaddition reaction of cyclic carbonate with amines (Cornille, Auvergne, Figovsky, Boutevin, & Caillol, 2017; Rokicki & Piotrowska, 2002). The reaction of carbon dioxide with epoxide groups to form cyclic carbonate is very effective to further the polymerization reaction such as the polymerization of copolycarbonate (Ree, Bae, Jung, & Shin, 1999; Taherimehr & Pescarmona, 2014).

Soybean oil as feedstocks for polymeric materials attracts increasing attention because they are inexpensive and available in large quantities. (Pfister, Xia, & Larock, 2011). They have been utilized to replace petroleum chemicals to produce coatings, inks, plasticizers, lubricants, and agrochemicals. (Maisonneuve, Lamarzelle, Rix, Grau, & Cramail, 2015; Rokicki, Parzuchowski, & Mazurek, 2015).

Recently, several researchers accomplished synthesizing polyurethane using soybean oil as a starting material using a non-isocyanate reaction route. In 2008, Javni et al. (Javni, Hong, & Petrović, 2008) prepared polyurethane by a non-isocyanate

Suan Sunandha Science and Technology Journal
©2022 Faculty of Science and Technology, Suan Sunandha Rajabhat University

route by reacting carbonated soybean oil with diamines. Carbonated soybean oil was reacted with different diamines such as 1,2- ethylenediamine, 1,4-butylenediamin and 1,6-hexylenediamine. The results showed that polyurethane could be prepared with a wide range of mechanical properties which was useful for industrial applications (Javni et al., 2008; Maisonneuve et al., 2015; Rokicki et al., 2015). The Poly (butylene carbonate) can successfully be synthesized based on carbon dioxide (CO_2) and 1, 2-butylene oxide using a self-prepared zinc glutarate (ZnGA) as a catalyst as reported by Chunsakul et al. (Chunsakul, Seadan, & Suttiruengwong, 2019).

Therefore, the aim of this study was to synthesize Polyurethane using environment-benign and renewable starting materials such as carbon dioxide and soybean oil. The carbonated soybean oil was first prepared from carbon dioxide (CO_2) and epoxidized soybean oil (ESBO) using zinc glutarate (ZnGA) as a catalyst but the result of FTIR indicated the absence of the peak of cyclic carbonate around 1800 cm^{-1}. Therefore, in this work, the synthesis of Polyurethane using tetra-n-butylammonium bromide (TBAB) as a catalyst. Chemical analysis of synthesized polyurethanes was carried out using FTIR, NMR and Raman spectroscopy. The peel strength was conducted and compared with commercial pressure sensitive adhesive.

2. Materials and Method

2.1 Materials

Epoxidized soybean oil was donated by Applied DB public company LTD, Thailand. Carbon dioxide (99.8%) was purchased from MSG Company. Titanium tetrachloride (TiCl), Tetra-n-butylammonium bromide (TBAB), Lignin, alkaline, (3-Aminopropyl) triethoxysilane were purchased from Sigma Aldrich, Singapore. N,N-dimethyl-formamide (DMF) was obtained from RCI Labscan. THF was purchased from QReC. Ethyl acetate was purchased from SCHARLAU. Diethylenetriamine was purchased from FLUKA. All other chemical reagents were analytical grade.

2.2 Synthesis of Carbonate Soybean Oil (CSBO)

The ESBO (50 g) and TBAB (5 mole% with respect to the epoxy content) were first added into the reactor. The reactor was pressurized at 70 bar with CO_2. Then the reactor was stirred at 400 rpm and heated up to 140˚C. After the reaction time of 72 h, the reactor was cooled at 50˚C. The product was dissolved in ethyl acetate and then washed catalyst from product solution by adding distilled water. The mixture was separated using a separatory funnel. Both water and ethyl acetate were removed via rotary evaporator. The reaction is shown in scheme 1.

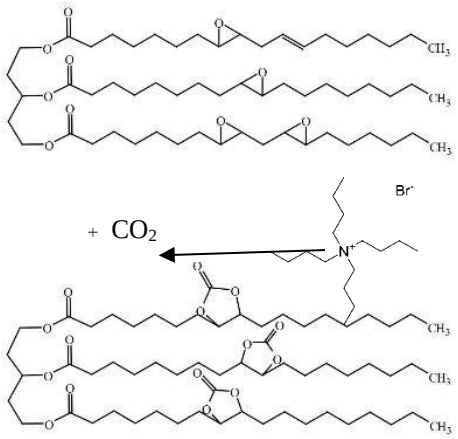

Scheme 1. Synthesis of carbonate soybean oil.

2.3 Synthesis of Polyurethane

3 g of CSBO (cyclic carbonate, measured by ^1H NMR) was dissolved in 20 ml with two different solvents (THF and DMF). The as-synthesized carbonated soybean oil (CSBO) was allowed to react with two types of substances, (3-Aminopropyl) triethoxysilane or diethylene-triamine with the molar ratios of cyclic carbonate: NH_2 of 1:1) with THF or DMF as solvents to obtain Polyurethanes (U1THF, U1DMF, U2THF, and U2DMF), where U1 and U2 denote polyurethane from (3-Aminopropyl) triethoxysilane and polyurethane from diethylenetriamine respectively. The reaction mixture was stirred at 70˚C for 3 h. After the reaction, the product was poured into a Teflon mold and oven at 70˚C for 7 h.

2.4 Synthesis of lignin-Polyurethane

After 3 hours of reaction for the preparation of Polyurethanes (U1THF, U1DMF, U2THF, and U2DMF), the solution of lignin alkali dissolved in two different solvents (THF/water and DMF/water) (12 ml/8 ml) was added. The reaction mixture was stirred at 70˚C for 12 hours, then the product was poured into Teflon mold and oven-sampled at 70˚C for 7 hours.

Suan Sunandha Science and Technology Journal
©2022 Faculty of Science and Technology, Suan Sunandha Rajabhat University

2.5 Characterization

2.5.1 Raman Spectroscopy

The catalyst was successfully removed from carbonate soybean oil which is characterized by Raman spectroscopy (Bruker, USA). The Raman spectra were recorded between 107-3781 cm^{-1} and used a laser source 785 nm with the resolution of 9-18 cm^{-1}.

2.5.2 FTIR Analysis

The chemical structure and functional groups of carbonate soybean oil, Polyurethane, and lignin polyurethane from Epoxidized soybean oil, and CO_2 were characterized with Fourier transform infrared spectrometer; FTIR (VERTEX70, Bruker, USA). The FTIR spectra were recorded in the range of 4000-400 cm^{-1} and used the resolution of 4 cm^{-1}.

2.5.3 ^{1}H-Nuclear magnetic resonance (^{1}H-NMR)

Nuclear magnetic resonance (NMR) using NMR Spectrometer from Varian (400MHz) with ^{1}H probes. In The NMR spectroscopic measurements, chemical shifts were calibrated with the chemical shifts of the solvent used (D-chloroform).

2.5.4 T-Peel test

The T-peel test of samples (Figure 1) were measured at room temperature with a crosshead speed of 100 mm/min by a universal testing machine (NRI-TS500-5B).

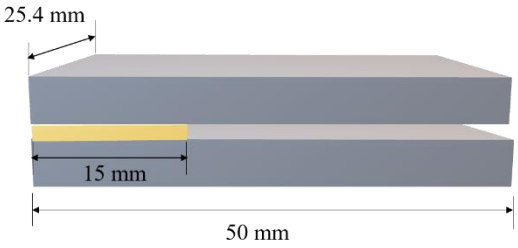

Figure 1. Sample of T-peel test.

3. Results and Discussion

3.1 Characterizations of carbonate soybean oil

The synthesized cyclic carbonates from epoxides are shown in scheme 1. Under the high-pressure condition, the tetrabutylammonium ion activates the epoxide ring followed by the nucleophilic attack by the bromide ion. Then it attacks the carbon dioxide to produce the cyclic carbonate, which simultaneously allows the bromide to leave and the catalyst to be released (Chunsakul et al., 2019; Doll & Erhan, 2005). However, the catalyst is removed using an extraction method using ethyl acetate and water.

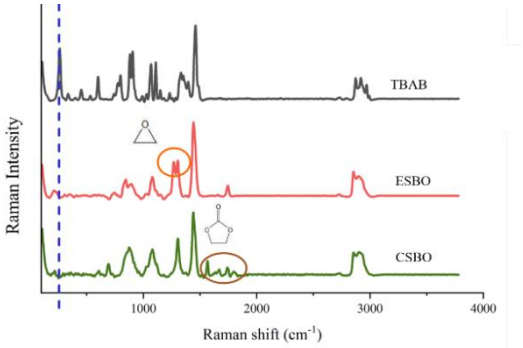

Figure 2. Raman spectra of Tetra- n- butyl ammonium bromide (TBAB), Epoxidized soybean oil (ESBO), and Carbonate soybean oil (CSBO).

The results in Figure 2 showed that Raman spectra of TBAB appears the characteristic peak of TBAB at Raman shift 265 cm^{-1}, the Raman spectra of ESBO showed a peak of the epoxy group at doublet 1260 and 1280 cm^{-1} and the Raman spectra of CSBO showed a new peak C=O of cyclic carbonate around 1600-1800 cm^{-1} but no characteristic peak of C-C stretching of TBAB and characteristic doublet peak of the epoxy group. Therefore, the result confirmed the catalyst removal from CSBO.

Figure 3 presents the FTIR spectra of ESBO, and CSBO for comparison. Table 1 and 2 list the vibration modes and wavenumbers of IR absorption peak of ESBO and CSBO respectively.

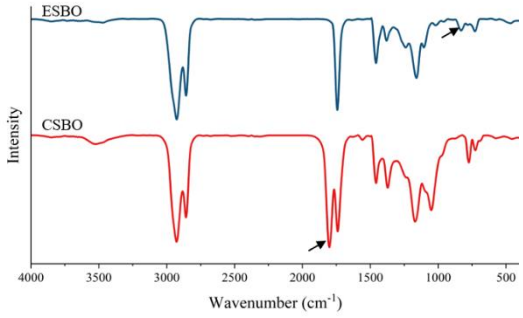

Figure 3. FTIR spectra of Epoxidized soybean oil (ESBO), and Carbonate soybean oil (CSBO).

Suan Sunandha Science and Technology Journal
©2022 Faculty of Science and Technology, Suan Sunandha Rajabhat University

Table 1. Vibration modes and Wavenumbers of IR absorption peaks in FTIR spectra of ESBO.

Peak value (cm^{-1})	Group
3000 - 2800	Stretching vibration of saturated C-H bond
1750 - 1700	Stretching vibration of C=O
1280 - 1200	Stretching vibration of C-O (ester bond)
825	Stretching vibration of C-O (epoxy group)

Table 2. Vibration modes and Wavenumbers of IR absorption peaks in FTIR spectra of CSBO.

Peak value (cm^{-1})	Group
3000 - 2800	Stretching vibration of saturated C-H bond
1800	Stretching vibration of C=O (cyclic carbonate group)
1750 - 1700	Stretching vibration of C=O
1280 - 1200	Stretching vibration of C-O (ester bond)

The results in Figure 3 and table 1 revealed that the peak at 825 cm-1 corresponded to the characteristic peak of C-O stretching (epoxy group). The FTIR spectra of CSBO showed the new characteristic peak corresponding to the cyclic carbonate group. The characteristic peak of cyclic carbonate (C=O) is indicated at 1800 cm^{-1} and the peak of the epoxy group disappeared.

In addition, the physical appearance of ESBO was a colorless liquid but after reaction with CO_2, the product was a brown liquid, and the viscosity was increased. Therefore, it was confirmed that the synthesis of CSBO was successful.

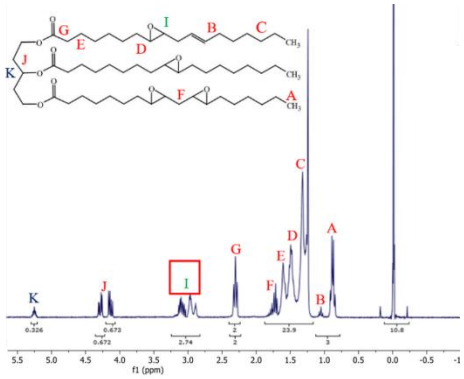

Figure 4. NMR spectra of ESBO.

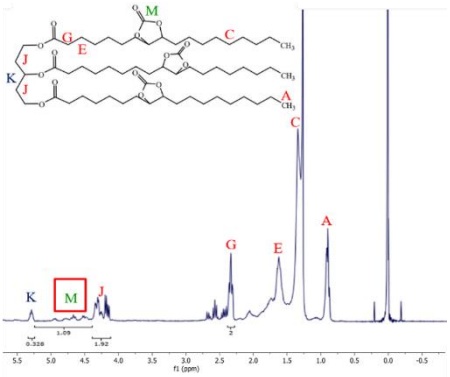

Figure 5. ^{1}H-NMR spectra of CSBO.

The ^{1}H-NMR spectra of ESBO and CSBO were used to propose the chemical structure and it confirmed the conversion of epoxide to cyclic carbonate. Figure 4 showed the NMR spectra of ESBO, where the peak at 2.80-3.20 ppm corresponded to the epoxy group. Figure 5 showed the NMR spectra of CSBO, which showed the peak at 4.20-5.10 ppm assigned to cyclic carbonate groups.

The performance of the carbonation reaction was evaluated through the conversion carbonation or yield (% Y) of cyclic carbonate. The mole of epoxide and carbonate groups were calculated from the integrals of the ^{1}H-NMR spectrum (Figure 4 and 5). The central carbon (K) signal was taken as the spectrum normalization factor. The mole of epoxide groups (Em) was calculated with the signals corresponding to epoxy rings (I) (Equation (1)). Similarly, through Equation (2), the mole of carbonate groups (Cm) was calculated from the signals (M) (González Martínez, Vigueras Santiago, & Hernández López, 2021).

Then quantitative results, 100% conversion of ESBO into CSBO was confirmed via the 1H-NMR spectrum. It was clear from Figure 5 that the original epoxy groups at 2.80 - 3.20 ppm disappeared while the new signals at 4.20 - 5.10 ppm corresponding to the cyclic carbonate group appeared. The calculated moles of the epoxy group and cyclic carbonate group are 4.26 and 2.53 respectively. The yield of cyclic carbonate was found to be 61% (Equation (3)).

$$Em = \frac{I}{2K} \quad (1)$$

$$Cm = \frac{M}{2K} \quad (2)$$

$$\%Y = \frac{C_m}{E_m}\, x\, 100 \quad (3)$$

Suan Sunandha Science and Technology Journal
©2022 Faculty of Science and Technology, Suan Sunandha Rajabhat University

3.2 Characterization of Lignin-Polyurethane

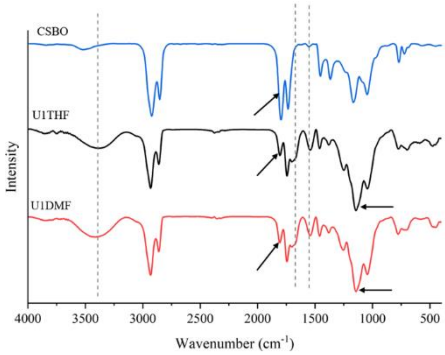

Figure 6. FTIR spectra of Carbonate soybean oil (CSBO), U1THF, and U1DMF.

Table 3. Vibration modes and wavenumbers of IR absorption peaks in FTIR spectra of U1THF and U1DMF.

Wavenumber (cm^{-1})	Groups
3300	Stretching vibration of N-H (Urethane linkage)
3000 - 2800	Stretching vibration of saturated C-H bond
1800	Stretching vibration of C=O (cyclic carbonate group)
1600	Stretching vibration of C=O (Urethane linkage)
1500	Stretching vibration of C-N (Urethane linkage)
1280 - 1200	Stretching vibration of C-O (ester bond)
1078	Stretching vibration of Si-O

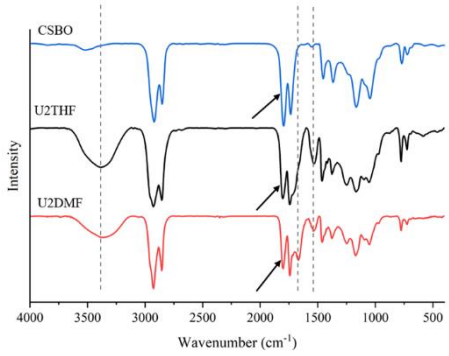

Figure 7. FTIR spectra of Carbonate soybean oil (CSBO), U2THF, and U2DMF.

Table 4. Vibration modes and Wavenumbers of IR absorption peaks in FTIR spectra of U1THF and U1DMF.

Peak value (cm^{-1})	Group
3300	Stretching vibration of N-H (Urethane linkage)
3000 - 2800	Stretching vibration of saturated C-H bond
1800	Stretching vibration of C=O (cyclic carbonate group)
1600	Stretching vibration of C=O (Urethane linkage)
1500	Stretching vibration of C-N (Urethane linkage)
1280 - 1200	Stretching vibration of C-O (ester bond)

The results in Figure 6 and 7 and Table 3 and 4 showed that the FTIR spectra of U1THF was similar to U1DMF. That showed the new characteristic peak corresponding to the Urethane linkage. That peak C=O stretching at 1600 cm^{-1}, C-N stretching at 1500 cm^{-1}, and N-H stretching at 3300 cm^{-1}. The characteristic peak of cyclic carbonate (C=O) was indicated at 1800 cm^{-1} was decreased. Therefore, the result can be confirmed that the ring-opening reaction turns into urethane linkage.

In addition, the characteristic of Si-O-Si stretching at 1078 cm^{-1} intensity was increased as shown in Figure 6. The appearance of Si-O-Si is due to the self-condensation of (3-Aminopropyl) triethoxysilane. (Kathalewar et al., 2013; Robles, Csóka, & Labidi, 2018). Therefore U1THF and U1DMF samples were able to form into films. However, U2THF and U2DMF samples were viscous liquid. They could not be fabricated into the film.

Upon adding lignin into the Polyurethanes, the lignin-U1THF and Lignin-U1DMF formed into films whereas lignin-U2THF and lignin-U2DMF were viscous liquid. However, U1THF and U2THF formed a heterogeneous phase. This was probably due to the distinguished solubility of lignin alkali and THF. On the other hand, the solubility of lignin alkali in DMF was better. Thus, U1DMF and U2DMF mixtures were homogeneous.

Suan Sunandha Science and Technology Journal
©2022 Faculty of Science and Technology, Suan Sunandha Rajabhat University

3.3 T-Peel test

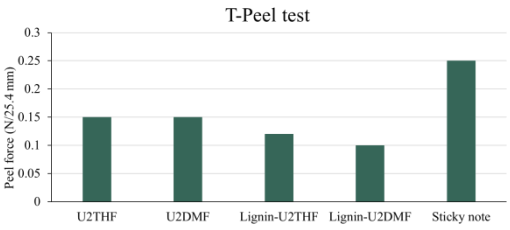

Figure 8. Peel force of viscous liquid polyurethanes compared with sticky notes.

Figure 8 showed the peel force of the samples compared to commercial sticky notes. U2THF and U2DMF have the same peel force (around 0.15 N/25.4 mm). U2THF-lignin U2DMF-lignin showed the peel forces of 0.12 N/25.4 mm and 0.10 N/25.4 mm respectively. In all cases, the peel force was lower than that of the sticky note. Without lignin, the adhesive performance was better in terms of the peel force. This may be due to the phase separation of lignin and polyurethane, which could not form the continuous phase. Although all specimens showed lower peel strengths than the commercial one. It could possibly be recommended as pressure sensitive bioadhesives.

4. Conclusion

Polyurethane was successfully synthesized using carbon dioxide and soybean oil as renewable starting materials. U1THF and U1DMF specimens could be fabricated into films whereas U2THF and U2DMF were viscous liquid. After adding lignin alkaline, U1THF-Lignin and U2THF-Lignin formed a heterogeneous phase but U1DMF-Lignin and U2DMF-Lignin were homogeneous phases. Peel strengths of all specimens were lower than the commercial one. In terms of applications, the synthesized polyurethane can be potentially applied as pressure sensitive bioadhesives.

5. Acknowledgment

We would like to thank the Department of Materials Science and Engineering, Faculty of Engineering and Industrial Technology, Silpakorn University for financial support. Applied DB (PCL), Thailand is gratefully acknowledged for providing Epoxidized soybean oil.

6. References

Caraculacu, A. A., & Coseri, S. (2001). Isocyanates in polyaddition processes. Structure and reaction mechanisms. *Progress in Polymer Science, 26*, 799-851.

Chunsakul, T., Seadan, M., & Suttiruengwong, S. (2019). Copolycarbonate derived from carbon dioxide as toughness improvement for Poly (lactic acid). *Materials Today: Proceedings, 17*, 1949-1955. doi:10.1016/j.matpr.2019.06.239

Cornille, A., Auvergne, R., Figovsky, O., Boutevin, B., & Caillol, S. (2017). A perspective approach to sustainable routes for non-isocyanate polyurethanes. *European Polymer Journal, 87*, 535-552. doi:10.1016/j.eurpolymj.2016.11.027

Doll, K. M., & Erhan, S. Z. (2005). The improved synthesis of carbonated soybean oil using supercritical carbon dioxide at a reduced reaction time. *Green Chemistry, 7*(12), 849-854. doi:10.1039/b511014a

González Martínez, D. A., Vigueras Santiago, E., & Hernández López, S. (2021). Yield and selectivity improvement in the synthesis of carbonated linseed oil by catalytic conversion of carbon dioxide. *Polymers, 13*(6). doi:10.3390/polym13060852

Gupta, S., & Upadhyaya, R. (2014). Cancer and p21 protein expression: In relation with isocyanate toxicity in cultured mammalian cells. *The International Journal of Pharmaceutical Research and Bio-Sciences, 3(*6*)*, 20-28.

Javni, I., Hong, D. P., & Petrović, Z. S. (2008). Soy-based polyurethanes by nonisocyanate route. *Journal of Applied Polymer Science, 108*(6), 3867-3875. doi:10.1002/app.27995

Kathalewar, M. S., Joshi, P. B., Sabnis, A. S., & Malshe, V. C. (2013). Non-isocyanate polyurethanes: From chemistry to applications. *RSC Advances, 3*(13), 4110-4129. doi:10.1039/c2ra21938g

Lee, A., & Deng, Y. (2015). Green polyurethane from lignin and soybean oil through non-isocyanate reactions. *European Polymer Journal, 63*, 67-73. doi:10.1016/j.eurpolymj.2014.11.023

Maisonneuve, L., Lamarzelle, O., Rix, E., Grau, E., & Cramail, H. (2015). Isocyanate-free routes to polyurethanes and poly(hydroxy urethane)s. *Chemical Reviews, 115*(22), 12407-12439. doi:10.1021/acs.chemrev.5b00355

Pfister, D. P., Xia, Y., & Larock, R. C. (2011). Recent advances in vegetable oil-based polyurethanes. *ChemSusChem, 4*(6), 703-717. doi:10.1002/cssc.201000378

Ree, M., Bae, J. Y., Jung, J. H., & Shin, T. J. (1999). A new copolymerizayion processs leading to poly(propylene carbonate) with a highly enhanced yield from carbon dioxide and propylene oxide. *Journal of Polymer*

Suan Sunandha Science and Technology Journal
©2022 Faculty of Science and Technology, Suan Sunandha Rajabhat University

Science Part A: Polymer Chemistry, *37*(12), 1863-1876.

Robles, E., Csóka, L., & Labidi, J. (2018). Effect of reaction conditions on the surface modification of cellulose nanofibrils with aminopropyl triethoxysilane. *Coatings*, *8*(4). doi:10.3390/coatings8040139

Rokicki, G., Parzuchowski, P. G., & Mazurek, M. (2015). Non-isocyanate polyurethanes: Synthesis, properties, and applications. *Polymers for Advanced Technologies*, *26*(7), 707-761. doi:10.1002/pat.3522

Rokicki, G., & Piotrowska, A. (2002). A new route to polyurethanes from ethylene carbonate, diamines and diols. *Polymer*, *43*, 2927-2935.

Taherimehr, M., & Pescarmona, P. P. (2014). Green polycarbonates prepared by the copolymerization of CO_2 with epoxides. *Journal of Applied Polymer Science*, *131*(21). doi:10.1002/app.41141

Available online at http://www.ssstj.sci.ssru.ac.th

Suan Sunandha Science and Technology Journal
©2022 Faculty of Science and Technology, Suan Sunandha Rajabhat University

Stretchability and Deformation Behavior of Polybutylene Adipate-co-terephthalate Blend Films

Korawit Kaoudom[1], Manus Seadan[2], Supakij Suttiruengwong[1,*]

[1]Department of Materials Science and Engineering, Faculty of Engineering and Industrial Tenchnology, Silpakorn Uniersity, Nakhon Pathom 73000, Thailand

[2]Department of Physics, Faculty of Science, Slpakorn University, Nahon Pathom 73000, Thailand

*Corresponding author e-mail: suttiruengwong_s@su.ac.th

Received: *15 February 2022* /**Revised**: *30 March 2022* /**Accepted**: *14 June 2022*

Abstract

The single use packaging is widely used in various products; ranging from food to non-food contact, from commodity to specialty purposes. Most of these materials are derived from non-renewable fossil resources. In a sustainable manner, it needs to be recyclable or compostable. Good mechanical properties together with biodegradability can make the product more recyclable. In this study, the elasticity for films consisting of polybutylene adipate-co-terephthalate (PBAT) blended with polylactic acid (PLA) (10, and 20 %wt), additive and reactive agents were evaluated. The blends were prepared via a twin-screw extruder. The film specimens were prepared by cast film extrusion. The films were then stretched with different ratios (1.5, 2 and 2.5 times) by the uniaxial machine. The mechanical properties, elasticities and surface morphology of uniaxially stretched PBAT and PBAT blend films were characterized by tensile testing and scanning electron microscope (SEM), respectively. The tensile strength of stretched films tended to improve while the elongation at break reduced at higher stretching ratios. The surface morphology of stretched films revealed that the degree of orientation was increased after higher stretching ratios. The ability to recover in the plastic deformation region of stretched films was increased at the higher stretching ratios.

Keywords: Elasticity, Polybutylene adipate-co-terephthalate, Biodegradable plastics, Stretchability

1. Introduction

Nowadays most of the food and non-food packages are made from fossil-based polymers such as poly(propylene) (PP), high density poly(ethylene) (HDPE), low density poly(ethylene) (LDPE), linear low density poly(ethylene) (LLDPE), poly(ethylene terephthalate) and etc. These plastics, particularly the single use plastic, are generally not biodegradable and accumulate for a very long time. Based on the single-use plastic waste statistics, 380 million tons of single-use plastic (or 50% of the total plastic production) were generated each year and we use them only once, the same amount of plastic becomes trash in a year (SeedScientific, 2021). Regarding the single-use plastic packaging, the thin films are most dominated in terms of the applications both for food and non-food items. It is interesting therefore to find sustainable solutions. Two of the main options are recycle or composting options for such a plastic. For composting options, the existing compostable polymers poly polybutylene adipate-co-terephthalate (PBAT), polylactic acid (PLA), and poly(butylene succinate) (PBS) are the most popular ones. In 2020, global production capacities of biodegradable polymer were more than bio-based/non-biodegradable polymers. Top 3 of biodegradable polymers are Starch blends, PLA and PBAT, respectively (European Bioplastics, 2020). In the packaging use, PBAT is generally considered the most suitable alternative to low-density polyethylene based products due to its properties similar to LDPE and because of its high molecular weight and long chain branched molecular structure, high elongation at break, high failure energy and good processability on blown and cast film lines (BASF, 2013; Pietrosanto, Scarfato, Di Maio, & Incarnato, 2020).

Suan Sunandha Science and Technology Journal
©2022 Faculty of Science and Technology, Suan Sunandha Rajabhat University

In recent years, the research development and improvement of PLA and PBAT have been popular in many applications (Chen, Han, Zhang, & Dong, 2021; Deng, Yu, Wongwiwattana, & Thomas, 2018; Hongdilokkul et al., 2015; Li et al., 2017; Su, Duhme, & Kopitzky, 2020). Su et al. (2020) prepared uncompatibilized PBAT/PLA blends with different techniques. In blown films production, using PLA contents (10-30 %wt), the tensile strength of blown films tended to increase in MD while the elongation at break increased. However, the tensile strength of pressed panels and flat films processes were not different except 30 %wt PLA in the pressed panels process, which decreased. For the same composition, the mechanical properties of blown film production were higher than pressed panels. Hongdilokkul et al. (2015) used peroxide as a reactive agent in PLA/PBAT blends. They reported an improved interfacial adhesion between PLA and PBAT phase, leading to the improvement of the drawability. When blended with 20 %wt PBAT, the drawability, processability and toughness properties of PLA were greatly improved. Likittanaprasong, Seadan, and Suttiruengwong (2015) enhanced impact property of poly(lactic acid) with different flexible copolymers. They used 6 flexible copolymers. When copolymers were added into PLA, tensile strength and modulus of PLA/copolymers were decreased as a result of elasticity of copolymers. PLA/copolymers were more flexible than PLA. The elongations at break of PLA/copolymers were increased resulting from the PLA/copolymers samples more ductile than PLA sample. The results indicated that different copolymers had different impact resistance. Chen et al. (2021) prepared toughened PLA nanocomposites by combining the modification nano-SiO_2 and pre-stretching. The modulus and tensile strength of PLA/SiO_2 nanocomposites were higher than those of pure PLA because SiO_2 nanoparticles played a reinforcement role in the PLA matrix. After pre-stretching, a brittle-to-ductile transition occurred in the PLA/SiO_2 nanocomposites. When the pre-stretching ratio (PSR) was 0.5, 1.0, 1.5 and 2.0, the elongation at break, modulus and tensile strength at break were higher than undrawn PLA. The elongation at break was decreased with increasing PSR while modulus and tensile strength at break were increased greatly. This was due to the degree of orientation, which was increased with the increment of PSR. Thus, in this work, we proposed another way of improving the mechanical properties of PBAT and PBAT blend films by stretching method. The effect of stretching on the mechanical properties, elasticity and surface morphology of PBAT and PBAT blend films were investigated.

2. Materials and Methods

2.1 Materials

PBAT grade Ecoflex® F Blend C1200, BASF was purchased from Polymat Ltd. PLA grade 4043D was purchased from NatureWorks. Di (tert-butylperoxyisopropyl) benzene (DB), Perkadox 14s, having 40% of peroxide, was supplied by Akzo Nobel, Netherlands. Multi-functional epoxy chain extender (ECE), Joncryl® ADR-4368C was purchased from BASF Co. Ltd. Ethylene copolymer (E) (Biomax® strong 120) was purchased from Dupont CO. Ltd.

2.2 Methods

2.2.1 Preparation and stretching of films

The PBAT/PLA blended with additive and reactive agent was prepared by a twin-screw extruder. The melting blending process was carried out at temperature profile of 80-190°C with a screw speed of 200 rpm except neat PBAT and PBAT_E5. Both compounds were carried out at 80-135°C with the same screw speed as the PBAT/PLA blends. The compositions of polymer compounds were shown in table 1. The compound films were prepared by a cast film extruder. The cast film extrusion process was carried out at 105-150°C (neat PBAT and PBAT_E5) and 110-210°C (PBAT/PLA blended with additive and reactive agent) with screw speed 80 rpm. Then the stretched films were fabricated with 1.5, 2 and 2.5 times of original length by a uniaxial machine as shown in Figure 1. The stretching temperature was provided at ~60°C by heat gun. After stretching, they

Suan Sunandha Science and Technology Journal
©2022 Faculty of Science and Technology, Suan Sunandha Rajabhat University

were cooled down to room temperature by air before they were unloaded from the grips.

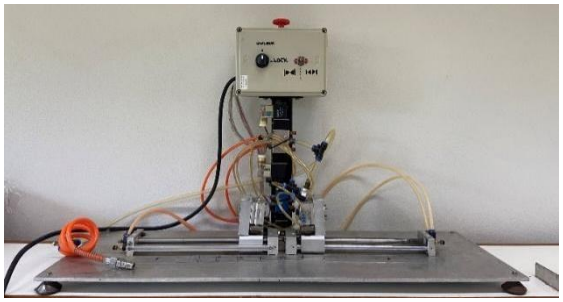

Figure 1. Uniaxial machine.

Table 1. The composition of polymer compounds.

Samples	PBAT	PLA	Ethylene copolymer (phr)	DB (phr)	ECE (phr)
PBAT	100	-	-	-	-
PBAT_E5	100	-	5	-	-
P90_L10_DB0.2_ECE0.1	90	10	-	0.2	0.1
P90_L10_E5_DB0.2_ECE0.1	90	10	5	0.2	0.1
P80_L20_DB0.2_ECE0.1	80	20	-	0.2	0.1
P80_L20_E5_DB0.2_ECE0.1	80	20	5	0.2	0.1

of 30 MPa and a crosshead speed of 50 mm/min. The specimens of unstretched and stretched were cut the same as tensile testing.

2.2.4 Scanning electron microscopy (SEM)

Surfaces morphology of the samples were investigated by a Field Emission Scanning Electron Microscope, FESEM) MIRA3 TESCAN CO., LTD, Czech Republic. Gold sputtering was performed to coat on samples before testing.

3. Results and Discussions

3.1 Mechanical properties

The mechanical properties of unstretched PBAT, PBAT_E5 and PBAT/PLA blend films were measured by tensile testing at room temperature. Figure 2. showed the stress-strain curves of unstretched PBAT, PBAT_E5 and PBAT/PLA blend films. Unstretched PBAT film showed tensile strength and elongation at break at 25.4 MPa and 551.29%, respectively. When adding ethylene copolymer, tensile strength of unstretched PBAT_ E5 film decreased from 25.4 MPa to 21.9 MPa while elongation at break slightly increased from 551.29%

2.2.2 Tensile testing

The mechanical properties of samples were measured at room temperature with a crosshead speed of 50 mm/min by a universal testing machine (NRI-TS500-5B) according to ASTM D882. The standard films were cut from the unstretched and stretched samples along the stretching direction

.

2.2.3 Cyclic testing

Elasticities of the samples were measured by a universal testing machine in cyclic test mode. The cyclic tests were performed at maximum stress (σ_{max})

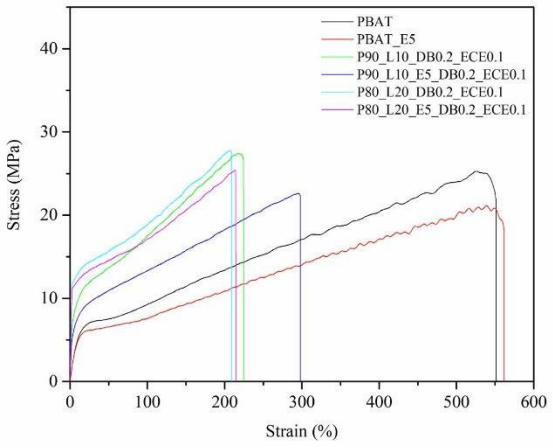

Figure 2. Stress-Strain curve of unstretched PBAT, PBAT_E5 and PBAT/PLA blend films.

to 561.89%. For PBAT/PLA blend films, elongation at break of PBAT/PLA blend films was decreased a lot after blending PLA into PBAT while tensile strength slightly increased except tensile strength of P 90 _L10 _ E 5 _ DB 0.2 _ ECE 0.1 film slightly decreased. When compared neat PBAT film with P90_ L10_ DB0.2 _ ECE0.1 and P80 _ L20_DB0.2_ ECE0.1 films, tensile strength increased from 25.4 MPa to 27.4 MPa and 27.8 MPa respectively,

Suan Sunandha Science and Technology Journal
©2022 Faculty of Science and Technology, Suan Sunandha Rajabhat University

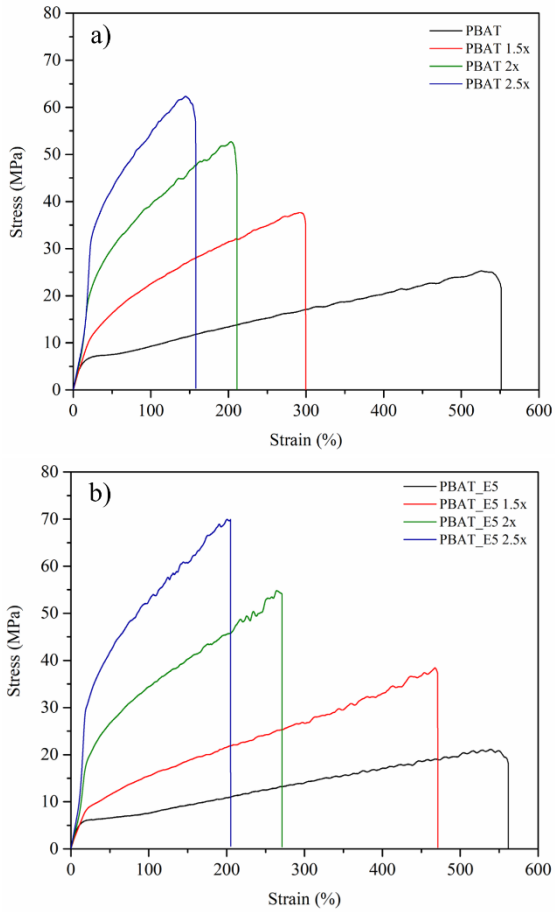

Figure 3. Stress-Strain curve of unstretched films and stretched films (1.5x, 2x and 2.5x) a) PBAT and b) PBAT_E5.

whereas elongation at break was decreased from 551.29% to 224.65% and 209.08% respectively because PLA is rigid polymer when compared to PBAT. Rigid polymer has high tensile strength and modulus (Pitivut, Suttiruengwong, & Seadan, 2015). When comparing PBAT/PLA blend films with and without additive, tensile strength of P90_ L10 _ E5 _ DB0.2 _ ECE0.1 and P80 _ L20 _ E5 _ DB0.2_ECE0.1 decreased from 27.4 MPa and 27.8 MPa to 22.6 MPa and 25.4 MPa respectively while elongation at break increased from 224.65% and 209.08% to 298.13% and 214.51% respectively because ethylene copolymer was more flexible than PLA (Likittanaprasong et al., 2015). Tensile strength of all unstretched films was slightly different but elongation at break of unstretched PBAT/PLA blends film was significantly decreased. Therefore, unstretched PBAT and PBAT _ E5 films were selected for stretching to improve mechanical properties and studied elasticity after stretching.

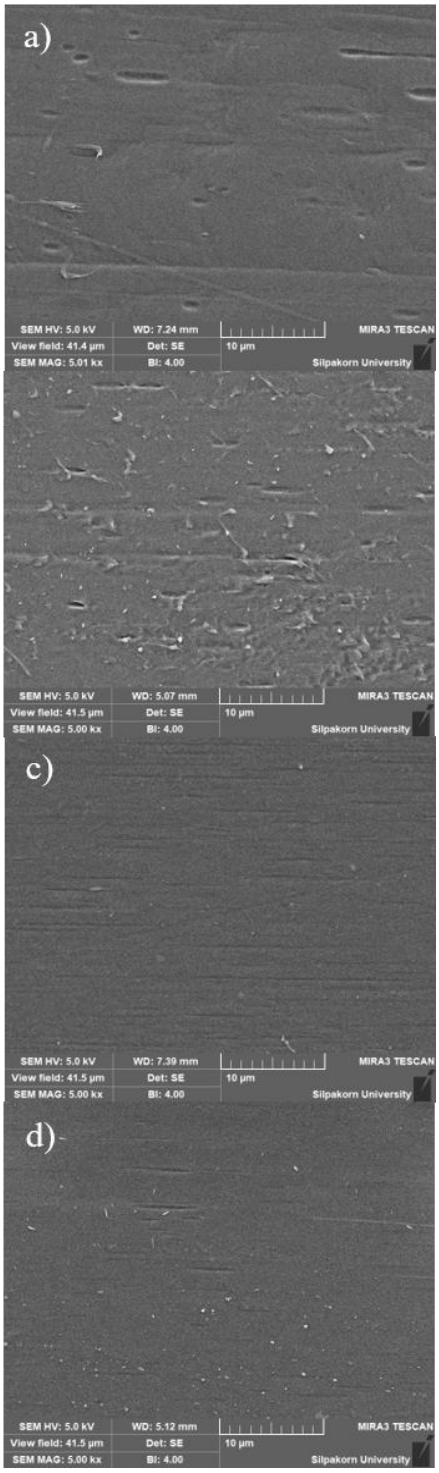

Figure 4. Surface morphology of unstretched films a) PBAT and b) PBAT_E5 and stretched films (2x) c) PBAT 2x and d) PBAT_E5 2x.

After stretching PBAT and PBAT_E5 films, Figure 3. represents the stress-strain curves of

Suan Sunandha Science and Technology Journal
©2022 Faculty of Science and Technology, Suan Sunandha Rajabhat University

unstretched and stretched PBAT and PBAT_E5 films with different ratios. It was obvious that the tensile strength of stretched PBAT and PBAT_E5 films were different after stretching. With increasing the stretching ratio, the stretched PBAT and PBAT_E5 transformed from a ductile to brittle behavior and tensile strength of stretched PBAT and PBAT_E5 films tended to increase while elongation at break tended to decrease because of stretched films in the cold drawing zone of polymer and the orientation of the polymer chains during in stretching process (Su et al., 2020). At the highest stretching ratio (2.5x), tensile strength of stretched PBAT and PBAT_E5 films increased by 164% (from 25.4 MPa to 66.71 MPa) and 186% (from 21.9 MPa to 63.22 MPa) but elongation at break decreased by 71% (from 551.29% to 165.19%) and 63% (from 561.89% to 206.15%), respectively. This may be due to the fact that by stretching, the stretched polymers chains were oriented along uniaxial machine direction and the degree of orientation was increased with the increment of stretching ratio (Chen et al., 2021).

3.2 Morphology of unstretched and stretched films

Figure 4. shows Surface morphology of unstretched and stretched PBAT and PBAT_E5 films with stretching ratio 2x. Surface morphology of unstretched PBAT and PBAT_E5 films show droplet voids on film surfaces were illustrated in Figure 4 a) and b). But unstretched PBAT and PBAT_E5 showed different film surfaces. When adding ethylene copolymer into PBAT, film surface of PBAT_E5 film was rougher than PBAT film because ethylene copolymer particles were elongated and dispersed on the film surface After stretching PBAT and PBAT_E5 films. Surface morphology of stretched PBAT and PBAT_E5 were shown in figure 4 c) and d), the droplet voids became elongated void due to the orientation of the stretched films in uniaxial machine direction. It confirmed the increased degree of orientation with the increment of stretching ratio, resulting in tensile strength of stretched films increased while elongation at break decreased as mentioned above. The increase in tensile strength may be resulted from the degree of the crystallinity. However, a role of the crystallinity was not investigated in this work.

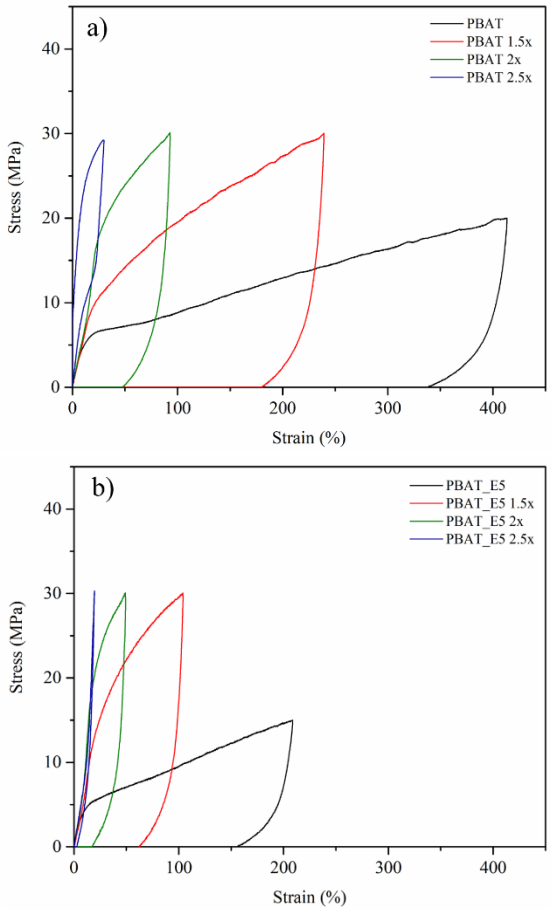

Figure 5. Stress-Strain curve from cyclic test of unstretched films and stretched films (1.5x, 2x and 2.5x) a) PBAT and b) PBAT_E5.

3.3 Elasticity of unstretched and stretched films

Elasticity of unstretched and stretched PBAT and PBAT_E5 films were tested by cyclic testing. It was reported in the form of %recovery. The cyclic tests were performed at maximum stress 30 MPa. Figure 5. showed the stress-strain curves from cyclic tests of unstretched and stretched PBAT and PBAT_E5 films. In case of unstretched PBAT and PBAT_E5 films, they cannot be tested at maximum stress 30 MPa because tensile strength of unstretched PBAT and PBAT_E5 films were 25.4 MPa and 21.9 MPa, respectively. The unstretched PBAT and PBAT_E5 films were tested at maximum stress 20 MPa and 15 MPa, respectively. It found that %recovery of unstretched PBAT and PBAT_E5 films were 18.09% and 25.25%, respectively. After stretching, %recovery of stretched PBAT and

Suan Sunandha Science and Technology Journal
©2022 Faculty of Science and Technology, Suan Sunandha Rajabhat University

Table 2. %Recovery of unstretched and stretched PBAT and PBAT_E5 films.

Sample	Stretching ratio	Recovery (%)
PBAT	1	18.09
PBAT 1.5x	1.5	24.80
PBAT 2x	2	48.41
PBAT 2.5x	2.5	74.24
PBAT_E5	1	25.25
PBAT_E5 1.5x	1.5	40.11
PBAT_E5 2x	2	64.64
PBAT_E5 2.5x	2.5	86.15

PBAT_E5 films increased with increasing stretching ratio because increment of stretching ratio resulted in tensile stress of stretched films equal to 30 MPa at lower %strain. At lower %strain, film showed higher elasticity than at higher %strain because when the film was drawn continuously, the film entered more deformation zones. Thus, the film possessed higher strength.

4. Conclusions

The stretching process can improve mechanical properties and elasticity as indicated by tensile strength of PBAT and PBAT_E5 films increased by 164% and 186% but elongation at break decreased by 71% and 63% respectively when stretching at the highest ratio (2.5x) due to stretched films are oriented along the uniaxial machine direction and the degree of orientation increased. The elasticity shows in the form of %recovery. %Recovery of stretched PBAT and PBAT_E5 increased when stretching at the highest ratio due to elasticity of films increased. SEM shows surface morphology of stretched PBAT and PBAT_E5 which indicates the longer elongated voids when stretching. It confirmed stretched films are oriented along the uniaxial machine direction. More work needs to be carried out to ensure the application including the coefficient of friction, the shelf-life and the economics analysis of the products.

5. References

BASF. (2013). *Product Information ecoflex® F blend C 1200*. Retrieved from https://www.google.com/url?sa=t&rct=j&q=&esrc=s&source=web&cd=&ved=2ahUKEwikruTnidT3AhVE7XMBHXr4CTEQFnoECAgQAQ&url=https%3A%2F%2Fdocuments.basf.com%2Fc32f5c099d8e29ac42869b975517bdbdda6e62f4&usg=AOvVaw19kOzNTgIMyvLSuz_njoU7

Chen, Y., Han, L., Zhang, H., & Dong, L. (2021). Improvement of the strength and toughness of biodegradable polylactide/silica nanocomposites by uniaxial pre-stretching. *International Journal of Biological Macromolecules*, *190*, 198-205. doi:10.1016/j.ijbiomac.2021.08.218

Deng, Y., Yu, C., Wongwiwattana, P., & Thomas, N. L. (2018). Optimising ductility of poly(lactic acid)/poly(butylene adipate-co-terephthalate) blends through co-continuous phase morphology. *Journal of Polymers and the Environment*, *26*, 3802-3816. doi:10.1007/s10924-018-1256-x

European Bioplastics. (2020). *Bioplastics market data*. Retrieved from https://www.european-bioplastics.org/market/

Hongdilokkul, P., Keeratipinit, K., Chawthai, S., Hararak, B., Seadan, M., & Suttiruengwong, S. (2015). A study on properties of PLA/PBAT from blown film process. *IOP Conference Series: Materials Science and Engineering*, *87*, 012112. doi:10.1088/1757-899x/87/1/012112

Li, X., Yan, X., Yang, J., Pan, H., Gao, G., Zhang, H., & Dong, L. (2017). Improvement of compatibility and mechanical properties of the poly(lactic acid)/poly(butylene adipate-co-terephthalate) blends and films by reactive extrusion with chain extender. *Polymer Engineering and Science*, *58*. doi:10.1002/pen.24795

Likittanaprasong, N., Seadan, M., & Suttiruengwong, S. (2015). Impact property enhancement of poly (lactic acid) with different flexible copolymers. *IOP Conference Series: Materials Science and Engineering*, *87*, 012069.

Suan Sunandha Science and Technology Journal
©2022 Faculty of Science and Technology, Suan Sunandha Rajabhat University

doi:10.1088/1757-899x/87/1/012069

Pietrosanto, A., Scarfato, P., Di Maio, L., & Incarnato, L. (2020). Development of eco-sustainable PBAT-based blown films and performance analysis for food packaging applications. *Materials*, *13*(23), 5395.

Pitivut, S., Suttiruengwong, S., & Seadan, M. (2015). Effect of reactive agent and transesterification catalyst on properties of PLA/PBAT blends. *IOP Conference Series: Materials Science and Engineering*, *87*, 012090. doi:10.1088/1757-899x/87/1/012090

SeedScientific. (2021). *51+ Disturbing plastic waste statistics*. Retrieved from https://seedscientific.com/plastic-waste-statistics/

Su, S., Duhme, M., & Kopitzky, R. (2020). Uncompatibilized PBAT/PLA blends: Manufacturability, miscibility and properties. *Materials*, *13*(21), 4897. doi:10.3390/ma13214897

Available online at http://www.ssstj.sci.ssru.ac.th

Suan Sunandha Science and Technology Journal
©2022 Faculty of Science and Technology, Suan Sunandha Rajabhat University

Barrier and Seal Properties of Reactive Blending of Poly(butylene succinate) Based Blends

Pitakpong Kamrit[1], Manus Seadan[2], Supakij Suttiruengwong[1*]

[1]Department of Materials Science and Engineering, Faculty of Engineering and Industrial Technology, Silpakorn University, Sanam Chandra Palace Campus, Nakhon Pathom 73000, Thailand

[2]Department of Physics, Faculty of Science, Silpakorn University, Sanam Chandra Palace Campus, Nakhon Pathom 73000, Thailand

*Corresponding author e-mail: suttiruengwong_s@su.ac.th

Received: *15 February 2022* / **Revised**: *27 April 2022* / **Accepted**: *26 May 2022*

Abstract

Poly Butylene Succinate (PBS) is one of the biodegradable polymers with good physical properties but its barrier properties such as the oxygen barrier are poor. The aim of this study was to investigate the barrier and seal properties of PBS by blending with biodegradable poly hydroxybutyrate-co-hydroxyvalerate (PHBV). PBS and PHBV (80/20 and 70/30 %w/w) with and without reactive agents were prepared using an internal mixer. Film specimens of 100 micrometers in thickness were prepared using compression molding. The morphology, barrier properties and peel-seal strength were investigated. Morphological observations using scanning electron microscope (SEM) showed an improved dispersion of PHBV in the blends after adding the reactive agents. The oxygen barrier and water vapor barrier were determined using ASTM D3985 and ASTM E96, respectively. The results showed that the addition of PHBV into the blend films led to lower OTR and WVTR when compared to the neat PBS. The addition of reactive agents can further improve the OTR and WVTR of PBS/PHBV blends due to the compact and dense structure of the films. Peel–seal behavior of the films was examined by the different sealing temperatures, which determined the failure mechanism after peeling. The blend films with reactive agents after sealing temperature between 105 and 115°C were peeled from the substrate with adhesive and cohesive failures showing the easy peel mode.

Keywords: Poly(butylene succinate), Poly(hydroxybutyrate-co-hydroxyvalerate), Reactive blending film, Barrier properties, Peelable film

1. Introduction

The growing environmental concern on plastic pollution has gained global attention. It was reported that more than 340 million tons of plastic waste were generated around the world, with around 46% of this waste from the packaging sector in 2018 (Wu, Misra, & Mohanty, 2021). For the food packaging applications, it is a single-use packaging alone that generates a large amount of plastic wastes. Amongst these, the plastic top seal for sealing trays is one of the interesting items, which is difficult to be replaced with the sustainable option. Top seal is mostly made from non-biodegradable polyolefins and poly(ethylene terephthalate) (PET) or even multilayer films. They are not easily recycled and usually sent to landfills after using. With the high material property requirements of these plastics including a light weight (micro-scale thickness), high toughness, complex structures (multi-layer) and contamination due to direct contact with foods (Wu et al., 2021), the collection, separation and recycle are very complicated. Urgent efforts are directed towards finding alternative solutions, including the use of renewable, biobased, and biodegradable plastics (Rodriguez-Uribe et al., 2021). One of the options can be the compostable plastics as they offer the composting option, especially for a food contact packaging, where recycling was complexed by the economics of scale and waste management. For food packaging uses, the poor water vapor and gas barrier properties of most biodegradable plastics are the

Suan Sunandha Science and Technology Journal
©2022 Faculty of Science and Technology, Suan Sunandha Rajabhat University

major limitations for top seal applications. The main approach to improve this performance of biodegradable plastics includes polymer blending. The method is easily adopted in the industrial processes (Wu et al., 2021).

Poly butylene succinate or PBS is one of the biodegradable aliphatic polyester and is synthesized from 1,4-butanediol and succinic acid monomers by the polycondensation reaction. PBS has mechanical properties comparable to polyolefins like polyethylene (PE) and polypropylene (PP) (Muthuraj, Misra, & Mohanty, 2017). On the other hand, the disadvantage of PBS with packaging application is its poor barrier to moisture and oxygen (Rodriguez-Uribe et al., 2021). A study conducted by V. Siracusa et al. (Siracusa, Lotti, Munari, & Dalla Rosa, 2015) reported the oxygen transmission rate (OTR) of PBS films prepared by compression molding and with a thickness of 144.7 μm was ~281 $cm^3.m^{-2}.day^{-1}.bar^{-1}$. J. Xu (Xu, 2015) reported the water vapor transmission rate (WVTR) of PBS films made by using hot-press and with a thickness of 51 μm was 83.8 $g.m^{-2}.day^{-1}$. To obtain high oxygen/water vapor barrier blends, one component with a high barrier should be incorporated. Accordingly, the polymer blending by high barrier properties materials can result in products with better barrier properties. Among biopolymers, Polyhydroxybutyrate-co-hydroxyvalerate (PHBV) as a family of Poly(hydroxyalkanoates) (PHAs) has relatively high barrier properties and proven biodegradability has attracted the attention of the packaging application. This group of polymer is a polyester derived from microorganism, including bacterial fermentation of starting raw sugars or lipids (Nuchanong, Seadan, Khankrua, & Suttiruengwong, 2021; Rodriguez-Uribe et al., 2021). Since the oxygen barrier of PHBV is much better than most biopolymers such as PBS, Polylactic acid (PLA), Polycaprolactone (PCL), and some commodity polymers such as PP and PE, it is a good candidate for blending. This polymer is however still very expensive. Although the water vapor barrier of PHBV was inferior to that of PP and PE, it is clearly better than that of biodegradable polyesters such as PBS, PLA, PBAT and PCL (Rodriguez-Uribe et al., 2021). Thus, PHBV can help to enhance the barrier properties of biopolymer blends. The poor barrier of PLA films has been found to improve with the addition of PHBV by I. Zembouai et al. (Zembouai et al., 2013). The OTR of PLA was decreased by about 35.3, 43.2 and 81.5% with the addition of 25, 50 and 75 wt% of PHBV for PHBV/PLA blend, respectively. On the other hand, the value of WVTR of PLA was decreased by about 22.7, 36.6 and 58.9% by addition of 25, 50 and 75 wt% of PHBV, respectively. M. Cunha et al. (Cunha, Fernandes, Covas, Vicente, & Hilliou, 2016) studied the melt blended PHBV/PBAT (70/30). It was reported that WVP of the film was close to PHBV, but the elongation at break of the film showed the low flexibility. The compatibility between PBS and PHBV was poor, resulting in relatively large particle size and a weak interfacial adhesion in their blends by Y.J. Phua et al. (Phua, Pegoretti, Medeiros Araujo, & Mohd Ishak, 2015) and P. Ma. et al. (Ma, Hristova-Bogaerds, Lemstra, Zhang, & Wang, 2012). Certain compatibility needs to be introduced into the blend system in order to acquire better performance. To achieve oxygen/water vapor barrier and mechanical balance in biodegradable polymer blends, effective compatibilizers were normally applied (Wu et al., 2021).

Therefore, the objective of this work was to study the addition of reactive compatibilizer in 80/20 and 70/30 wt% of PBS and PHBV blend. The polymer blend with and without reactive compatibilizer was evaluated by oxygen transmission rate (OTR), water vapor transmission rate (WVTR) and seal strength test for study the possibility to use with top seal application.

2. Materials and Methods

A commercial grade polybutylene succinate (PBS) FZ91PM with MFR 5 g/10 min, density 1.26 g/cm^3, melting temperature around 115°C was purchased from PTT MCC Biochem Co. Ltd. Thailand). Polyhydroxybutyrate-co-hydroxyvalerate) (PHBV) Enmat Y1000P with 3 mol% hydroxyvalerate (HV) content was purchased from Tianan Biologic Material Co. (Ningbo, P. R. China). It

Suan Sunandha Science and Technology Journal
©2022 Faculty of Science and Technology, Suan Sunandha Rajabhat University

has the density of 1.25 g/cm^3, melting temperature around 175-180°C. Multi-functional epoxy chain extender (ECE) Joncryl ADR 4468 in solid flake form with epoxy equivalent weight 310 g/mol was purchased from BASF Co., Ltd.

2.1 Blend preparation

PBS and PHBV pellets were dried at 60ºC overnight before further use. The ratios of PBS and PHBV were 80:20 and 70:30 by weight. For reactive blending, PBS/PHBV with various contents of ECE were studied at 0.1, 0.2 and 0.3 phr. PBS/PHBV blends with and without reactive agents were melt-blended using an internal mixer at 180°C with rotor speed of 100 rpm for 10 min. Films were prepared using compression molding at 190ºC for 3 min to obtain films of about 100 µm thickness.

2.2 Characterization

Scanning electron microscopy (SEM). To investigate the morphology of PBS/PHBV blends with and without reactive agents, all blended samples were cryo-fractured in liquid nitrogen and sputter coated with Au/Pd. The fracture surface was investigated by Field emission scanning electron microscopy (FESEM) (MIRA3, TESCAN) with a chamber pressure <0.009 Pa under high vacuum mode. A 2500×magnification was used for all samples.

Oxygen transmission rate (OTR). The oxygen transmission rate (OTR) was carried out according to ASTM D3985 using Gas Permeability Tester (type GDP-C, Brugger Feinmechanik GmbH). OTR measurements were performed at 23°C at 50% of RH, and the results were expressed in cm^3.m^{-2}.day^{-1}.bar^{-1}.

Water vapor transmission rate (WVTR). The water vapor transmission rate (WVTR) of the film samples was studied using the "Cup method" referring to ASTM E96. Silica gel was used as a desiccating agent, and the cups had a specific exchange surface of S = 4.59 cm^2. The experimental setting consists of a cylindrical vessel filled with a desiccating agent and sealed with the investigated film. The mass increase in the cups, due to the water absorption of silica gel, was plotted against time. The WVTR was calculated from the slope of the mass uptake of desiccating agent profile versus time at 23°C at 75% of RH, and the results were expressed in g.m^{-2}.day^{-1}.

Seal-Peel test. Heat sealing process involves sealing temperature between 95 and 110°C and sealing time 8 s (18 rpm.) were directly set on a continuous sealing machine (BSV-5I, Tupack Co., Ltd.). All of the films were sealed on a PBS blend sheet. The sheet prepared from PBS/PLA/PBAT was about 800 µm thickness to imitate the container rim or the tray's lip. Peel strength of films was measured by a supported 180° test (Technique C) according to ASTM F88. The grip distance and peeling rate was 25.4 mm and 200 mm/min, respectively. The testing machine was a universal testing machine (NRI-TS500-5B, Narin instrument Co., Ltd.) with a load cell of 5 kN. Peel strength values were the average values of five repeated measurements.

3. Results and Discussion

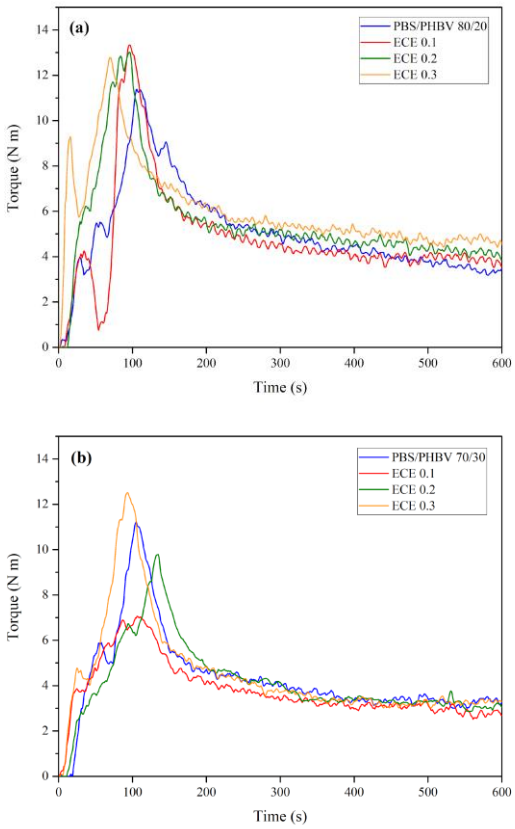

Suan Sunandha Science and Technology Journal
©2022 Faculty of Science and Technology, Suan Sunandha Rajabhat University

Figure 1. Mixing torques of PBS/PHBV (a) 80/20 (b) 70/30 blend with and without reactive agents at 180ºC and rate 100 rpm.

Mixing torque values. The mixing torque of the internal mixer can be related to the molten polymer viscosity. The evolution of PBS/PHBV 80/20, 70/30 blend with and without reactive agents mixing torque curves is shown in Figure 1. The mixing torque curve of the non-reactive PBS/PHBV 80/20 blend is lower than that of the reactive PBS/PHBV 80/20 blend as a result of the reaction between ECE epoxide group and carboxylic end group of polyester through condensation reaction, indicating some degree of chemical reaction. This finding is consistent with other researches that also modified polyester through condensation reaction (Nanthananon, Seadan, Pivsa-Art, Hiroyuki, & Suttiruengwong, 2017; Nuchanong et al., 2021; Phuangmali, Seadan, Khankrua, & Suttiruengwong, 2021; Yang, Xin, Mughal, Li, & He, 2017). The reactive epoxide groups can react with carbonyl groups in both polyesters to form copolymer, leading to better compatibility between two polymers. For PBS/PHBV 70/30 blend (Figure 1 b), the mixing torque was not different when adding and increasing ECE contents. The reason for this might be the expense of two or more competing reactions of PHBV, such as the competition between the degradation reaction and condensation reaction (Nuchanong et al., 2021). Therefore, the change in the viscosity of the melt is not pronounced.

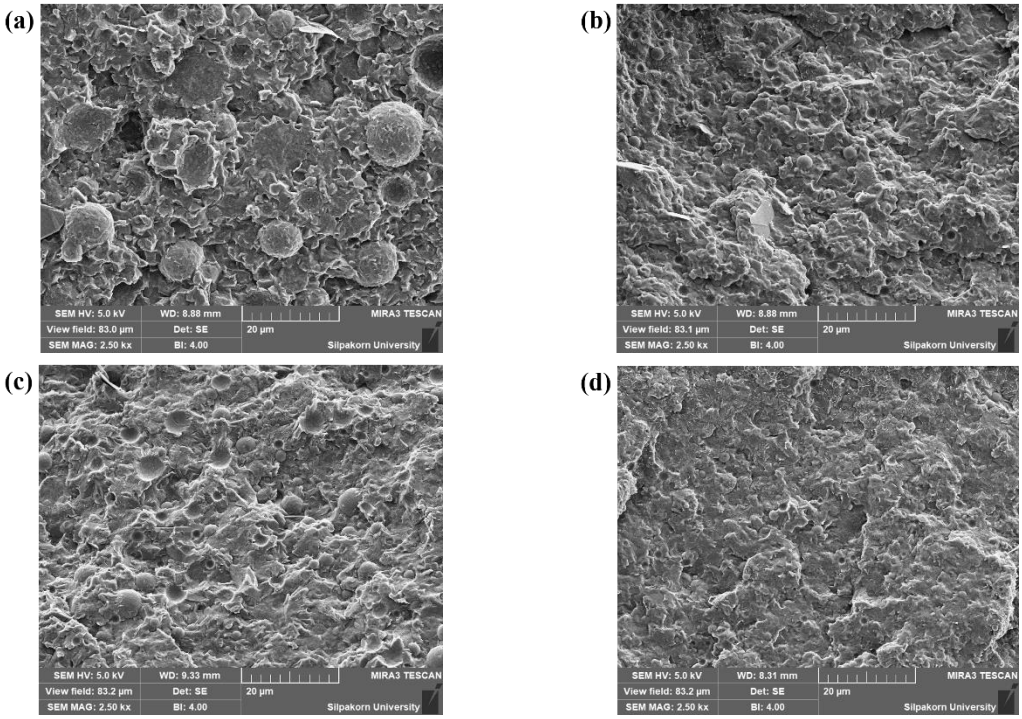

Figure 2. SEM micrographs of cryo-fracture surface of (a) non-reactive PBS/PHBV 80/20 and reactive PBS/PHBV 80/20 with ECE (b) 0.1, (c) 0.2 and (d) 0.3 phr.

Suan Sunandha Science and Technology Journal
©2022 Faculty of Science and Technology, Suan Sunandha Rajabhat University

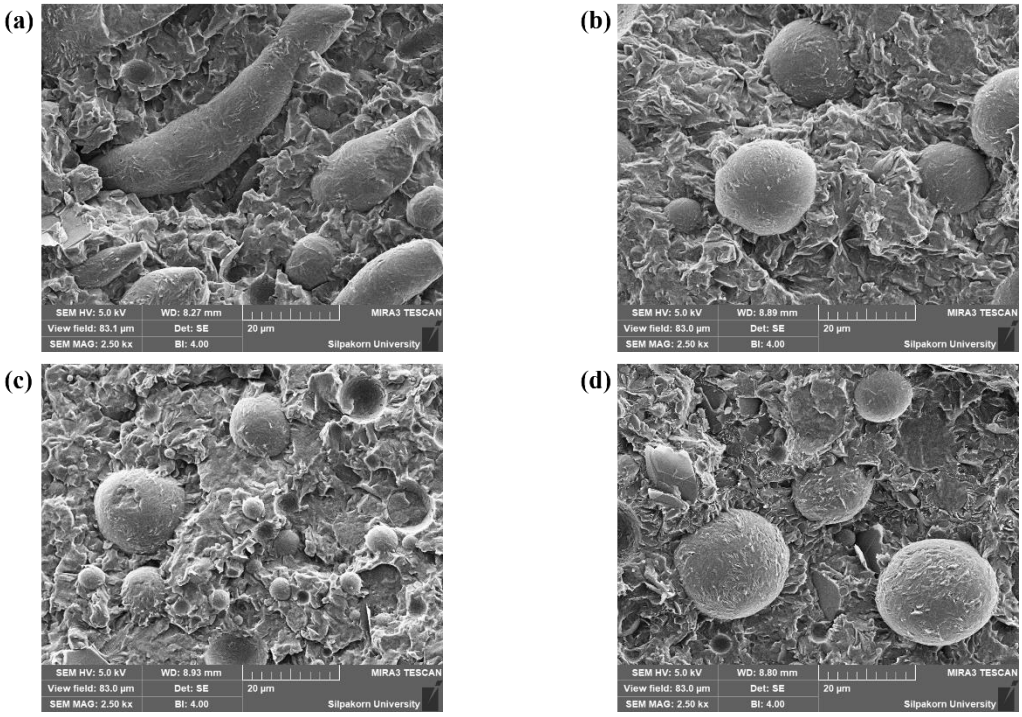

Figure 3. SEM micrographs of cryo-fracture surface of (a) non-reactive PBS/PHBV 70/30 and reactive PBS/PHBV 70/30 with ECE (b) 0.1, (c) 0.2 and (d) 0.3 phr.

Morphological observation. The micrographs of the PBS/PHBV blends are studied by SEM. Figure 2 shows the SEM micrographs of the cryo-fractured surface of the non-reactive and reactive PBS/PHBV (80:20) blends. The physical PBS/PHBV blends (Figure 2 a) shows that PHBV droplets are dispersed in the PBS matrix with an average droplet size of about 10 µm. After addition of ECE to the PBS/PHBV blends (Figure 2 b - d), the sizes of PHBV droplets are smaller than non-reactive one. The particle sizes are about 2 µm. It is evident that there was a reaction through the condensation reaction when adding ECE into the blends. Similar observation was made by I. Zembouai et al. (Zembouai et al., 2013). They reported that PHBV and PLA form mainly a two phase-system. In the 25/75 blend, the phase was formed by PHBV and the inclusions (bead-shaped) were PLA domains. P. Ma and coworker (Ma et al., 2012) also reported after adding of the reactive agent to the PHBV/PBS melts, which acted as compatibilizer between PHBV and PBS and a network consisting of both PHBV and PBS were formed.

In case of the cryo-fractured surfaces of PBS/PHBV (70:30), PHBV is typically dispersed in a form of the filament in the PBS matrix as shown in Figure 3 a. In Figure 3 b, PBS/PHBV (70:30) blend with the addition of the reactive agent showed the spherical particles instead of the filament shape. The filament changes to spherical droplets with a larger particle size of about 20 µm and the smaller about 4-5 µm. The interfacial adhesion between both polymers for both compositions of the blends as depicted in Figure 3 c and Figure 3 d after adding ECE.

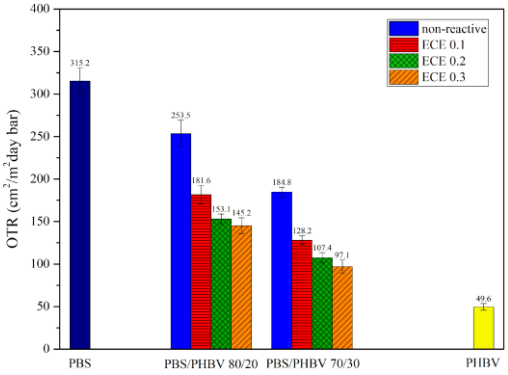

Figure 4. Oxygen transmission rate (OTR) of PBS/PHBV blend with and without reactive agents.

Suan Sunandha Science and Technology Journal
©2022 Faculty of Science and Technology, Suan Sunandha Rajabhat University

Barrier properties. Gas barrier properties of PBS/PHBV blends were investigated by means of oxygen and water vapor transmission rate tests. Evaluations were performed on compressed films with thickness about 100 µm. Similar trends are observed for both gas permeation evolutions as a function of compositions.

Oxygen transmission rate (OTR). The results are depicted in Figure 4 PHBV possesses a good oxygen barrier when compared to PBS. OTR values of PBS/PHBV blend are decreased with increasing PHBV contents in the blends. When adding ECE, the OTR value decreased furthermore when compared to non-reactive PBS/PHBV blends. OTRs of PBS/PHBV 80/20 and 70/30 blend are improved by 54 and 69.2% after the addition of ECE 0.3 phr, respectively compared with that of PBS. The reason for this is still unknown. This shows clearly the role of PHBV as an efficient barrier promoter for PBS, even at the low content. The lower OTR values obtained after adding ECE suggest an improved interfacial adhesion between both polymers helps create the compact and dense structure of the films (Chinga-Carrasco & Syverud, 2012).

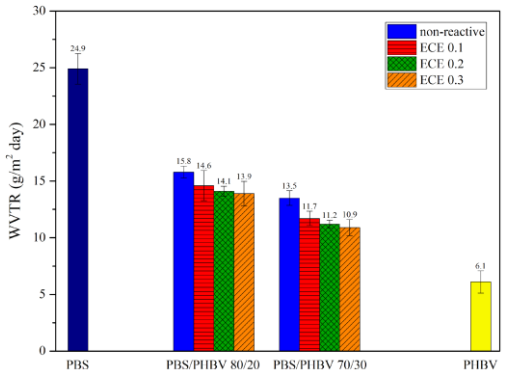

Figure 5. Water vapor transmission rate (WVTR) of PBS/PHBV blend with and without reactive agents.

Water vapor transmission rate (WVTR). WVTR results are presented in Figure 5. It is seen that by increasing PHBV contents the water vapor barrier was better when compared to PBS alone. PBS/PHBV blends show the decrease in WVTR values with increasing PHBV contents. Moreover, OTR of reactive PBS/PHBV blends exhibit lower than that of non-reactive blends. WVTR values of PBS/PHBV 80/20 and 70/30 blend compared with PBS are improved by 44 and 55.6% after the addition of ECE 0.3 phr, respectively. The incorporation of PHBV can improve the moisture barrier properties of PBS. This was also in good agreement with I. Zembouai (Zembouai et al., 2013), who reported the barrier property of PHBV and PLA blend. After improving the barrier properties of the blends, it was found that barrier properties lied between PLA and PHBV barrier properties. It was reported that the decrease in barrier properties as crystallinity increased was mainly explained by two factors. The first was the inclusion of impermeable crystallites which decreases the amount of amorphous phase through which the gas molecules can permeate. The second was that impermeable crystals increase the tortuosity of the transport path (Zembouai et al., 2013).

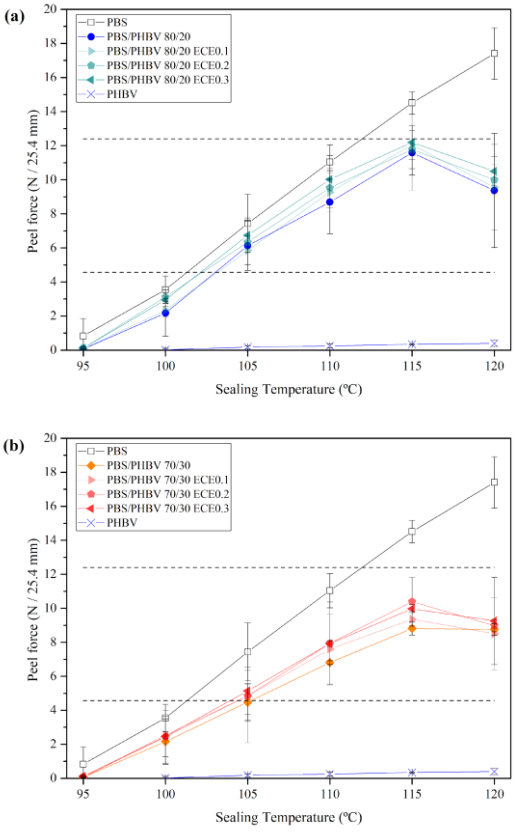

Figure 6. Peel force of (a) PBS/PHBV 80/20 blends and (b) PBS/PHBV 70/30 blends with and without

Suan Sunandha Science and Technology Journal
©2022 Faculty of Science and Technology, Suan Sunandha Rajabhat University

ECE in different sealing temperatures on PBS blends sheet.

Seal-Peel test. In this research, PBS/PHBV films were fabricated and used to investigate the peel properties as for an easy-peel range application. The peel force of the film sealed on the prepared PBS blend sheet was carried out to evaluate the interaction between PBS/PHBV films and PBS blend sheet. From the seal and Peel test shown in Figure 6, Peel force tends to decrease with increasing PHBV contents. The compact and dense structure of the films could be the reason for this. On the other hand, depending on the preparation of the films (in this case the compression molding was used), PHBV minor phases can reside at the surface because of its low interaction with PBS (Liewchirakorn, Aht-ong, & Chinsirikul, 2017). Since the heat seal was studied, optimum heat seal temperatures of some of the blends may fall out of this range. Therefore, the blends could be used in packaging applications with easy-open peelable features (in-dash lines), which have a peel force of 4.45-12.24 N/25.4 mm (1 to 2.75 lb/in as reported by reported by J. Zhang et al.) (Diaz, Pao, & Kim, 2016; Zhang et al., 2009). However, all blends film at sealing temperature 105 and 115ºC had a tendency to be used as peelable film for easy-peel films.

Peel-seal behaviors in easy-peel range with different sealing temperatures (105-115ºC) peeling film from PBS blend sheet substrate (800 µm). Three types of the film's failure (Liewchirakorn et al., 2017) observed in this study are schematically illustrated in Figure 7 a to c. Adhesive failure was found in sealed PBS/PHBV 80/20 blend at 105-110 ºC sealing temperatures and in 70/30 blend at 105 ºC sealing temperatures on PBS blend substrate. This failure is located at the interface between the film and substrate, resulting in the lowest peel force values. For the cohesive failure, the film tends to peel off from the substrate and peel advances during the test. There is some residue observed on both peeled surfaces of PBS blend substrate and PBS/PHBV blend films. This found in the case of the PBS/PHBV 80/20 and 70/30 blend films were sealed at 115ºC, 110ºC, respectively. The films demonstrate tearing failures at a high sealing temperature of 115°C. PBS/PHBV 70/30 blend films exhibit the complete tear. This tearing failure means no peel during the peeling process due to a high seal force between film and substrate (or seal strength is higher than the inherent tensile strength of the film).

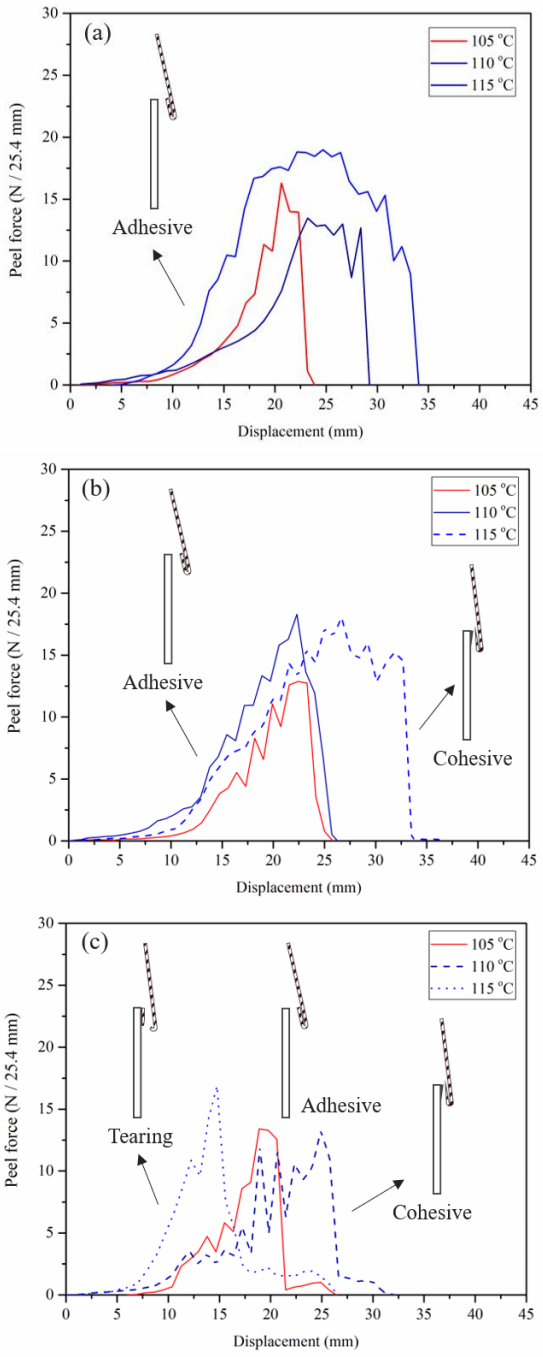

Figure 7. Typical peel failure curve of (a) PBS, PBS/PHBV blends (b) 80/20 and (c) 70/30 in different sealing temperatures on PBS blends sheet.

Suan Sunandha Science and Technology Journal
©2022 Faculty of Science and Technology, Suan Sunandha Rajabhat University

4. Conclusions

Biodegradable PBS and PHBV blends were prepared by melt mixing with and without ECE. Film specimens were prepared using compression molding. The SEM images indicated the decreased PHBV dispersed phase as well as improved interfacial adhesion after adding ECE in PBS/PHBV blends, indicating improved compatibility between these polymers. The addition of PHBV into the blend films without ECE altered the barrier properties, where the decrease in both OTR and WVTR when compared with the neat PBS was observed. Meanwhile, the addition of ECE can further improve the OTR and WVTR of PBS/PHBV blends due to the compact and dense structure of the films. PHBV could act as an efficient barrier promoter for PBS. For the seal-peel strength test, after sealing temperature between 105 and 115°C that exhibited easy-peel characteristics. Peel–seal behaviors in an easy-peel range were peeled from the PBS blend substrate, adhesive and cohesive failures were apparent during the peeling process. It can be concluded that the blend film with PHBV minor phase with ECE can be used for top seal application.

5. Acknowledgement

The authors greatly acknowledge the financial support provided by the Department of Materials Science and Engineering, Faculty of Engineering and Industrial Technology, Silpakorn University.

6. References

Chinga-Carrasco, G., & Syverud, K. (2012). On the structure and oxygen transmission rate of biodegradable cellulose nanobarriers. *Nanoscale Research Letters*, *7*(1), 192. doi:10.1186/1556-276X-7-192

Cunha, M., Fernandes, B., Covas, J. A., Vicente, A. A., & Hilliou, L. (2016). Film blowing of PHBV blends and PHBV-based multilayers for the production of biodegradable packages. *Journal of Applied Polymer Science*, *133*(2). doi:10.1002/app.42165

Diaz, C., Pao, H. Y., & Kim, S. (2016). Film performance of poly(lactic acid) blends for packaging applications. *Journal of Applied Packaging Research*, *8*, 4.

Liewchirakorn, P., Aht-ong, D., & Chinsirikul, W. (2017). Practical approach in developing desirable peel-seal and clear lidding films based on poly(lactic acid) and poly(butylene adipate-co-terephthalate) blends. *Packaging Technology and Science*, *31*. doi:10.1002/pts.2321

Ma, P., Hristova-Bogaerds, D. G., Lemstra, P. J., Zhang, Y., & Wang, S. (2012). Toughening of PHBV/PBS and PHB/PBS blends via in situ compatibilization using dicumyl peroxide as a free-radical grafting initiator. *Macromolecular Materials and Engineering*, *297*(5), 402-410. doi:10.1002/mame.201100224

Muthuraj, R., Misra, M., & Mohanty, A. (2017). Biodegradable compatibilized polymer blends for packaging applications: A literature review. *Journal of Applied Polymer Science*, *135*. doi:10.1002/app.45726

Nanthananon, P., Seadan, M., Pivsa-Art, S., Hiroyuki, H., & Suttiruengwong, S. (2017). Biodegradable polyesters reinforced with eucalyptus fiber: Effect of reactive agents. *AIP Conference Proceedings*, *1914*(1), 070012. doi:10.1063/1.5016739

Nuchanong, P., Seadan, M., Khankrua, R., & Suttiruengwong, S. (2021). Thermal stability enhancement of poly(hydroxybutyrate-co-hydroxyvalerate) through in situ reaction. *Designed Monomers and Polymers*, *24*(1), 113-124. doi:10.1080/15685551.2021.1914406

Phua, Y. J., Pegoretti, A., Medeiros Araujo, T., & Mohd Ishak, Z. A. (2015). Mechanical and thermal properties of poly(butylene succinate)/poly(3-hydroxybutyrate-co-3-hydroxyvalerate) biodegradable blends. *Journal of Applied Polymer Science*, *132*(47). doi:10.1002/app.42815

Phuangmali, I., Seadan, M., Khankrua, R., & Suttiruengwong, S. (2021). Reactive compatibilization of poly(hydroxybutyrate-co-hydroxyvalerate)/polyvinyl alcohol blends. *Polymer-Plastics Technology and Materials*, *60*(13), 1461-1473. doi:10.1080/25740881.2021.1918162

Suan Sunandha Science and Technology Journal
©2022 Faculty of Science and Technology, Suan Sunandha Rajabhat University

Rodriguez-Uribe, A., Wang, T., Pal, A. K., Wu, F., Mohanty, A. K., & Misra, M. (2021). Injection moldable hybrid sustainable composites of BioPBS and PHBV reinforced with talc and starch as potential alternatives to single-use plastic packaging. *Composites Part C: Open Access*, *6*, 100201. doi:10.1016/j.jcomc.2021.100201

Siracusa, V., Lotti, N., Munari, A., & Dalla Rosa, M. (2015). Poly(butylene succinate) and poly(butylene succinate-co-adipate) for food packaging applications: Gas barrier properties after stressed treatments. *Polymer Degradation and Stability*, *119*, 35-45. doi:10.1016/j.polymdegradstab.2015.04.026

Wu, F., Misra, M., & Mohanty, A. K. (2021). Challenges and new opportunities on barrier performance of biodegradable polymers for sustainable packaging. *Progress in Polymer Science*, *117*. doi:10.1016/j.progpolymsci.2021.101395

Xu, J. (2015). *Biobased nanocomposites for packaging applications - synthesis using melt extrusion of poly (lactic acid), poly (butylene succinate) and/or starch blended with natural nanofillers* (Master's thesis). Kansas State University. Retrieved from http://hdl.handle.net/2097/20561

Yang, Z., Xin, C., Mughal, W., Li, X., & He, Y. (2017). High-melt-elasticity poly(ethylene terephthalate) produced by reactive extrusion with a multi-functional epoxide for foaming. *Journal of Applied Polymer Science*, *135*, 45805. doi:10.1002/app.45805

Zembouai, I., Kaci, M., Bruzaud, S., Benhamida, A., Corre, Y.-M., & Grohens, Y. (2013). A study of morphological, thermal, rheological and barrier properties of poly(3-hydroxybutyrate-co-3-hydroxyvalerate)/polylactide blends prepared by melt mixing. *Polymer Testing*, *32*(5), 842-851. doi:10.1016/j.polymertesting.2013.04.004

Zhang, J., Manias, E., Polizos, G., Huh, J.-Y., Ophir, A., Songtipya, P., & Jimenez-Gasco, M. d. M. (2009). Tailored polyethylene nanocomposite sealants: Broad-range peelable heat-seals through designed filler/polymer interfaces. *Journal of Adhesion Science and Technology*, *23*(5), 709-737. doi:10.1163/156856108X379182

Available online at http://www.ssstj.sci.ssru.ac.th

Suan Sunandha Science and Technology Journal
©2022 Faculty of Science and Technology, Suan Sunandha Rajabhat University

Properties of Ternary Blends of Compostable PLA/PBAT/PBS

Sarocha Chuakhao[1], Manus Seadan[2], Supakij Suttiruengwong[1,*]

[1]Department of Materials Science and Engineering, Faculty of Engineering and Industrial Technology, Silpakorn University, Nakhon Pathom 73000, Thailand

[2]Department of Physics, Faculty of Science, Silpakorn University, Nakhon Pathom 73000, Thailand

*Corresponding author e-mail: Chuakhao_S@su.ac.th, Manus_sc.su@hotmail.com, suttiroengwong_s@su.ac.th

Received: *16 February 2022* / **Revised**: *1 March 2022* / **Accepted**: *14 June 2022*

Abstract

Compostable plastics such as Poly (lactic acid) (PLA), Poly(butylene succinate) (PBS) and Poly(butylene adipate-co-terephthalate) (PBAT) have been extensively used in many applications, from commodity to engineering ones. These plastics offer the circularity of the carbon cycle. However, each of them has advantages and disadvantages. The ternary blend of these three are therefore very interesting in terms of phase morphology and their physical properties while offering compostable practices. In this work, the blends of PLA/PBAT/PBS were studied. PLA/PBAT was fixed at 50/50 whereas PBS was varied from 10 to 40 % wt. In order to ensure the compatibility, peroxide and carbodiimide compounds were used. The results show an immiscibility of PLA/PBAT/PBS blend, with continuous surface of PLA and PBAT while PBS is dispersed phase. However, it shows the better interfacial adhesion of PLA/PBAT/PBS when reactive compounds were added. The mechanical properties indicated the modulus of all blends higher than neat PBAT (~52 MPa) and PBS (~377 MPa). However, it insignificantly changed when increased PBS contents, similar to the tensile strength results.

Keywords: Circularity, Ternary blend, Compostable plastic

1. Introduction

There is a great concern on accumulative plastic waste. Many existing solutions include the new plastics economy pioneered by Ellen MacArthur (Ellen MacArthur Foundation, 2020). Plastics and circular economy have been put into the solutions in forms of the new design of products and processes as well as the materials substitution. In terms of materials regeneration and sustainability, biobased and biodegradable plastics are obvious choices. Depending on the applications, materials can be selected and designed for circularity. Thus, one of the options for plastics can be compostable plastic, which can provide the composting option and return carbon and nutrients for the plant growth. Among compostable plastics, poly(lactic acid) (PLA) is one of the most studied one because it has many advantages such as high strength, high modulus, biodegradable and low cost as well as commercialization on a large scale. However, PLA is highly brittle and has low toughness and heat distortion temperature and barrier properties beside limited application (Chaiwutthinan, Chuayjuljit, Srasomsub, & Boonmahitthisud 2019; Hongdilokkul et al., 2015; Pitivut, Suttiruengwong, & Seadan, 2015; F. Wu, Misra, & Mohanty, 2020).

Many researchers have attempted to improve the properties of PLA to make it more widely applicable. One method that is widely used for improving the toughness of PLA is to blend PLA with a flexible polymer such as PBAT and PBS (Hongdilokkul et al., 2015; Pitivut et al., 2015; Prasong, Ishigami, Thumsorn, Kurose, & Ito, 2021; D. Wu et al., 2020). Poly(butylene adipate-co-terephthalate) (PBAT) is aliphatic aromatic polyester. Although PBAT has been commercialized with high toughness and flexibility, it still has low modulus (D. Wu et al., 2020). Therefore, blending PLA and PBAT can balance these properties. P. Chaiwutthinan et al. (2019) and Pitivut et al. (2015) studied the properties of PLA/PBAT blends in different ratios. The results showed that the addition of PBAT could improve

Suan Sunandha Science and Technology Journal
©2022 Faculty of Science and Technology, Suan Sunandha Rajabhat University

elongation at break of PLA while young's modulus and strength decreased with increased PBAT contents.

A few studies have involved in the blending of PLA and PBS, as PBS was a biodegradable polymer with good processability, high flexibility, high impact strength and better heat resistance compared to other biopolymer such as PLA and PBAT (Prasong et al., 2021; Ravati & Favis, 2013). Prasong et al. (2021) reported that PBS acted as a nucleating agent of PLA and induce. crystallinity in PLA/PBS blend. Improving the crystallinity of the polymer resulted in an increase in the heat resistance of the blend. However, a study of ternary blends between PLA/PBAT/PBS has been limited up to our knowledge. Ravati, Beaulieu, Zolali, and Favis (2014) studied properties of the PBS/PLA/PBAT ternary blend in the equal ratio. SEM micrograph showed all phases were percolated and created a tri-continuous ternary PLA/PBS/ PBAT immiscible blend. The presence of this microstructure resulted in the ternary blend showing a very high level of properties including a high impact strength, high young's modulus, and high elongation at break. F. Wu, Misra, and Mohanty (2019) developed super toughened poly(lactic acid)-based ternary blends via enhancing interfacial compatibility. The results showed that the incorporation of PLA ensured that the blend with modulus above 1 GPa and strength above 30 MPa. In addition, the modulus increased with increased peroxide contents. On the other hand, the addition of peroxide into ternary blends resulted in the molecular chains with highly branched or cross-linked structures. It limited the chain movement, leading to the decreased elongation at break.

According to literature, the effect of PBS content on the properties of PLA/PBAT/PBS ternary blends has not been reported before. Therefore, the objective of this research was to study the effect of PBS content on the phase morphology and physical properties of PLA/PBAT/PBS ternary blends with and without reactive agent.

2. Materials and Methods

2.1 Materials

Poly(lactic acid) (PLA) 4043D grade was purchased from BC POLYMER MARKETING CO., LTD., Thailand. Poly(butylene adipate-co-terephthalate) (PBAT) Ecoflex F blend C1200 was purchased from POLYMATS CO., LTD., Thailand. Poly(butylene succinate) (PBS) FZ91PM grade was purchased from PTT MCC Biochem CO., LTD., Thailand. Di (tert-butylperoxyisopropyl) benzene (perkadox 14s) was purchased from AkzoNobel Co., Ltd. Bioadimide 100XT and 500XT were purchased from Optimal Tech CO., LTD., Thailand.

2.2 Preparation of PLA/PBAT/PBS blends

Prior to usage, PLA PBAT and PBS resin were dried in an oven at 60ºC for 6 hours to remove moisture. Then PLA PBAT and PBS were blended via internal mixer (CHAREON TUT CO., LTD) at 190 ºC with rotor speed 60 rpm for 10 min. The compositions of PLA/PBAT/PBS ternary blends both with and without reactive agents in this study were listed in table 1. PLA/PBAT ratio was fixed at 50/50 while PBS varied from 10 to 40 % wt. Perkadox (Per) and bioadimide (BioAd) 0.2 and 0.4 phr respectively were used for each of compositions to form reactive blended polymers.

Table 1. Compositions of PLA/PBAT/PBS blends.

Sample	PLA (%wt)	PBAT (%wt)	PBS (%wt)	Per (phr)	BioAd (phr)
Neat PLA	100	-	-	-	-
Neat PBAT	-	100	-	-	-
Neat PBS	-	-	100	-	-
PBS0	50	50	-	-	-
PBS10	45	45	10	-	-
PBS20	40	40	20	-	-
PBS30	35	35	30	-	-
PBS40	30	30	40	-	-
PBS0P0.2B0.4	50	50	-	0.2	0.4
PBS10P0.2B0.4	45	45	10	0.2	0.4
PBS20P0.2B0.4	40	40	20	0.2	0.4
PBS30P0.2B0.4	35	35	30	0.2	0.4
PBS40P0.4B0.4	30	30	40	0.2	0.4

Suan Sunandha Science and Technology Journal
©2022 Faculty of Science and Technology, Suan Sunandha Rajabhat University

2.3 Characterization

Melt flow index (MFI) of all samples was measured at 190ºC/2.16 kg, according to ASTM D1238 using Plastomer: MFR1 (CHAREON TUT CO., LTD). The cryo-fracture surface morphology of neat polymers and their blends was examined by Field emission scanning electron microscope (FESEM) (MIRA3, TESCAN) operated at 5.0 KV and samples were sputtered with gold. Young's modulus, tensile strength, and elongation at break of all samples were determined according to ASTM D638-5 with a crosshead speed of 10 mm/min using universal testing machine (NRI-TS501-1508-5B, NARIN instrument CO., LTD).

3. Results and Discussions

3.1 Mixing torque

Mixing torque at 10 min of the sample with and without reactive agents is shown in figure 1. The mixing torque of neat PLA PBAT and PBS are 8.49, 10.18 and 5.46 Nm respectively. The mixing torques imply the melt viscosity of polymers. Therefore, PBAT has the highest melt viscosity whereas PBS has the lowest melt viscosity. Considering the mixing torques of the blends without reactive agent, the results showed that mixing torques decreased with increased PBS contents. On the other hand, the torque value of the blends with reactive agents increases with increasing PBS content due to Perkadox being highly reactive with PBS, resulting in molecular chain cross-linking (Cherykhunthod, Seadan, & Suttiruengwong, 2015; F. Wu et al., 2019). In addition, the presence of bioadimide as a chain extender can also increase the viscosity of the polymer. Thereby, increasing viscosity of the system led to higher torque value.

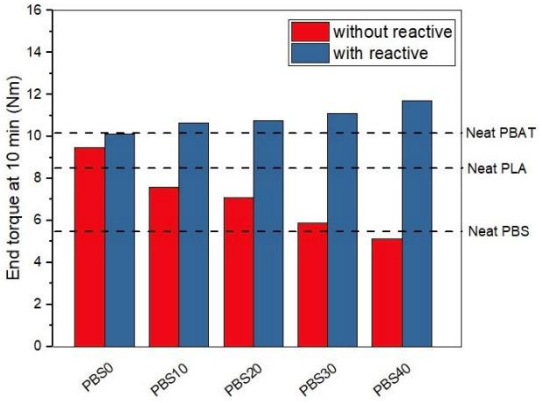

Figure 1. Mixing torque at 10 min of neat polymers and their blends with various PBS contents.

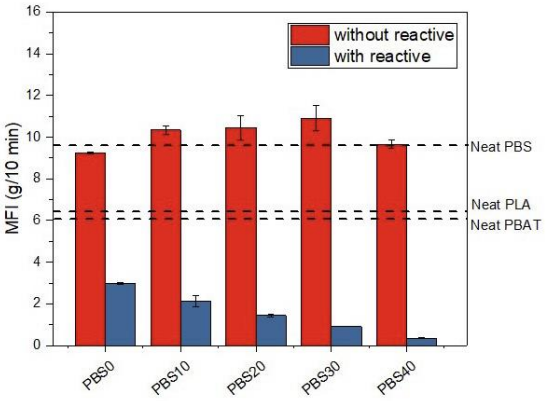

Figure 2. Melt flow index of neat polymers and their blends with various PBS contents.

3.2 Melt flow index

Figure 2 shows the melt flow index of neat polymers and their blends. The results showed MFI of neat PLA PBAT and PBS were 6.45, 6.08 and 9.58 g/10min respectively. In the case of the blends without reactive agent, MFI was increased with increasing PBS contents whereas MFI of the blends with reactive agent decreased with increasing PBS contents. This result is in a good agreement with the mixing torque. That is, polymers with high torque values would have low MFI or high viscosity.

Suan Sunandha Science and Technology Journal
©2022 Faculty of Science and Technology, Suan Sunandha Rajabhat University

(3a)

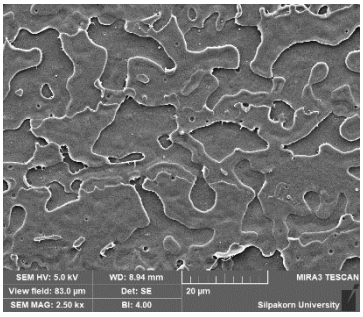

(3b)

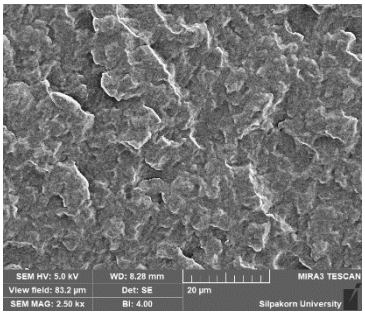

(3c)

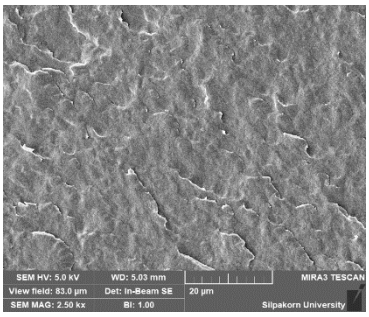

Figure 3. Cryo-fracture surface of (a) neat PLA, (b) neat PBS, (c) neat PBAT by SEM.

3.3 Morphology

SEM micrographs of neat polymers were shown in Figure 3. Neat PLA shows a smooth surface, indicating the brittle characteristic, while neat PBS and PBAT show a relatively rough fracture surface. Figure 4a and 4b show the morphology of the blends with PBS 10 and 20 %wt respectively and without reactive agent. The result indicated an immiscibility of PLA/PBAT/PBS blends, with smooth continuous surface, probably PLA phase while rough continuous surface, probably PBAT phase. In addition, PBS as minor content is dispersed. In case of the blends with reactive agent (Figure 4c and 4d), the morphology changed, indicating that adding perkadox was able to improve interfacial adhesion of the ternary blends. Therefore, the blends exhibited a more uniform surface and dispersed phase was smaller.

(4a)

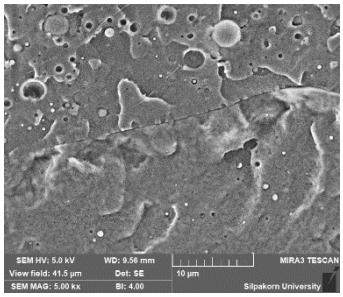

(4b)

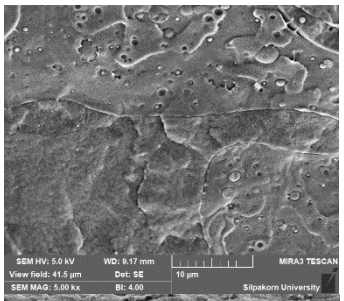

(4c)

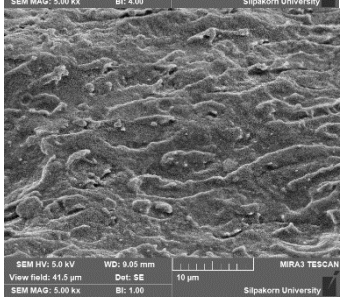

(4d)

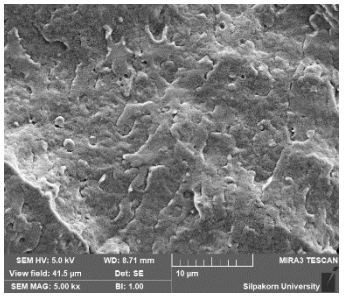

Figure 4. Cryo-fracture surface of (a) PBS10, (b) PBS20, (c) PBS10P0.2B0.4 and (d) PBS20P0.2B0.4 by SEM.

3.4 Mechanical properties

Young's modulus of all samples is shown in figure 5a. The results show that neat PLA had a high modulus (~1,574 MPa) while neat PBAT had a low modulus (~52 MPa). Blending PLA and PBAT in the ratio 50:50 resulted in modulus between both polymers. The blends combined with PBS had lower

Suan Sunandha Science and Technology Journal
©2022 Faculty of Science and Technology, Suan Sunandha Rajabhat University

modulus values. In addition, the modulus of all blends was higher than neat PBS (~377 MPa). However, it insignificantly changed when increased PBS content, similar to the tensile strength results (Figure 5b). Conversely, the elongation at break of all blends decreased with increased PBS content. Moreover, the addition of reactive agent resulted in lower elongation at break compared to the blends without reactive agent due to perkadox causing crosslinked or branched molecular chains (F. Wu et al., 2019).

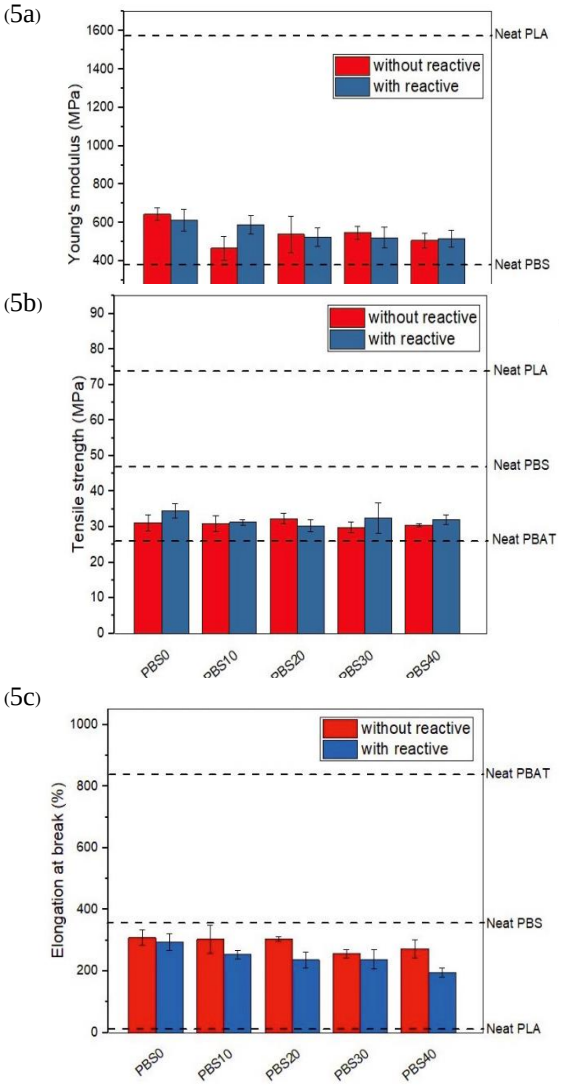

Figure 5. (a) Young's modulus, (b) tensile strength and (c) elongation at break of neat polymers and their blends with various PBS content.

4. Summary

In this work, ternary blends of compostable PLA/PBAT/PBS which fixed PLA/PBAT at 50/50 and varier PBS from 10 to 40 %wt were prepared via internal mixer at 190ºC for 10 min with rotor speed 60 rpm. Mixing torques of the blends increase after reactive agents were applied, indicating an increased melt viscosity. From morphology study, it represents the better interfacial adhesion of PLA/PBAT/PBS when reactive agents were added. In addition, the tensile modulus and strength differ insignificantly upon increasing PBS content. From all the experimental results mentioned above, it may not be clear what proportion of PLA/PBS/PBAT is the optimum. More studies on the phase behavior and crystal structure of the ternary blends are needed to explain the mechanical properties. In addition, this research can be further developed for various packaging applications.

5. References

Chaiwutthinan, P., Chuayjuljit, S., Srasomsub, S., & Boonmahitthisud, A. (2019). Composites of poly(lactic acid)/poly(butylene adipate-co-terephthalate) blend with wood fiber and wollastonite: Physical properties, morphology, and biodegradability. *Journal of Applied Polymer Science*, *136*. doi:10.1002/app.47543

Cherykhunthod, W., Seadan, M., & Suttiruengwong, S. (2015). Effect of peroxide and chain extender on mechanical properties and morphology of poly (butylene succinate)/poly (lactic acid) blends. *IOP Conference Series: Materials Science and Engineering*, *87*, 012073. doi:10.1088/1757-899x/87/1/012073

Ellen MacArthur Foundation. (2020). *Circular economy*. Retrieved from http:// www. ellenmacarthurfoundation.org

Hongdilokkul, P., Keeratipinit, K., Chawthai, S., Hararak, B., Seadan, M., & Suttiruengwong, S. (2015). A study on properties of PLA/PBAT from blown film process. *IOP Conference Series: Materials Science and Engineering*, *87*, 012112. doi:10.1088/1757-899x/87/1/012112

Pitivut, S., Suttiruengwong, S., & Seadan, M. (2015). Effect of reactive agent and transesterification catalyst on properties of PLA/PBAT blends.

Suan Sunandha Science and Technology Journal
©2022 Faculty of Science and Technology, Suan Sunandha Rajabhat University

IOP Conference Series: Materials Science and Engineering, *87*, 012090. doi:10.1088/1757-899X/87/1/012090

Prasong, W., Ishigami, A., Thumsorn, S., Kurose, T., & Ito, H. (2021). Improvement of interlayer adhesion and heat resistance of biodegradable ternary blend composite 3D printing. *Polymers*, *13*(5), 740. doi:10.3390/polym13050740

Ravati, S., Beaulieu, C., Zolali, A. M., & Favis, B. D. (2014). High performance materials based on a self-assembled multiple-percolated ternary blend. *AIChE Journal*, *60*, 3005-3012. doi:10.1002/aic.14495

Ravati, S., & Favis, B. D. (2013). Tunable morphologies for ternary blends with poly(butylene succinate): Partial and complete wetting phenomena. *Polymer*, *54*(13), 3271-3281. doi:https://doi.org/10.1016/j.polymer.2013.04.005

Wu, D., Huang, A., Fan, J., Xu, R., Liu, P., Li, G., & Yang, S. (2020). Effect of blending procedures and reactive compatibilizers on the properties of biodegradable poly(butylene adipate-co-terephthalate)/poly(lactic acid) blends. *Journal of Polymer Engineering*, *41*. doi:10.1515/polyeng-2020-0161

Wu, F., Misra, M., & Mohanty, A. K. (2019). Super toughened poly(lactic acid)-based ternary blends via enhancing interfacial compatibility. *ACS Omega*, *4*, 1955-1968. doi:10.1021/acsomega.8b02587

Wu, F., Misra, M., & Mohanty, A. K. (2020). Tailoring the toughness of sustainable polymer blends from biodegradable plastics via morphology transition observed by atomic force microscopy. *Polymer Degradation and Stability*, *173*, 109066. doi:10.1016/j.polymdegradstab.2019.109066

Available online at http://www.ssstj.sci.ssru.ac.th

Suan Sunandha Science and Technology Journal
©2022 Faculty of Science and Technology, Suan Sunandha Rajabhat University

Synthesis of Copper Nanoparticles-polyvinylpyrrolidone Composite Materials Using Simultaneous Irradiation Process

Thanawat Kasemsankidakarn[1,2], Parichart Kongkaoroptham[2], Thananchai Piroonpan[2], Wanvimol Pasanphan[1,2*]

[1]Department of Materials Science, Faculty of Science, Kasetsart University, 50 Ngam Wong Wan Rd., Ladyao, Chatuchak, Bangkok 10900, Thailand

[2]Center of Radiation Processing for Polymer Modification and Nanotechnology (CRPN), Faculty of Science, Kasetsart University, 50 Ngam Wong Wan Rd., Ladyao, Chatuchak, Bangkok 10900, Thailand

*Corresponding author e-mail: wanvimol.p@ku.ac.th

Received: *28 February 2022* / **Revised**: *16 March 2022* / **Accepted**: *14 June 2022*

Abstract

An approach for the synthesis of copper nanoparticles (CuNPs) embedded in poly (vinylpyrrolidone) (PVP) composite materials is proposed using a simultaneous irradiation process. The parameters, i.e., copper sulfate (CuSO4) precursor, VP and PVP concentrations were optimized for synthesis of CuNPs under irradiation. Crosslinking of PVP system was analyzed by gel fraction and swelling degree using gravimetric measurement. Functionality, chemical composition and crystallinity of the CuNPs-PVP composite materials were characterized by FT-IR, SEM-EDS, XRD. Morphology of the CuNPs-PVP composite materials was observed using SEM. Light blue color of Cu^{2+} precursor in liquid polymer/monomer system changed to dark brown color of Cu in solid form. Stable CuNPs with the particle diameters ranging from ca.100 to 500 nm was successfully synthesized in the PVP solid materials. A simple and effective process for the preparation of the CuNPs-PVP composite materials serves as a new generation of process and functional nanomaterials for industrial applications.

Keywords: Copper nanoparticles, Poly (vinylpyrrolidone), Nanocomposite, Irradiation

1. Introduction

Copper nanoparticles (CuNPs) are metal materials in a nano-sized scale (<100 nm) having high surface area to volume ratio resulting in strong electrical conductivity (Athanassiou, Grass, & Stark, 2006) catalytic property and antibacterial activity (Wahyudi, Soepriyanto, Mubarok, & Sutarno, 2018). CuNPs are considered as one of the alternative materials for replacing other bulk metallic materials because it has lower price than gold and silver, etc., (Cheng et al., 2017; Tomotoshi & Kawasaki, 2020). For example, it has been used as conductive fabrics (Moazzenchi & Montazer, 2020), catalysts, antibacterial agents and pigments (Athanassiou et al., 2006) in various applications. In case of soldering connections, conductive paste has valuable applications in the electronic industry, such as printed circuits and circuit repair (Zinn et al., 2012). However, CuNPs have high oxygen sensitivity which will then aggregate and be readily oxidized by oxygen in an aqueous environment, high humidity and air environment (Wahyudi et al., 2018). Therefore, several strategies for the synthesis of CuNPs by reducing oxidation in order to develop stable CuNPs for desirable applications is still in the line of scientific and technological development.

Many approaches for synthesizing CuNPs are based on the reduction process of Cu(II) ions as a precursor to CuNPs. Up to present, the process for the synthesis of CuNPs includes chemical reduction using various chemical reducing agents (Chandra, Kumar, & Tomar, 2014), photo-induced reduction (Giuffrida, Costanzo, Ventimiglia, & Bongiorno, 2008), sonochemical (Wongpisutpaisan, Charoonsuk, Vittayakorn, & Pecharapa, 2011) and

Suan Sunandha Science and Technology Journal
©2022 Faculty of Science and Technology, Suan Sunandha Rajabhat University

radiolytic methods (Zhou et al., 2008). The benefits of radiolytic synthesis of metal NPs are chemical reducing agent free, size controllable, simultaneous reaction and fabrication, practical, and easiness (Flores-Rojas, López-Saucedo, & Bucio, 2020). Ionizing radiations generate the reactive species (e.g., solvated electrons, ions and free radicals) in a controlled synthetic system. The solvated electrons have an incredibly negative redox potential and they play an important role as a source of reducing agent to promote reduction reaction (Joshi, Patil, Iyer, & Mahumuni, 1998). This brings about the phenomena causing reduction of metal ions to their zero valent state. Metal cluster properties are often affected by the interaction between the metal and the surrounding molecules (e.g., solvent, ligand, stabilizer). In contrast to chemical reduction of metal ions, the radiation chemical process for colloid preparation has significant benefits in that there are no irritating impurities such as chemical reducing agents. Radiolysis process produces pure and enables the creation of stable nanoparticles by controlling the stabilizer and irradiation synthesis system (Flores-Rojas et al., 2020). Radiolysis process have been proposed for the synthesis of silver nanoparticles (Jannoo, Teerapatsakul, Punyanut, & Pasanphan, 2015; Ramnani, Biswal, & Sabharwal, 2007), gold nanoparticles (Bondaz et al., 2020; Meyre, Tréguer-Delapierre, & Faure, 2008) and copper nanoparticles (Ahmad, Ahmad, & Radiman, 2009; Alyan, Abdel-Samad, Massoud, & Waly, 2019).

It is known that polymer stabilizer is an important component for stabilizing metallic nanoparticles not only during the synthesis process but also prolonging the post-synthesized product. Polymers containing reactive functions for providing strong complexation or coordination and electrostatic interaction with the metallic ions precursor and their nanoparticles have been considered as stabilizers for metallic nanoparticle synthesis. Chitosan and its derivatives (Tangthong et al., 2021a, 2021b), silk fibroin peptide (Wongkrongsak, Tangthong, & Pasanphan, 2016), ascorbic acid (Ismail et al., 2019), polyvinyl alcohol (PVA) (Zhou et al., 2008) and polyvinyl pyrrolidone (PVP) (Misra, Biswal, Gupta, Sainis, & Sabharwal, 2012) have been used as polymer stabilizer for metallic NPs synthesis. PVP is an amorphous, hygroscopic synthetic polymer composed of linear 1-vinyl-2-pyrrolidinone function (Hiremath, Nuguru, & Agrahari, 2019). During the nanoparticle synthesis, PVP could form a protective layer on the surface of various nanoparticles (Hsu & Wu, 2007). N-vinylpyrrolidone (VP) is a hydrophilic monomer of PVP that is commonly used as a stabilizer for polymer-based nanoparticles (Pornpitchanarong, Rojanarata, Opanasopit, Ngawhirunpat, & Patrojanasophon, 2020). PVP helps to resist aggregation by possessing a steric hindrance structure and acting as NPs dispersant when formulated into a polymer matrix. This leads to the ability to formulate metallic NPs with remarkably stable and inert properties (Koczkur, Mourdikoudis, Polavarapu, & Skrabalak, 2015). To the best of our knowledge, a simultaneous synthesis of CuNPs in solid PVP polymer using radiolysis method has not yet been reported.

In this work, we are, therefore, focusing on the synthesis and fabrication of CuNPs in PVP solid matrix using simultaneous gamma-ray irradiation process. The effects of PVP, VP, and Cu precursor concentrations on radiolytic synthesis of CuNPs in PVP composite were studied. Chemical structures were characterized by Fourier Transform Infrared Spectroscopy (FT-IR). CuNPs formation was confirmed by X-rays Diffraction (XRD). The elemental composition of CuNPs in PVP composite materials were observed by Energy Dispersive X-rays Spectrometer (SEM/EDS). Stability of CuNPs-PVP composite materials was investigated within a time interval.

2. Materials and Methods

2.1 Materials

Copper (II) sulfate ($CuSO_4$, MW = 159.6 Da) was purchased from Ajax Finechem Pty Ltd. (Australia). Poly (vinyl pyrrolidone) (PVP) K-30 (MW = 40,000 g/mol) and vinyl pyrrolidone (VP, MW = 111.14 g/mol) were bought from Guangdong Yumay Chemical Co., Ltd. (China).

Suan Sunandha Science and Technology Journal
©2022 Faculty of Science and Technology, Suan Sunandha Rajabhat University

2.2 Instrument and characterizations

Gamma-rays irradiation process was carried out in a ^{60}Co Gammacell 220 irradiator with a dose rate of 1.6 kGy/h. A Red-dyed PMMA dosimeter type Red 4304 was supplied from Harwell Dosimeter Ltd. The samples were irradiated in air under room temperature and pressure. FTIR analyses were carried out by Fourier Transform Infrared Spectroscopy (FT-IR) in Bruker Tensor 27 (USA) with Attenuated Total Reflectance Mode (ATR mode). The FTIR spectra detected 32 scans at a resolution of 2 cm^{-1} in a frequency range of 4000-400 cm^{-1}. The X-ray diffraction (XRD) patterns were taken on a Bruker AXS (Germany) with CuK_{α} radiation as an X-ray source operating at 50 kV and 100 mA. The diffraction data were collected over the angular 2θ range of 10-80° at a scan rate of 5°/min. A standard powder diffraction card of JCPDS, copper file (No. 01-1241 & 03-1005) (Ramesh, Vetrivel, Suresh, & Kaviarasan, 2020) was used for identifying the characteristic diffraction. Morphology and elemental composition of the composite were assessed using scanning electron microscope with Scanning Electron Microscope - Energy Dispersive X-rays Spectrometer (SEM/EDS) in Quanta 450, FEI (Netherlands). The samples were cut into rectangular shape and then placed onto carbon tape on an aluminum holder. Physical appearance and stability were carried out under room temperature by CanoScan LiDE 300 scanner. The recorded data were observed for 0, 7 and 180 days.

2.3 Synthesis of CuNPs in PVP-VP composite materials by gamma-rays irradiation process

$CuSO_4$ solution (6.384 g, 400 mM) was prepared by dissolving in distilled water (100 mL). The $CuSO_4$ solution (400 mM, 0, 250, 500, 750, 1000 µL) were mixed with PVP powder (0, 2, 4, 6, 8 g). VP solution was then added to adjust final concentration $CuSO_4$/PVP/VP mixture for 10 mL to obtain the mixtures with $CuSO_4$ (0, 10, 20, 30 and 40 mM) and PVP (0, 10, 20, 30 and 40% w/w) in VP (50-100% w/w). The mixtures were irradiated by gamma-rays irradiation with an absorbed dose of 25 kGy in air under room temperature to obtain CuNPs in polymerized VP in PVP (CuNPs/PVP-VP_n). Similarly, PVP matrix without $CuSO_4$ was also prepared. PVP powder (1, 2, 3, 4, 5 and 6 g) were mixed with VP solution (9, 8, 7, 6, 5 and 4 g) to obtain the total volume of 10 g of PVP-VP solution with various concentrations of PVP 10, 20, 30, 40, 50 and 60% w/v, respectively. The solution was vigorously stirred for 4 h and then irradiated by gamma-rays at 25 kGy in air under room temperature to obtain polymerized VP in PVP (PVP-VP_n) matrix.

FTIR (ATR, cm^{-1}) for PVP (Fig. 3(a)): 3450 (O-H stretching), 2941 (C-H stretching), 1648 (C=O stretching), 1420, (C-N stretching) 1285 (C-N bending), 840 (pyrrolidone ring), 646, 567 (N-C=O bending). For VP (Fig. 3(b)): 2941 (C-H stretching), 1693 (C=O stretching), 1625 (C=C stretching), 1420, (C-N stretching), 1285 (C-N bending), 840 (pyrrolidone ring), 646, 567 (N-C=O bending). For PVP/VP mixture (Fig. 3(c)): 2941 (C-H stretching), 1693 (C=O stretching), 1625 (C=C stretching), 1423 (C-N stretching), 1285 (C-N bending), 840 (pyrrolidone ring), 646, 567 (N-C=O bending). For irradiated PVP-VP (25 kGy) (Fig. 3(d)): 3450 (O-H stretching), 2941 (C-H stretching), 1648 (C=O stretching), 1423 (C-N stretcing), 1285 (C-N bending), 840 (pyrrolidone ring), 646, 567 (N-C=O bending).

2.4 Gel fraction analysis of PVP-VP_n

The irradiated samples were dried at 60ºC in an air-oven for 48 h and cut into the dimension of 1 × 1 cm^2. Piece of sample was immersed in distilled water (50 mL) at room temperature within a time interval of 0-168 h. The sample was taken out from the solution and then dried at 60ºC in air oven for 48 h. Gel fraction were determined from (W_d/ W_i) × 100, where W_i is an initial weight of dried sample before immersing in water and W_d is a weight of dried water-insoluble gel.

Suan Sunandha Science and Technology Journal
©2022 Faculty of Science and Technology, Suan Sunandha Rajabhat University

2.5 Swelling behavior of PVP-VP_n

The insoluble gel samples were dried at 60ºC in an air-oven for 48 h and cut into the dimension of 1×1 cm^2 and immersed in distilled water (50 mL) at room temperature. The swollen samples were taken out from solution and weight within time interval of 0-168 h. The swollen samples were dried at 60ºC in air oven for 48 h and then weight to obtain a weight of dried water-insoluble gel (W_d). The swelling degree was calculated from $((W_s - W_d)/W_d) \times 100$, where W_d is a weight of dried insoluble gel and W_s is a weight of swollen gel.

3. Results and Discussion

Formation of CuNPs in PVP-VP_n was simultaneously synthesized and fabricated using radiolysis-based mechanism via radiation-induced reduction and radiation-induced polymerization/crosslinking. Under irradiation, the primary reactive species, i.e., electron from ionization (e^-), excited molecule (R^*) and ions ($R^{\bullet+}$) were generated. Dissociation of excited molecules then brought about free radical production, such as macro radical ($R^\bullet$) of polymer and hydroxyl radical ($H^\bullet$). The $H^\bullet$ and $R^\bullet$ undergo initiation, polymerization and crosslinking of VP and PVP system to create PVP-VP_n solid matrix. Meanwhile, the solvate electron play an important role in the reduction of copper ions (Cu^{2+}) to copper atom (Cu^0) for the production of CuNPs. Radiation-induced reaction of Cu^{2+} for CuNPs synthesis are similar to that of AuNPs and AgNPs as in the previous reports (Jannoo et al., 2015; Piroonpan, Katemake, & Pasanphan, 2020).

3.1 Gel formation of PVP-VP_n matrix

The effect of PVP-VP_n concentration on gel fraction is shown in Figure 1. The PVP-VP_n solid matrix was prepared by gamma-rays irradiation with a dose of 25 kGy. With increasing PVP concentration in the VP liquid monomer, it was found that the gel fraction gradually reduced. The gel fraction was reduced from 59.62% to 32.46% and 20% wt%, when the concentration of PVP increased from 0 to 10 and 20 %wt. The gel fraction decreased down to zero when the PVP concentration was higher than 30 %wt. The results indicated that PVP influenced gel formation in the PVP/VP system. Increasing PVP in VP obstructs the polymerization of VP to VP_n and VP_n might be grafted or crosslinked on the PVP polymer chain. By increasing PVP, in other word reducing VP, the amount of reactive vinyl function of VP also reduced and gel fraction tended to decline. Although the PVP-VP_n became solid form, part of the obtained PVP-VP_n matrix was in a water-soluble form.

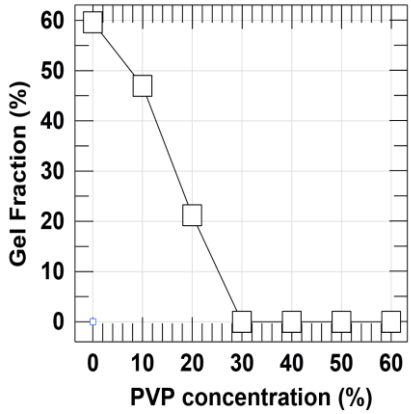

Figure 1. Gel fraction of PVP-VP_n material prepared using different PVP concentrations and irradiated at an absorbed dose of 25 kGy.

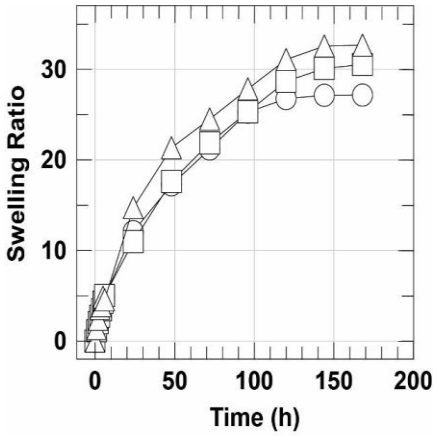

Figure 2. Swelling ratio of PVP-VP_n material prepared using differnt PVP concentration or with PVP: VP ratio of 0:100 (○), 10:90 (□), and 20:80 (△) and irradiated at 25 kGy.

Suan Sunandha Science and Technology Journal
©2022 Faculty of Science and Technology, Suan Sunandha Rajabhat University

3.2 Kinetics swelling of PVP-VP_n matrix

Kinetic swelling of PVP-VP_n was analyzed as shown in Figure 2. Swelling behavior of PVP-VP_n having gel formation was used for observing the swelling ratio. According to the gel fraction result, the PVP-VP_n with the PVP: VP ratio of 0: 100, 10: 90 and 20: 80 were selected. The swelling ratio of all PVP-VP_n samples increased within the time interval of 0-168 h. By prolonging the immersion time, the swelling ratio increased from 0 to around 30%. The swelling ratio of all samples reached a steady state at 168 h (7 days). The greater the gel fraction, the lower swelling ratio was observed because network formation in the PVP-VP_n structure obstructed the expansion of PVP-VP_n chains.

3.3 Functional groups characterization

The functional groups of PVP-VP_n were characterized by FTIR as shown in Figure 3. FIIR spectrum of PVP shows peak at 1648 cm^{-1} assigned to carbonyl group (C=O) on the PVP ring, 3450 and 2941 cm^{-1} assigned to O–H and C–H stretching. Other significant bands of PVP include those caused by pyrrolidone ring at 840 cm^{-1} and N-C=O bending at 567 cm^{-1}. In the case of VP (Figure 3(b)), the peak at 1625 cm^{-1} interpreted as C=C stretching was significantly observed. When PVP was mixed with VP (Figure 3(c)), the C=C stretching peak of VP was additionally found when compared with PVP (Figure 3(a)). After irradiation with the dose of 25 kGy, the characteristic vinyl peak at 1625 cm^{-1} disappeared from the FTIR spectrum of the irradiated PVP-VP_n spectrum (Figure 3(d)). An absence of the C=C absorption band in the irradiated PVP-VP sample suggests that the VP monomer was converted to C-C bond owing to polymerization process upon irradiation.

3.4 Morphology and element analysis

Physical appearance, morphologies and elemental mapping profile of the representative PVP-VP_n and CuNPs-PVP-VP_n composite presented in Figure 4. PVP-VP_n matrix exhibited transparent and light-yellow color in a solid form (Figure 4A(a)). With the CuNPs constructed in the PVP-VP_n matrix, color was changed to be dark brown or copper-like color (Figure 4A(b)). Generally, the color of Cu^{2+} before irradiation was blue due to the characteristic color of $CuSO_4$ (data not shown). Therefore, change of color from blue to copper-like implies the formation of CuNPs due to transformation of Cu^{2+} to Cu^0 atoms upon radiation-induced reduction mechanisms. Figure 4B shows their corresponding SEM images of PVP-VP_n and CuNPs-PVP-VP_n composite samples. The surface morphology of PVP-VP_n was smooth and clear without any particular composite in the matrix. On the other hand, CuNPs-PVP-VP_n samples evidently displayed embedded CuNPs in the PVP-VP_n matrix. The particle size of CuNPs was mostly observed to be ca.100 nm and somewhat agglomerated particles with the size ca. 500 nm was also found in the PVP-VP_n matrix. The morphological information from SEM images implied that CuNPs was successfully synthesized in the PVP-VP_n matrix.

To observe the presence of the Cu element in the PVP-VPn matrix, SEM-EDS mapping images were taken for observing the distribution of Cu. The SEM-EDS spectrum (inset) showed the characteristic K_α-X-rays peak at 8.027 keV. The Cu element in the sample was mapped using such characteristic X-ray. The PVP-VP_n containing CuNPs presented the red dots dealing with Cu elements (Figure 4C(b)). Without the Cu element, the red dot was not found in the mapping image (Fig. 4C(a). The Cu mapping observed in the PVP-VP_n matrix agree with the Cu mapping as observed on the chitosan-graft-PE surface in the previous report (Pasanphan & Chirachanchai, 2008; Pasanphan, Haema, Tangthong, & Piroonpan, 2014)

Suan Sunandha Science and Technology Journal
©2022 Faculty of Science and Technology, Suan Sunandha Rajabhat University

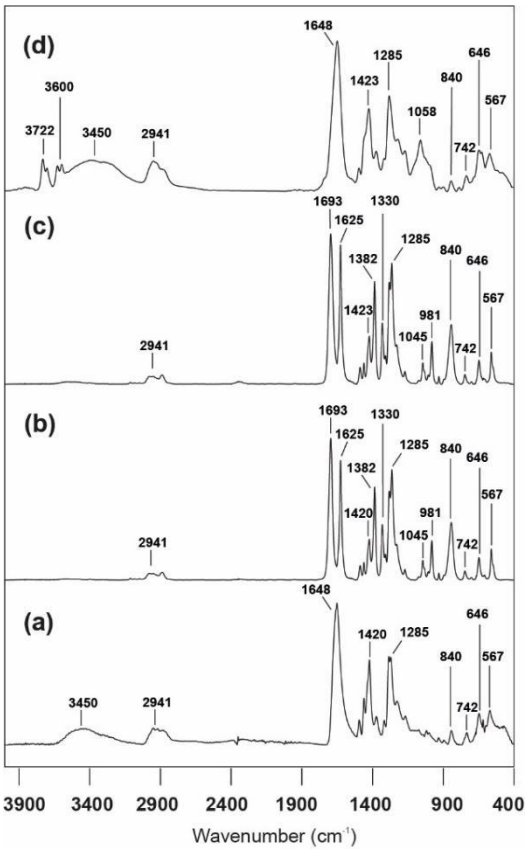

Figure 3. FT-IR spectra of (a) PVP, (b) VP, (c) PVP/VP mixture (ratio 40:60) and (d) irradiated PVP-VP_n (25 kGy).

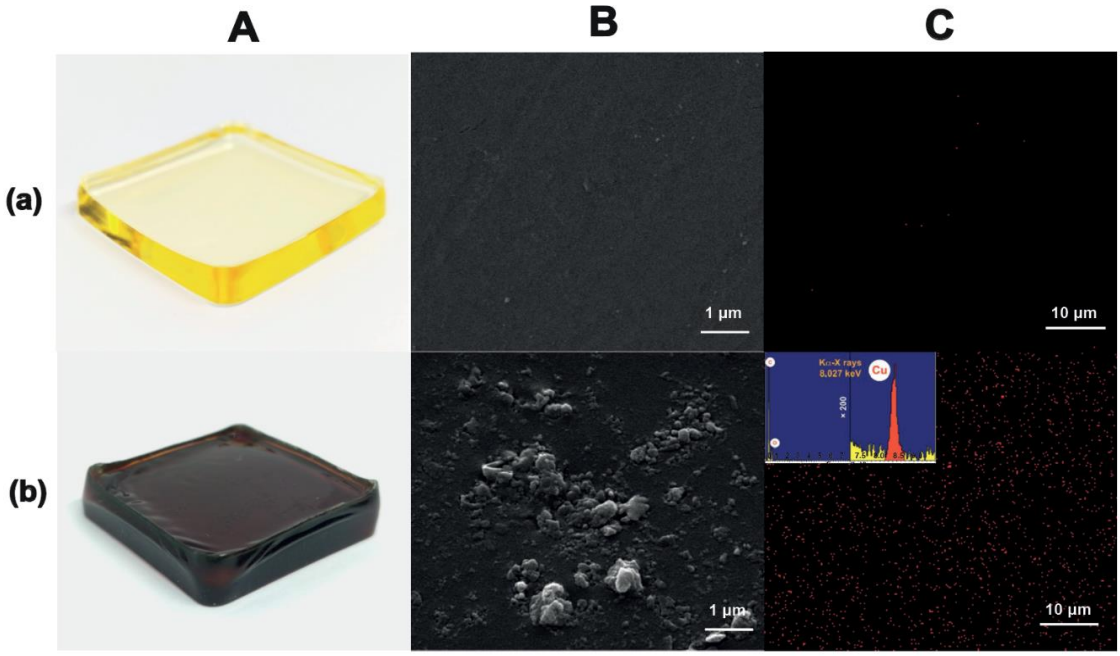

Figure 4. (A) Physical appearance, (B) SEM images, (C) SEM-EDS mapping and EDS spectrum (inset) of (a) PVP-VP and (b) CuNPs-PVP-VP_n composite material.

Suan Sunandha Science and Technology Journal
©2022 Faculty of Science and Technology, Suan Sunandha Rajabhat University

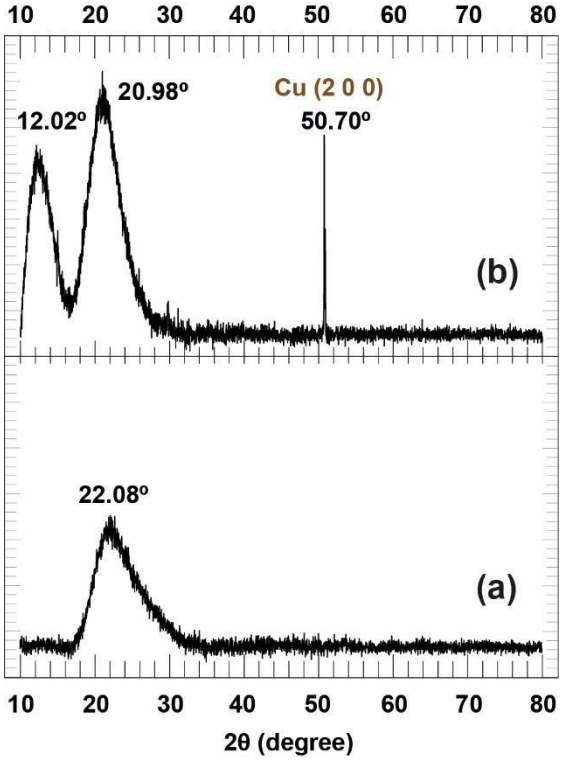

Figure 5. XRD patterns of (a) PVP-VP and (b) PVP-VP-Cu composite material.

3.5 Packing structure and crystal analysis

The XRD patterns of the PVP-VP_n and CuNPs-PVP-VP_n composite materials are shown in Figure 5. The broad diffraction peak at 22.08° (2θ) was observed for the PVP-VPn sample (Figure 5A). The diffraction peaks of PVP-VP_n were in agreement with pure PVP as in the previous literature (Vijaya, Selvasekarapandian, Nithya, & Sanjeeviraja, 2015). The diffraction peak was also observed between ~15°-30° which could be associated with the semi-crystallinity of pure PVP. For CuNPs-PVP-VP_n, the XRD pattern exhibited 2 board diffraction peaks at 12.02° (2θ) and 20.98° (2θ). These two peaks were interpreted as the crystalline of the PVP-VP_n polymeric matrix. The additional diffraction peak at 12.02°(2θ) might be due the new crystalline structure formed because of the influence of metal ions and CuNPs complex with the polymer chain. In addition, the main diffraction peak at 22.08° (2θ) of PVP-VP_n was also shifted to 20.98° (2θ). These changes indicate that the addition of CuNPs to the PVP-VP_n matrix reduced the crystalline nature of PVP-VP_n. This is due to the complexation between the host polymer PVP-VP_n and the CuNPs. It has been reported that when a polymer is complexed with a metal, salt or acid, the crystallinity of the polymer host could be disrupted by the addition of impurities (Kumar, Kim, Nahm, & Elizabeth, 2007).

In addition, the significant and sharp diffraction peak was observed at 50.70° (2θ) (Figure 5B). This new diffraction peak corresponds to (2 0 0) planes of CuNPs (Pham et al., 2012). The diffraction peak of CuNPs observed in PVP-VP_n sample also agreed with that of CuNPs as reported in the previous literature (Phul, Kaur, Farooq, & Ahmad, 2018). The XRD pattern confirmed the face centered cubic lattice of copper (Biçer & Şişman, 2010). The diffraction peak was in good agreement with the standard pattern for pure face centered cubic phase of CuNPs (JCPDS No. 01-1241 & 03-1005). No impurity peaks of CuO or Cu_2O were observed. The XRD result strongly supports the successful synthesis of CuNPs in the PVP-VP_n matrix.

3.6 Physical appearance and stability of CuNPs-PVP-VP_n composite materials

Figure 6 depicts physical appearance and stability of CuNPs-PVP-VP_n samples prepared from different conditions under air atmosphere at ambient temperature and pressure. The PVP-VP_n polymer matrix exhibited transparency matrix. For PVP-VP_n containing CuNPs, the samples changed from transparent appearance to light brown and dark brown colors depending on the concentration of $CuSO_4$ precursor. With higher $CuSO_4$ concentration from 0 to 40 mM, brown color was greater when the long chain PVP polymer was used. The long chain PVP could efficiently stabilize Cu^{2+} and exhibited as a protective polymer that not only stabilizing Cu^{2+} at the initial step but also stabilizing CuNPs after already prepared. It was also found that CuNPs in the PVP-VP_n matrix were very stable for more than 180 days and were greater when the long chain PVP polymer was used. The long chain PVP could efficiently stabilize Cu^{2+} and exhibited as a protective polymer that not only stabilizing Cu^{2+} at the initial step but also stabilizing CuNPs after already prepared. It was also found that CuNPs in PVP-VP_n matrix were very stable more than 180 days.

Suan Sunandha Science and Technology Journal
©2022 Faculty of Science and Technology, Suan Sunandha Rajabhat University

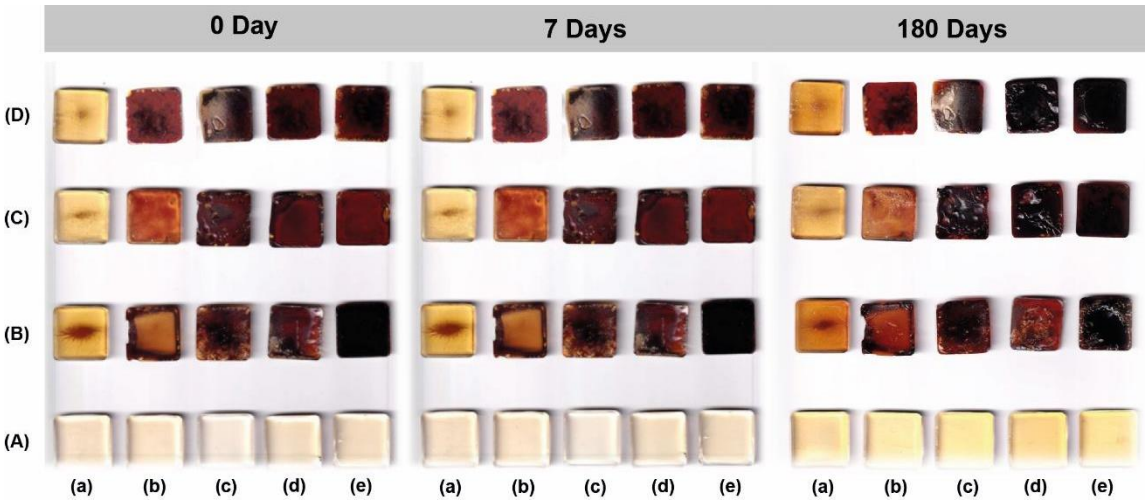

Figure 6. Physical appearances of CuNPs-PVP-VP_n composite material with $CuSO_4$ concentrations of (A) 0, (B) 10, (C) 20 and (D) 40 mM and PVP concentrations of (a) 0, (b) 10, (c) 20, (d) 30 and (e) 40% w/w in VP solution.

4. Conclusions

CuNPs-PVP-VP_n nanocomposite materials were successfully prepared using a simultaneous irradiation process based on radiation-induced reduction and polymerization/crosslinking mechanism. Gel fraction of PVP-VP_n polymer matrix was found when the PVP concentration of 0-20 %wt was used in VP monomer. Gel fraction of PVP-VP_n reduced with increasing PVP concentration. In the combination of PVP-VP_n and Cu ions precursor, CuNPs could successfully synthesize and stabilize in the PVP-VP_n material using irradiation technique with the dose of 25 kGy. CuNPs with the size of ca. 100 nm and some agglomerated CuNPs with the size of ca. 500 nm were embedded inside the PVP-VP_n polymer. The XRD diffraction peak indicated (2 0 0) plane of face centered cubic lattice of CuNPs confirmed successful synthesis of CuNPs without impurity. The CuNPs in PVP-VP_n composite material exhibited outstanding stability up to >180 days. Our established model process for the synthesis of CuNPs in solid polymer would be a practical process for further production of CuNPs for various industrial applications.

5. Acknowledgements

The authors (T.K. and W.P) appreciated Research and Researcher for Industries (RRI) (RRIMSD62_M1051), the National Research Council of Thailand (NRCT) (Thailand) for financial support of this research as a master degree project. The authors also acknowledge Coordinate Research Project (CRP) and Technical Cooperation Programme (THA1014), International Atomic Energy Agency (IAEA), United Nation (UN), Austria (Vienna) for supporting coordinate research and technical cooperation performed at the Center of Radiation Processing for Polymer Modification and Nanotechnology (CRPN), Faculty of Science, Kasetsart University (Thailand).

6. References

Ahmad, S. I. B., Ahmad, M. S. B. H., & Radiman, S. B. (2009). A study on gamma irradiation synthesis of copper nanoparticles. *AIP Conference Proceedings*, *1136*(1), 186-190. doi:10.1063/1.3160127

Alyan, A., Abdel-Samad, S., Massoud, A., & Waly, S. A. (2019). Characterization and thermal conductivity investigation of copper-polyaniline nano composite synthesized by gamma radiolysis method. *Heat and Mass Transfer*, *55*, 2409-2417. doi:10.1007/s00231-019-02588-z

Athanassiou, E. K., Grass, R. N., & Stark, W. J. (2006). Large-scale production of carbon-coated copper nanoparticles for sensor applications. *Nanotechnology*, *17*(6), 1668-1673. doi:10.1088/0957-4484/17/6/022

Suan Sunandha Science and Technology Journal
©2022 Faculty of Science and Technology, Suan Sunandha Rajabhat University

Biçer, M., & Şişman, İ. (2010). Controlled synthesis of copper nano/microstructures using ascorbic acid in aqueous CTAB solution. *Powder Technology*, *198*(2), 279-284. doi:10.1016/j.powtec.2009.11.022

Bondaz, L., Fontaine, P., Muller, F., Pantoustier, N., Perrin, P., Morfin, I., ... Cousin, F. (2020). Controlled synthesis of gold nanoparticles in copolymers nanomolds by X-ray radiolysis. *Langmuir*, *36*(22), 6132-6144. doi:10.1021/acs.langmuir.0c00554

Chandra, S., Kumar, A., & Tomar, P. K. (2014). Synthesis and characterization of copper nanoparticles by reducing agent. *Journal of Saudi Chemical Society*, *18*(2), 149-153. doi:10.1016/j.jscs.2011.06.009

Cheng, C., Li, J., Shi, T., Yu, X., Fan, J., Liao, G., ... & Tang, Z. (2017). A novel method of synthesizing antioxidative copper nanoparticles for high performance conductive ink. *Journal of Materials Science: Materials in Electronics*, *28*(18), 13556-13564. doi:10.1007/s10854-017-7195-9

Flores-Rojas, G. G., López-Saucedo, F., & Bucio, E. (2020). Gamma-irradiation applied in the synthesis of metallic and organic nanoparticles: A short review. *Radiation Physics and Chemistry*, *169*, 107962. doi:10.1016/j.radphyschem.2018.08.011

Giuffrida, S., Costanzo, L. L., Ventimiglia, G., & Bongiorno, C. (2008). Photochemical synthesis of copper nanoparticles incorporated in poly (vinyl pyrrolidone). *Journal of Nanoparticle Research*, *10*(7), 1183-1192. doi:10.1007/s11051-007-9343-2

Hiremath, P., Nuguru, K., & Agrahari, V. (2019). Material attributes and their impact on wet granulation process performance. In A. S. Narang, & S. Badawy (Eds.), *Handbook of pharmaceutical wet granulation* (pp. 263-315). Academic Press.

Hsu, S. L. C., & Wu, R. T. (2007). Synthesis of contamination-free silver nanoparticle suspensions for micro-interconnects. *Materials Letters*, *61*(17), 3719-3722. doi:10.1016/j.matlet.2006.12.040

Ismail, N. A., Shameli, K., Wong, M. M. T., Teow, S. Y., Chew, J., & Sukri, S. N. A. M. (2019). Antibacterial and cytotoxic effect of honey mediated copper nanoparticles synthesized using ultrasonic assistance. *Materials Science and Engineering*: C, *104*, 109899. doi:10.1016/j.msec.2019.109899

Jannoo, K., Teerapatsakul, C., Punyanut, A., & Pasanphan, W. (2015). Electron beam assisted synthesis of silver nanoparticle in chitosan stabilizer: Preparation, stability and inhibition of building fungi studies. *Radiation Physics and Chemistry*, *112*, 177-188. doi:10.1016/j.radphyschem.2015.03.035

Joshi, S. S., Patil, S. F., Iyer, V., & Mahumuni, S. (1998). Radiation induced synthesis and characterization of copper nanoparticles. *Nanostructured Materials*, *10*(7), 1135-1144. doi:10.1016/S0965-9773(98)00153-6

Koczkur, K. M., Mourdikoudis, S., Polavarapu, L., & Skrabalak, S. E. (2015). Polyvinylpyrrolidone (PVP) in nanoparticle synthesis. *Dalton Transactions*, *44*(41), 17883-17905. doi:10.1039/C5DT02964C

Kumar, G. G., Kim, P., Nahm, K. S., & Elizabeth, R. N. (2007). Structural characterization of PVdF-HFP/PEG/Al_2O_3 proton conducting membranes for fuel cells. *Journal of Membrane Science*, *303*(1-2), 126-131. doi:10.1016/j.memsci.2007.06.069

Meyre, M. E., Tréguer-Delapierre, M., & Faure, C. (2008). Radiation-induced synthesis of gold nanoparticles within lamellar phases. Formation of aligned colloidal gold by radiolysis. *Langmuir*, *24*(9), 4421-4425. doi:10.1021/la703650d

Misra, N., Biswal, J., Gupta, A., Sainis, J. K., & Sabharwal, S. (2012). Gamma radiation induced synthesis of gold nanoparticles in aqueous polyvinyl pyrrolidone solution and its application for hydrogen peroxide estimation. *Radiation Physics and Chemistry*, *81*(2), 195-200. doi:10.1016/j.radphyschem.2011.10.014

Moazzenchi, B., & Montazer, M. (2020). Click electroless plating and sonoplating of polyester with copper nanoparticles producing conductive fabric. *Fibers and Polymers*, *21*(3), 522-531. doi:10.1007/s12221-020-9664-7

Pasanphan, W., & Chirachanchai, S. (2008). Polyethylene film surface functionalized with chitosan via γ-ray irradiation in

aqueous system: An approach to induce copper (II) ion adsorptivity on PE. *Reactive and Functional Polymers*, *68*(8), 1231-1238. doi: 10.1016/j.reactfunctpolym.2008.05.006

Pasanphan, W., Haema, K., Tangthong, T., & Piroonpan, T. (2014). Modification of chitosan onto PE by irradiation in salt solutions and possible use as Cu^{2+} complex film for pest snail control. *Journal of Applied Polymer Science*, *131*(23), 41204. doi:10.1002/app.41204

Pham, L. Q., Sohn, J. H., Kim, C. W., Park, J. H., Kang, H. S., Lee, B. C., & Kang, Y. S. (2012). Copper nanoparticles incorporated with conducting polymer: Effects of copper concentration and surfactants on the stability and conductivity. *Journal of Colloid and Interface Science*, *365*(1), 103-109. doi:10.1016/j.jcis.2011.09.041

Phul, R., Kaur, C., Farooq, U., & Ahmad, T. (2018). Ascorbic acid assisted synthesis, characterization and catalytic application of copper nanoparticles. *Material Science & Engineering International Journal*, *2*(4), 90-94. doi:10.15406/mseij.2018.02.00040

Piroonpan, T., Katemake, P., & Pasanphan, W. (2020). Comparative study of different chitosan solutions to assist the green synthesis of gold nanoparticles under irradiation. *Radiation Physics and Chemistry*, *169*, 108250. doi:10.1016/j.radphyschem.2019.03.054

Pornpitchanarong, C., Rojanarata, T., Opanasopit, P., Ngawhirunpat, T., & Patrojanasophon, P. (2020). Synthesis of novel N-vinylpyrrolidone/acrylic acid nanoparticles as drug delivery carriers of cisplatin to cancer cells. *Colloids and Surfaces B: Biointerfaces*, *185*, 110566. doi:10.1016/j.colsurfb.2019.110566

Ramesh, S., Vetrivel, S., Suresh, P., & Kaviarasan, V. (2020). Characterization techniques for nano particles: A practical top down approach to synthesize copper nano particles from copper chips and determination of its effect on planes. *Materials Today: Proceedings*, *33*, 2626-2630. doi:10.1016/j.matpr.2020.01.157

Ramnani, S. P., Biswal, J., & Sabharwal, S. (2007). Synthesis of silver nanoparticles supported on silica aerogel using gamma radiolysis. *Radiation Physics and Chemistry*, *76*(8-9), 1290-1294. doi:10.1016/j.radphyschem.2007.02.074

Tangthong, T., Piroonpan, T., Thipe, V. C., Khoobchandani, M., Katti, K., Katti, K. V., & Pasanphan, W. (2021a). Bombesin peptide conjugated water-soluble chitosan gallate—A new nanopharmaceutical architecture for the rapid one-pot synthesis of prostate tumor targeted gold nanoparticles. *International Journal of Nanomedicine*, *16*, 6957-6981. doi:10.2147/IJN.S327045

Tangthong, T., Piroonpan, T., Thipe, V. C., Khoobchandani, M., Katti, K., Katti, K. V., & Pasanphan, W. (2021b). Water-soluble chitosan conjugated DOTA-Bombesin peptide capped gold nanoparticles as a targeted therapeutic agent for prostate cancer. *Nanotechnology, Science and Applications*, *14*, 69-89. doi:10.2147/NSA.S301942

Tomotoshi, D., & Kawasaki, H. (2020). Surface and interface designs in copper-based conductive inks for printed/flexible electronics. *Nanomaterials*, *10*(9), 1689. doi:10.3390/nano10091689

Vijaya, N., Selvasekarapandian, S., Nithya, H., & Sanjeeviraja, C. (2015). Proton conducting polymer electrolyte based on poly (N-vinyl pyrrolidone) doped with ammonium iodide. *International Journal of Electroactive Materials*, *3*, 20-27.

Wahyudi, S., Soepriyanto, S., & Mubarok, M. Z., & Sutarno. (2018). Synthesis and applications of copper nanopowder–A review. *IOPConference Series: Materials Science and Engineering*, *395*(1), 012014. doi:10.1088/1757-899X/395/1/012014

Wongkrongsak, S., Tangthong, T., & Pasanphan, W. (2016). Electron beam induced water-soluble silk fibroin nanoparticles as a natural antioxidant and reducing agent for a green synthesis of gold nanocolloid. *Radiation Physics and Chemistry*, *118*, 27-34. doi:10.1016/j.radphyschem.2015.03.020

Wongpisutpaisan, N., Charoonsuk, P., Vittayakorn, N., & Pecharapa, W. (2011). Sonochemical

Suan Sunandha Science and Technology Journal
©2022 Faculty of Science and Technology, Suan Sunandha Rajabhat University

synthesis and characterization of copper oxide nanoparticles. *Energy Procedia*, *9*, 404-409. doi:10.1016/j.egypro.2011.09.044

Zhou, F., Zhou, R., Hao, X., Wu, X., Rao, W., Chen, Y., & Gao, D. (2008). Influences of surfactant (PVA) concentration and pH on the preparation of copper nanoparticles by electron beam irradiation. *Radiation Physics and Chemistry*, *77*(2), 169-173. doi:10.1016/j.radphyschem.2007.05.007

Zinn, A. A., Stoltenberg, R. M., Fried, A. T., Chang, J., Elhawary, A., Beddow, J., & Chiu, F. (2012). Nanocopper based solder-free electronic assembly material. *Nanotech*, *2*, 71-74.

Available online at http://www.ssstj.sci.ssru.ac.th

Suan Sunandha Science and Technology Journal
©2022 Faculty of Science and Technology, Suan Sunandha Rajabhat University

Effect of Extraction Solvent on Capsaicin Content of Chinda Peppers

Sutiam Kruawan*, Pikuntong Hanchaiyaphum, Sarawut Sodawichit, Phiyada Janthakhat, Supawita Konglamjeak, Natthida Khiewbanyang, Thitipong Wutisart, Bpantamars Phadungchob

Faculty of Education, Dhonburi Rajabhat University, Thonburi, Bangkok 10600, Thailand

*Corresponding author e-mail: sutiam.k@dru.ac.th

Received: *22 August 2021* / **Revised**: *23 September 2021* / **Accepted**: *8 February 2022*

Abstract

Chinda pepper (*Capsicum annuum* L.) is classified as a large chili pepper that is an important economic crop of Thailand. The substance in the chili pepper responsible for its spicy taste is capsaicin. Presently, capsaicin in Chinda peppers has been extracted for use in food and medical products. This research compared the capsaicin content from dried Chinda peppers in four different solvents: H_2O, acetone, ethanol (95% v/v), and a binary solvent of acetone and water at a ratio of 1:1 v/v. For all treatments, the ratio of chili peppers to the solvent was 20 g:240 ml. After analyzing the amount of capsaicin content by a NanoDrop spectrophotometer, it was found that the capsaicin content from dried Chinda pepper by the H_2O:acetone (1:1 v/v), acetone, H_2O and ethanol (95% v/v) were 0.48 ppm, 0.26 ppm, 0.22 ppm, and 0.18 ppm, respectively. These results indicated that the extraction of capsaicin with a binary solvent of H_2O:acetone at a ratio of 1:1 v/v had the highest extraction concentration. This can be explained theoretically that the presence of H_2O in acetone impacted the hydrophobic properties of the solvent and the interaction between capsaicin compound and the solvent.

Keywords: Capsaicin, Extraction, Chinda pepper

1. Introduction

Peppers are one of the most popular ingredients used to add a spicy flavor in several food preparations. They play an important role in the food industry in Thailand. Thailand is among the top three countries-India, China, and Thailand-which has grown the most chili peppers worldwide with 176,873 metric tons being grown and harvested in Thailand (Food and Agriculture Organization of the United Nations [FAO], 2021). Chili peppers are not only mainly utilized for a spicy flavor in food, extractable chemical compounds such as oleoresins were also used in cosmetic and dye industries (Advanced Biotech [ABT], 2021; Imbarex, 2021). Generally, their spicy flavor is due to a main group of organic compounds, capsaicinoids. Capsaicinoids are soluble in moderate polar organic solvents; e.g. methanol, ethanol, acetonitrile and binary solvent among others (Kurian & Starks, 2002). They are also soluble in water at 25°C (28.93 mg/l) and are practically insoluble in cold water (National Library of Medicine [NIH], 2021). The major capsaicinoid compound present in most varieties of the chili peppers is capsaicin (trans-8-methyl-N-vanillyl-6-nonenamide) (Figure 1). In addition, other capsaicinoid compounds were also found in relatively small amounts; such as nordihydrocapsaicin, homocapsaicin, normorcapsacin, etc. (Kobata et al., 1998) Even though capsaicin can cause irritation to skin and respiratory system, it has been extensively studied both experimentally and clinically for its ability to stimulate sensory nerves and to treat bladder inflammation (Kaale, Schepdael, Roets, & Hoogmartens, 2002). Determination of capsaicin content in chili peppers has received an increasing

Suan Sunandha Science and Technology Journal
©2022 Faculty of Science and Technology, Suan Sunandha Rajabhat University

interest for many reasons. Extraction methods of the capsaicin from peppers have been conducted using various extraction techniques including liquid-liquid extraction (LLE) (Tapia, Garcia, Escamilla, Calva, & Rocha, 1993), enzymatic extraction (Santamaria et al., 2000), solid-phase microextraction (SPME) (Spicer & Almirall, 2005) and ultrasonic assisted extraction (Karnka, Rayanakorn, Watanesk, & Vaneesorn, 2002). In addition, the efficiency of capsaicinoids extraction from chili peppers is influenced by the parts of chili peppers used, tissue preparation, contact time, sample particle size, storage time, as well as the presence of interfering substances. Moreover, extraction solvents play an important role in extraction efficiency. In an extraction, one has to priorly consider the chemical nature in different varieties of chili peppers and the type of extraction solvent. In this research, the extraction of capsaicin from Chinda peppers was investigated using solid-liquid extraction methods with different solvents: water, acetone, ethanol, and their combination.

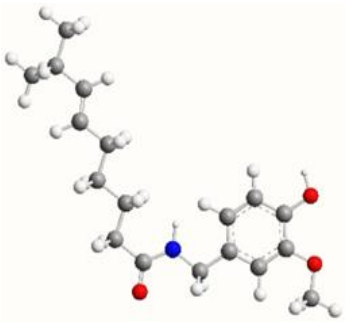

Figure 1. Schematic representation of the structure of Capsaicin. grey: C; white: H; red: O; blue: N.

Moreover, a quantitative analysis of capsaicin content from chili pepper sample can also be done using various techniques; for example, solid phase extraction (SPE) (Attuquayefio & Buckle, 1987), gas chromatography-mass spectrometry (GC-MS) (Thomas, Schreiber, & Weisskopf, 1998), high-performance chromatography (HPLC) (Barbero, Palma, & Barroso, 2006). However, these equipment can be expensive, difficult to use, and uncommon in a routine analysis. For convenience and reliability, a technique associated with UV absorption measured with common wavelength (λ_{max} = 280 nm) has been presently accepted (Juangsamoot, Ruangviriyachai, Techawongstien, & Chanthai, 2012). In this research, a NanoDrop Spectrophotometer was used in the quantitative analysis of capsaicin.

2. Materials and Methods

2.1 Chemicals

All reagents used were at least analytical reagent (AR) grade. Ethanol was supplied by Gammaco (Thailand). Acetone was supplied by Lab Scan (Thailand). The highest purity of standard capsaicin was obtained from Ennagram (France). Aqueous solutions were prepared with deionized water throughout the experiments.

2.2 Instrument

The standard addition method was carried out to determine the amount of capsaicin content. The standard dilute concentrations of 0.02, 0.04, 0.06, 0.08 and 0.10 mg/ml were prepared for the calibration curve. The absorbance of capsaicin was carried out by NanoDrop Spectrophotometer at λ_{max} = 280 nm.

2.3 Plant materials

Chinda peppers (*Capsicum annuum* L.) used in this study were obtained from a fresh market in Thonburi, Bangkok, Thailand. The whole fresh chili pepper was dried in a hot-air oven (at 100°C for 3 hours 30 minutes until constant weight was achieved). The dried samples were ground and stored in a desiccator until usage.

2.4 Solvent extraction

The ground dried samples were weighed for 20 grams and macerated in 240 ml of 4 different solvents (H_2O, 95% v/v ethanol, and 1:1 v/v H_2O:acetone) at room temperature for 24 hours extraction time. The extracts were filtered through a Whatman No. 42 filter paper. The solvent in the extracts was evaporated to dryness using a water bath (100°C). The residue from the evaporation was weighed for 10 mg and dissolved in suitable methanol solvent to make a final volume of 100 ml,

Suan Sunandha Science and Technology Journal
©2022 Faculty of Science and Technology, Suan Sunandha Rajabhat University

which produced a sample solution of 1.0 mg/ml concentration. The solutions were further quantitatively analyzed for capsaicin content by NanoDrop Spectrophotometer. The experiments were conducted in 3 duplicates for each type of solvents.

2.5 Preparation and analysis of capsaicin by NanoDrop Spectrophotometer

The capsaicin standard solution of 1.0 mg/ml was diluted to 0.02, 0.04, 0.06, 0.08 mg/ml. These solutions were used to graph the standard curve by measuring the absorbance at λ_{max} = 280 nm by NanoDrop Spectrophotometer. This standard curve was used to determine the amount of capsaicin in the unknown samples of each treatment.

3. Results and Discussion

The standard curve for the capsaicin content generated using 0.02, 0.04, 0.06, 0.08 and 0.10 mg/ml capsaicin standard solution versus optical density at 280 nm was recorded. The linear standard curve is shown in Figure 2, R^2 = 1.00.

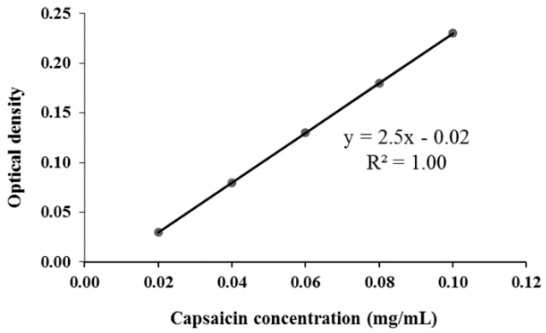

Figure 2. The plot of optical density vs capsaicin concentration shows a positive linear relationship.

To determine capsaicin content in four different extraction solvents, optical activity readings were converted into their respective concentrations using the standard curve in Figure 2, R^2 = 1.00. The average capsaicin content was calculated in ppm as shown in Table 1. The capsaicin content indicates the extraction efficiency. The results revealed that the capsaicin content was related to the type of the solvents. This agrees well with the rationality by which the polarity of solvent affects capsaicin extraction efficiencies (Rostagno, Palma, & Barroso, 2003). Moreover, it inferred that the binary mixture (H_2O:acetone) showed a higher capsaicin concentration when compared to the single solvents; acetone, H_2O, and ethanol. Among the single solvents, acetone has the highest capsaicin content, followed by H_2O and ethanol, respectively.

Nevertheless, different extraction efficiencies have been reported when the same solvent was used on dried versus wet chili pepper samples. Ethanol and Acetonitrile were better solvents for capsaicin extraction from fresh chili pepper samples, while acetone was a better solvent for capsaicin extraction from dried chili pepper samples (Chinn, Sharma-Shivappa, & Cotter, 2011). In other words, acetone alone was expected to have the highest extraction efficiency among the single solvents, which the results of this work agreed upon. On the other hand, the highest extraction efficiency of binary solvent observed in this work infers that the presence of H_2O during the extraction may have an impact on the hydrophobic properties of the solvents and the interaction with capsaicin compound (Barbero, Liazid, Palma, & Barroso, 2008; Rostagno et al., 2003). Whether to use single or binary solvent, it may depend on what is available or convenient to the user. However, regardless of choosing to use a single or binary solvent, the extraction efficiency of the specific solvent chosen still has to be considered. As shown by the results of this work, the yield of capsaicin content extractable from Chinda peppers was significantly affected by the type of the solvent as shown in Table 1, which agreed well with literature (Chinn et al., 2011). Although the parts of peppers used in the extraction (e.g. whole peppers, seeds, shells) might have an effect on the extraction efficiency (Attuquayefio & Buckle, 1987), the whole Chinda peppers were used in this work to mimic a practical production in a large scale processing and industries. To aid with consideration for processing and industrial uses, the comparison of advantages and disadvantages of the single and binary solvents used in this work was summarized in Table 2.

Suan Sunandha Science and Technology Journal
©2022 Faculty of Science and Technology, Suan Sunandha Rajabhat University

Table 1. The capsaicin content extracted from dried Chinda pepper by different extraction solvents.

Extraction solvents	Capsaicin content (ppm)
H_2O	0.22
Ethanol (95% v/v)	0.18
Acetone	0.26
H_2O:Acetone (1:1 v/v)	0.48

Table 2. The advantages and disadvantages of different extraction solvents.

Extraction solvents	Advantages	Disadvantages
H_2O	- Safe for consumption - Low cost	- Poor extraction efficiency
Ethanol (95% v/v)	- Safe for consumption - Easily obtained	- Slow filtration rate
Acetone	- High extraction efficiency for single solvent	- Possible health effects due to acetone contamination
H_2O:Acetone (1:1 v/v)	- Highest extraction efficiency	- Possible health effects due to acetone contamination

4. Conclusions

The solid-liquid extraction efficiency have been carried out to investigate the capsaicin content extractable from whole Chinda pepper parts using 4 different solvents: H_2O, acetone, ethanol (95% v/v), and H_2O:acetone (1:1 v/v). The results from NanoDrop Spectrophotometer showed that the capsaicin content decreases in the following order: H_2O:acetone (1:1 v/v) > Acetone > H_2O > 95%v/v ethanol. The different extraction concentration generally was related to the different polarity properties between solvents and capsaicin compounds. It was observed that binary mixture H_2O:acetone (1:1 v/v) obtained the highest capsaicin content. The presence of H_2O might have an impact on the hydrophobic properties of solvent and the interaction with capsaicin compounds. Furthermore, acetone alone had the highest concentration of capsaicin followed by H_2O and ethanol for dried Chinda peppers which agreed with reports elsewhere. Finally, to obtain a high capsaicin content from Chinda peppers, the choice of extraction solvent is of the matter.

5. Acknowledgement

We would like to thank Food Innovation Research Laboratory and Faculty of Science and Technology, Dhonburi Rajabhat University for lending us laboratory equipment and space, also the students who tirelessly brainstormed and worked days and nights to complete the design and the data collection of this work.

6. References

Advanced Biotech [ABT]. (2021). *Oleoresins*. Retrieved from https://www.adv-bio.com/oleoresins/

Attuquayefio, V. K., & Buckle, K. A. (1987). Rapid sample preparation method for HPLC analysis of capsaicinoids in capsicum fruits and oleoresins. *Journal of Agricultural and Food Chemistry*, *35*(5), 777-779. doi:10.1021/jf00077a032

Barbero, G. F., Liazid, A., Palma, M., & Barroso, C. G. (2008). Ultrasound-assisted extraction of capsaicinoids from peppers. *Talanta*, *75*(5), 1332-1337. doi:10.1016/j.talanta.2008.01.046

Barbero, G. F., Palma, M., & Barroso, C. G. (2006). Determination of capsaicinoids in peppers by microwave-assisted extraction-high performance liquid chromatography with fluorescence detection. *Analytica Chimica Acta*, *578*(2), 227-233. doi:10.1016/j.aca.2006.06.074

Chinn, M. S., Sharma-Shivappa, R. R., & Cotter, J. L. (2011). Solvent extraction and quantification of

Suan Sunandha Science and Technology Journal
©2022 Faculty of Science and Technology, Suan Sunandha Rajabhat University

capsaicinoids from *Capsicum chinense*. *Food and Bioproducts Processing*, *89*(4), 340-345. doi:10.1016/j.fbp.2010.08.003

Food and Agriculture Organization of the United Nations [FAO]. (2021). Retrieved from www.fao.org

Imbarex. (2021). *Paprika oleoresin: Orange natural dye*. Retrieved from https://www.imbarex.com/paprika-oleoresin-orange-natural-dye/

Juangsamoot, J., Ruangviriyachai, C., Techawongstien, S., & Chanthai, S., (2012). Determination of capsaicin and dihydrocapsaicin in some hot chilli varieties by RP-HPLC-PDA after magnetic stirring extraction and clean up with C_{18} cartridge. *International Food Research Journal*, *19*(3), 1217-1226. doi:10.1155/2012/380574

Kaale, E., Schepdael, A. V., Roets, E., & Hoogmartens, J. (2002). Determination of capsaicinoids in topical cream by liquid-liquid extraction and liquid chromatography. *Journal of Pharmaceutical and Biomedical Analysis*, *30*(4), 1331-1337. doi:10.1016/s0731-7085(02)00476-4

Karnka, R., Rayanakorn, M., Watanesk, S., & Vaneesorn, Y. (2002). Optimization of high-performance liquid chromatographic parameters for the determination of capsaicinoid compounds using the simplex method. *Analytical Sciences*, *18*(6), 661-665. doi:10.2116/analsci.18.661

Kobata, K., Kawamura, M., Toyoshima, M., Tamura, Y., Ogawa, S., & Watanabe, T. (1998). Lipase-catalyzed synthesis of capsaicin analogs by amidation of vanillylamine with fatty acid derivatives. *Biotechnology Letters*, *20*, 451-454. doi:10.1023/A:1005567923159

Kurian, A. L., & Starks, A. N. (2002). HPLC analysis of capsaicinoids extracted from whole orange habanero chili peppers. *Journal of Food Science*, *67*(3), 956-962. doi:10.1111/j.1365-2621.2002.tb09435.x

National Library of Medicine. (2021). Retrieved from https://pubchem.ncbi.nlm.nih.gov/compound/Capsaicin

Rostagno, M. A., Palma, M., & Barroso, C. G. (2003). Ultrasound-assisted extraction of soy isoflavones. *Journal of Chromatography A*, *1012*(2), 119-128. doi:10.1016/s0021-9673(03)01184-1

Santamaria, R. I., Reyes-Duarte, M. D., Barzana, E., Fernando, D., Gama, F. M., Mota, M., & Lopez-Munguia, A. (2000). Selective enzyme-mediated extraction of capsaicinoids and carotenoids from chili guajillo puya (*Capsicum annuum* L.) using ethanol as solvent. *Journal of Agricultural and Food Chemistry*, *48*(7), 3063-3067. doi:10.1021/jf991242p

Spicer, O., & Almirall, J. R. (2005). Extraction of capsaicin in aerosol defense sprays from fabrics. *Talanta*, *67*(2), 377-382. doi:10.1016/j.talanta.2005.05.031

Tapia, J. C., Garcia, R., Escamilla, E. M., Calva, G., & Rocha, J. A. (1993). Capsaicin recovery from a cell culture broth. *Industrial & Engineering Chemistry Research*, *32*(10), 2242-2246. doi:10.1021/ie00022a007

Thomas, B. V., Schreiber, A. A., & Weisskopf, C. P. (1998). Simple method for quantitation of capsaicinoids in peppers using capillary gas chromatography. *Journal of Agricultural and Food Chemistry*, *46*(7), 2655-2663. doi:10.1021/jf970695w

Available online at http://www.ssstj.sci.ssru.ac.th

Suan Sunandha Science and Technology Journal
©2022 Faculty of Science and Technology, Suan Sunandha Rajabhat University

Structural and Oxidation Behavior of Nanocomposite TiCrN Thin Films

Siriwat Alaksanasuwan[1,3*], Adisorn Buranawong[2,3] and Nirun Witit-anun[2,3]

[1]Faculty of Science and Technology, Phranakhon Si Ayutthaya Rajabhat University, Phranakhon Si Ayutthaya 13000, Thailand
[2]Department of Physics, Faculty of Science, Burapha University, Chonburi 20131, Thailand
[3]Thailand Center of Excellence in Physics (ThEP), MHESI, Bangkok 10400, Thailand
***Corresponding author e-mail: siriwat.aru@gmail.com**

Received: *17 February 2022* /**Revised**: *1 March 2022* / **Accepted:** *26 May 2022*

Abstract

The structural and oxidation behavior of nanocomposite titanium chromium nitride (TiCrN) thin films has been investigated by using x-ray diffraction (XRD), energy dispersive x-ray spectroscopy (EDS), and field emission scanning electron microscopy (FE-SEM). The TiCrN thin films were deposited on Si substrates by using the reactive DC magnetron sputtering technique from the Ti-Cr mosaic target. After that, the as-deposited thin films were annealed in the air at 500 - 900°C for 2 h. The XRD results showed that the formation oxidation of anatase-TiO_2, rutile-TiO_2, and Cr_2O_3 which diffraction peak appear from 500°C. The relative intensity of these oxide peaks varied with the annealed temperatures. By observing from FE-SEM, the aggregation of the grain increased with the annealing temperature. The cross-sectional results showed that the thin dense oxide overlayer occurred at 700°C and the oxide thickness increased gradually with the annealing temperature. Meanwhile, underneath the TiCrN grain grew above 700°C and become more void structure after annealing at 700°C. The dramatically increase of the oxygen content was found at 700°C and the evolution of Ti, Cr, N, and O with different elements compositions at various annealing temperatures were investigated from the EDS technique. The oxide layer obviously grows inward indicating the oxidation of TiCrN thin films belongs to inward oxidation. The oxidation rate of the films was increased with the increase of annealing temperature. The activation energy of the oxidation as evaluated by the Arrhenius-type relation was 168 kJ/mol.

Keywords: TiCrN thin film, Oxidation, Reactive sputtering, Mosaic target

1. Introduction

Nowadays, nano-layer hard coatings are very important in the manufacture of mechanical tools. This is because of high demand and its impact on the industrial part is those for surface hardening of conventional materials, which can be used efficiently to extend the lifetime of these tools (Solis-Pomar et al., 2016). Particularly, nitride coatings are commonly used as hard, wear-resistant, and anti-corrosion coatings because of their excellent properties (Santecchia et al., 2015). TiN was the first PVD ceramic coating used successfully to mechanical tools in the industry and it is still the most recognized (Alberdi, Marin, Diaz, Sanchez, & Galindo, 2007). However, the limitation of TiN is very rapid oxidation at temperatures above 500°C that easily induces shear off of the coating film and contributes to the degradation (Komarov, Konstantinov, Kovalchuk, Konstanttinov, & Tkachenko, 2016). It has been reported that the thermal oxidation resistance of TiN is considerably increased by the addition of chromium (Cr) in the TiN structure which leads to the ternary coating of TiCrN (Choi, Han, Hong, & Lee, 2009; Thampi, Bendavid, & Subramanian, 2016). Owing to the incorporation of Cr atom in the cubic fcc TiN structure influences the structure which leads to increase the hardness of TiN films from 20-25 GPa to 22-35 GPa and extended the oxidation resistance of the TiN films from 500°C to above 700°C (Chang, Yang, & Wang, 2007; Chen, Luo, & Zhao, 2013; Uglov, Anishchik, Zlotski, Abadias, & Dub, 2005; Vishnyakov et al., 2006). Hence, TiCrN coatings have become used as hard coatings for tools recently, in particular for high-speed cutting tools (Uglov et al., 2005).

Commonly, the TiCrN thin films can be prepared by two main PVD methods: evaporation (Chen et al., 2013; Wolfe, Gabriel, & Reedy, 2011) and sputtering (Krzanowski & Foley, 2014;

Suan Sunandha Science and Technology Journal
©2022 Faculty of Science and Technology, Suan Sunandha Rajabhat University

Paksunchai, Denchitcharoen, Chaiyakun, & Limsuwan 2012). The reactive magnetron sputtering is one of the most widely used methods to prepare thin films with large area uniformity and strong adhesion (Thampi et al., 2016). Moreover, a tactic in evolving the method of magnetron sputtering for depositing multicomponent thin films such as TiCrN films with any content of elements using a single magnetron is the use of a mosaic target (a target that consists of a regular target of Ti with inserts by Cr). Additionally, the sputtering by using a mosaic target may be suitable for deposited hard coatings with low mutual solubility or a great difference in melting temperatures (Alaksanasuwan, Buranawong, & Witit-Anun, 2020; Golosov, Melnikov, & Dostanko, 2012).

It is well known that the properties of thin films strongly depend on the microstructure of films which relates to the deposition parameters such as nitrogen gas flow rate, sputtering current, voltage bias, substrate temperature, partial or total pressure, and other parameters. Therefore, the effect of deposition parameters on the structural and properties of TiCrN thin films is still important. Furthermore, the demand to develop new hard coatings with good thermal stability has become essential to enhance tool life as machining speed increases (Chim, Ding, Zeng, & Zhang, 2009; Rizzo et al., 2013). Most high-temperature coatings depend on the formation of a protective oxide scaled by interaction with the environment (Chim et al., 2009). However, few annealing at high-temperature studies were performed on TiCrN thin film in terms of structure and properties. Therefore, the relation between thin films and their properties under various annealing temperatures is still essential to investigate.

This research work aimed to understand and discuss the structural and oxidation behavior of nanocomposite titanium chromium nitride (TiCrN) thin films deposited by the reactive DC magnetron sputtering using a mosaic target. Phase formation, morphological and elemental composition change during elevated temperature, which annealing the as-deposited thin films at high temperatures ranging from 500 to 900°C in air was investigated.

2. Experimental Details

TiCrN thin films in this research work were deposited on Si (100) substrate by the homemade vacuum coater as shown in Figure 1 with reactive DC magnetron sputtering technique from a mosaic target. The Ti-Cr mosaic target style, used in this research work, is made by embedding chromium rods (99.99%) into the high sputtering rate area of metal titanium (99.97%) disk, with a diameter of 54 mm and thickness of 3 mm thick. Pure Ar (99.999%) and N_2 (99.999%) were used as the sputtering and reactive gasses, respectively. Before deposition, the coating chamber was evacuated to a base pressure of 5×10^{-5} mbar. Previous to the deposition of the process of thin film, the pre-sputtering stage was start-up by ion bombardment from Ar^+ ions, which sputtered on the target to eliminate the surface impurities under a shutter shielding in about 5 min. The TiCrN films were deposited at 60 min, while the deposition parameters such as Ar and N_2 gas flow rate, sputtering power, substrate-target distances, substrate temperature, and working pressure were constant. The deposition parameters are summarized in Table 1.

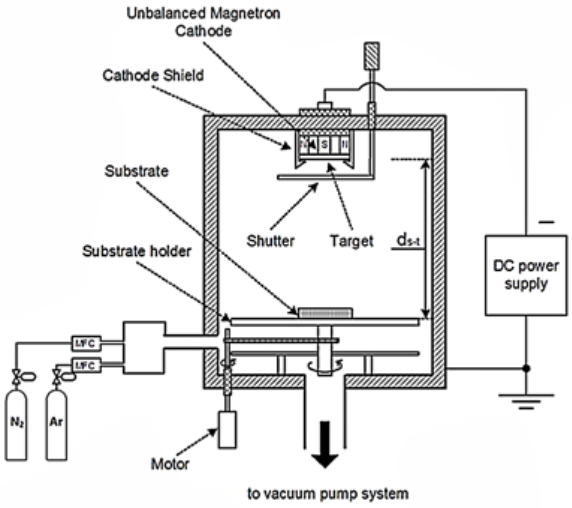

Figure 1. The homemade DC magnetron sputtering coater diagram.

Table 1. Deposition conditions of TiCrN thin films.

Parameters	Value
Sputtering targets	Mosaic of Ti-Cr
Substrate	Si (100)
Ar flow rate	16 sccm
N_2 flow rate	6 sccm
Base pressure	5.0×10^{-5} mbar

Suan Sunandha Science and Technology Journal
©2022 Faculty of Science and Technology, Suan Sunandha Rajabhat University

Working pressure	5.0×10^{-3} mbar
Sputtering Power	190 W
Target to substrate distance	15 cm
Deposition time	60 min

The crystalline structure of the as-deposited TiCrN thin film was analyzed by grazing-incidence X-ray diffraction (GIXRD: Bruker D8) using monochromatic Cu-k_α as an X-ray source ($\lambda = 0.154$ nm). The XRD patterns were acquired in a continuous mode, the 2θ scan angle range is between 20° and 80° with a measurement step of 0.02° min^{-1} and the grazing incidence angle of 3°. The phase of the film was determined using Bragg's law and interplanar spacing equation and compared with the Joint Committee on Powder Diffraction Standard (JCPDS) files. The microstructure, thickness, and cross-section structure of the thin films were observed by Field Emission Scanning Electron Microscope (FE-SEM: Hitachi s4700). The elemental composition of the TiCrN thin films was measured by energy-dispersive X-ray spectroscopy (EDS: EDAX) which connected to the Scanning Electron Microscope (SEM: LEO 1450VP).

The oxidation behavior of the TiCrN thin films was evaluated by the annealing process which was heated by a furnace (CARBOLITE: CWF1300) at a different temperature ranging from 500 to 900 °C with 100 °C increments for each step under the constant heating time of 2 h in the air atmosphere. After that, the oxidation behavior of thin films was investigated by XRD, FE-SEM, and EDS for identifying the formation of oxide structure, the cross-sectional oxide layer, and O content, respectively. In order to understand the oxidation behavior of the TiCrN films, the oxidation rate in cm^2/s, $k_p(T)$ related to the thickness of oxide layer from cross-sectional observation in cm, d and annealing time in s, t was calculated from Wagner's parabolic oxidation theory (Qi et al., 2013), whereby

$$d = 2[k_p(T) \times t]^{1/2} \quad (1)$$

The activation energy (E_a) in kJ of the films was obtained from the slope of the linear regression using the Arrhenius equation (Qi et al., 2013), whereby k_{p0} is the pre-exponential factor (cm^2/s), E_a is the activation energy (kJ), R is the gas constant (8.31 $J \cdot K^{-1} \cdot mol^{-1}$) and T is the annealing temperature (K), are calculated from

$$k_p(T) = k_{p0} \exp(-E_a/RT) \quad (2)$$

3. Results and Discussion

The X-ray diffraction patterns of the TiCrN films prepared on a Si wafer are shown in Figure 2. The lines at 2θ values of standard TiN and CrN with (111), (200), and (220) planes were exhibited for comparison purposes. The results from the XRD technique revealed that the crystal structures of the as-deposited TiCrN thin films prepared on Si wafers were revealed that the 2θ values of diffraction peaks varied between the TiN and CrN JCPDS standard data of 87-0633 and 77-0047, respectively, as shown in Figure 2. Moreover, the diffraction peaks varied between the TiN and CrN JCPDS standard structure. These results were according to the TiCrN (111), (200), and (220) plane.

The solid solution of (Ti,Cr)N film is a composite structure of TiN and CrN that has a similar crystal structure and nearby lattice parameter (Choi et al., 2009). Furthermore, it has been reported that the FCC B1-NaCl phase of the (Ti,Cr)N film was attained by using magnetron sputtering. (Choi et al., 2009; Paksanchai et al., 2012; Thampi et al., 2016). Actually, the solid solution of (Ti,Cr)N was formed whereby the Ti atoms were substituted by Cr atoms in TiN structure due to the atomic radius of Cr (0.1249 nm) is lesser than the radius of the Ti atom (0.1445 nm) (Paksanchai et al., 2012).

Figure 2 shows the XRD patterns of the TiCrN films after annealing, the results revealed that the diffraction angle of oxide structures for TiO_2 and Cr_2O_3 phases were found after annealing at 500°C and 600°C. These structures were in good agreement with the JCPDS standard no.89-4921 tetragonal TiO_2 anatase structure of (004) planes, JCPDS no. 89-4920 tetragonal TiO_2 rutile structure of (210) planes, and JCPDS no. 82-1484 rhombohedral Cr_2O_3 of (214) planes were obtained, respectively. Moreover, it was found that the crystallinity of these oxide structures increased with the increase of annealed temperatures from 500 to 600°C. Then, it was found that the crystal structure of films was changed after annealing at 700°C. The TiO_2 rutile structure of (101) planes were obtained, whereas other oxide phases still appeared, but it was found the dramatically decreased crystallinity of these

Suan Sunandha Science and Technology Journal
©2022 Faculty of Science and Technology, Suan Sunandha Rajabhat University

oxide phases. Lastly, the significantly increased crystallinity with strongly preferred orientations along TiO_2 (101) was noticed for the annealing temperature reaching 800℃. Additionally, the rhombohedral Cr_2O_3 phase of (113) appeared.

It could be attributed to the O_2 from the annealing atmosphere that reacted with the TiCrN thin films which resulted in forming the TiO_2 and Cr_2O_3 by oxidation mechanism (Chen & Lu, 2006). The crystallinity enhancement observed from X-ray intensity increased may be due to the aggregation deposited atom resulting in more order atom arrangement and the reduction of the defect during the annealing temperatures (Wang et al., 2013). Additionally, it was found that solid solution TiCrN thin film was changed to oxide structure of TiO_2 and Cr_2O_3 phases at annealed above 500°C from XRD analysis. Therefore, the TiCrN films in this work can resist thermal oxidation at 500°C.

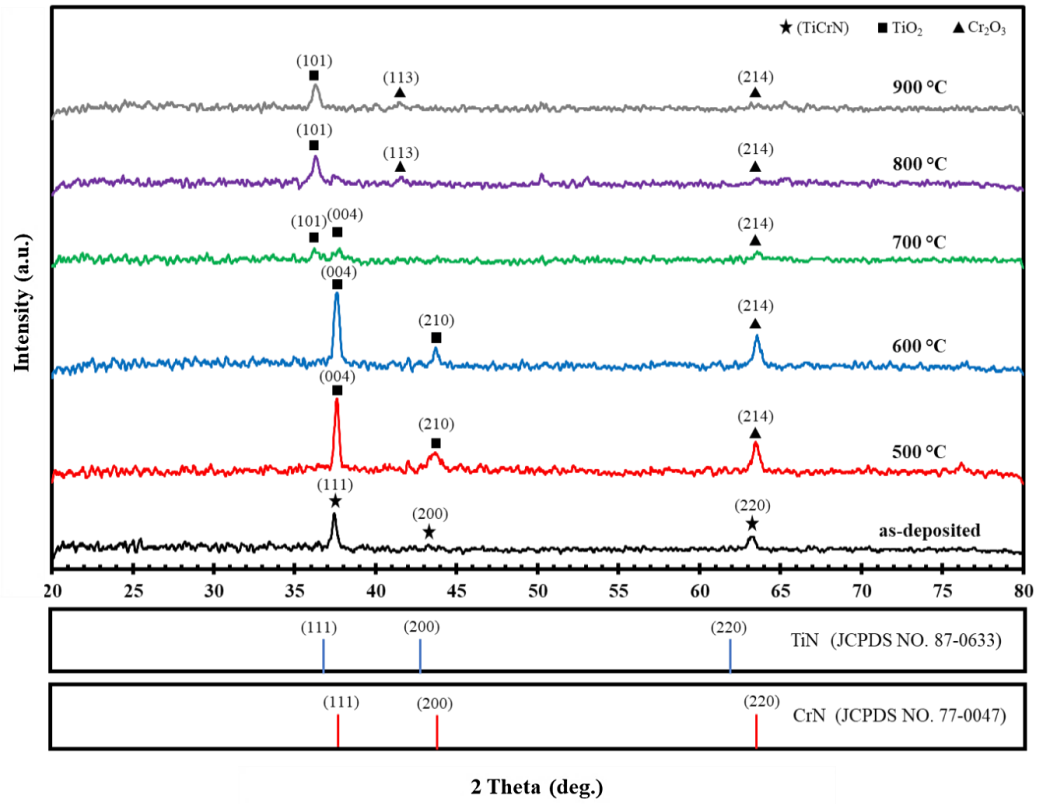

Figure 2. X-ray diffraction patterns of the TiCrN thin film before and after annealing.

The EDS result shows the as-deposited thin film and annealed thin film's chemical composition as a function of the annealing temperature in the air environment (Table 2 and Figure 3). As the annealing temperature below 600℃, the TiCrN thin films contained the Ti, Cr, N, and O composition of about 9, 21, 40, and 30 at.%, respectively. As the annealing temperature elevated above 700℃, it was found that the N content in the films was dramatically decreased from about 40 to 10 at.%, whereas a complete addition of the O contents in the films from about 30 to 60 at.%. Meanwhile, the Ti and Cr contents were still in the range of 7.38 to 7.51 at.% and 17.23 to 18.26 at.%, respectively.

It could be concluded that the elemental composition analysis results are in good agreement with the findings of the crystal structure characterization. It suggested that the thin films annealed at over 700℃ changed the structure of film with phase segregation owing to the heating process. The continuous increase of O contents after annealing is because the O_2 from the ambient atmosphere was diffused into the film and replaced as the N atoms in TiCrN films resulting from the dramatically decrease of N content by the oxidation mechanism during annealing temperature (Aliaj, Syla, Oettel, & Dilo, 2016). Consequently, the increase of O content from the EDS technique can

Suan Sunandha Science and Technology Journal
©2022 Faculty of Science and Technology, Suan Sunandha Rajabhat University

obviously be confirmed that the thin film oxidation occurred.

Table 2. The compositions and thickness of the TiCrN thin films at different annealing temperatures.

Annealing temperature (°C)	Thin film thickness (nm)	Compositions (at.%)			
		Ti	Cr	N	O
As-deposited	532	8.77	21.00	40.36	29.87
500	534	8.72	20.64	40.20	30.44
600	540	8.69	20.80	39.94	30.56
700	556	7.38	17.23	25.90	49.49
800	665	7.36	17.64	16.93	58.07
900	627	7.51	18.26	10.74	63.49

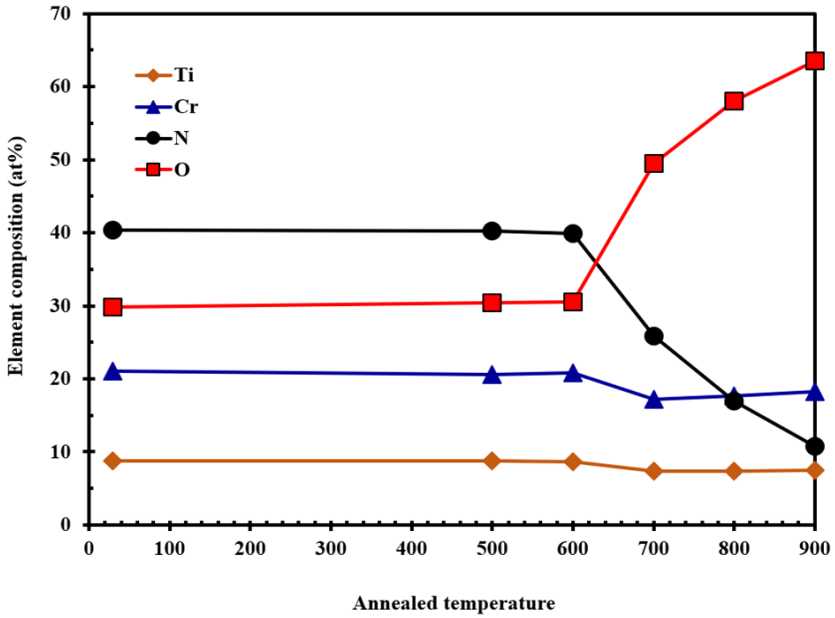

Figure 3. The element compositions of TiCrN thin films as a function of as-deposited to annealing temperatures.

The microstructure and the cross-sectional of the TiCrN thin films after the annealing process in the range of 500 to 900°C for 2 hours in the air were observed by the FE-SEM technique as shown in Figure 4 and 5. Firstly, Figure 4 exposes the films after the annealing process. Small grains and smooth surfaces were also found over the surface of the as-deposited films (Figure 4a). As the annealing temperature at 500 and 600°C, it can be seen that the surface pattern was stilled unchanged from the as-deposited films (Figure 4b and 4c). Thus, the TiCrN thin films in this work were also shown the thermal oxidation resistance up at 600°C. As the annealing temperature increased up to 700°C, it was found that countless grains with different shapes and sizes with a void between the grain boundaries were observed (Figure 4d). Grain aggregation, more void, and increased their sizes were identified when the annealing temperature reached 800°C (Figure 4e). Lastly, the surface of films at the highest annealing temperature of 900°C revealed that the grains are found to be continuous (Figure 4f).

The changing of grain sizes resulting from the increasing of the annealing temperature was investigated. The grain sizes growing with increasing of the annealing temperature may be controlled by a mechanism that the energy additional provided by higher annealing temperature formerly increases the mobility of deposited atoms resulting in grain coalescence (Mayrhofer, Willmann, & Mitterer, 2001). Additionally, it could be explained by considering the annealing induced

Suan Sunandha Science and Technology Journal
©2022 Faculty of Science and Technology, Suan Sunandha Rajabhat University

coalescence of small grains by grain boundary diffusion which resulted in major grain growth (Jafari et al., 2014).

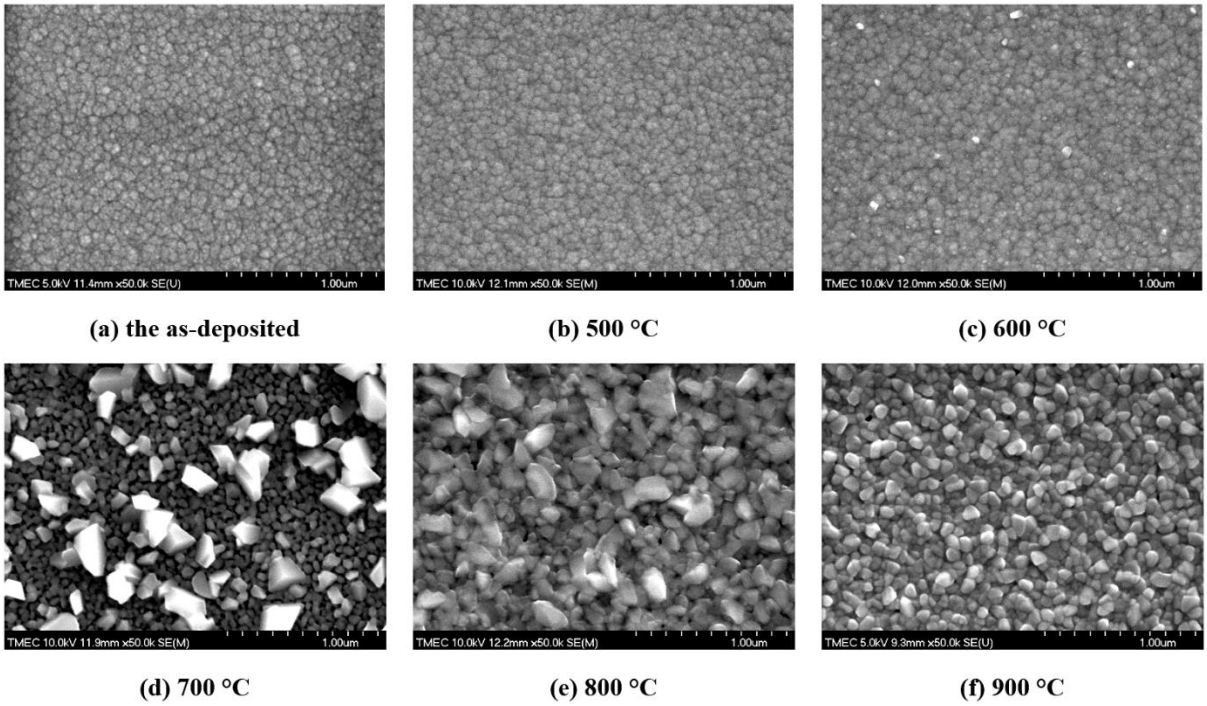

Figure 4. FE-SEM micrographs of TiCrN thin films annealed at different temperatures.

Figure 5 presents the FE-SEM images of the cross-section of TiCrN films after the annealing process. The microstructure of the as-deposited TiCrN thin films consists of columnar growth due to the nearly equiaxed grains stacked one upon other such that grain size is similar to the column diameter (Figure 5a). After annealing at high temperature, it was found that the cross-section observation apparently reveals the film also performs a columnar pattern as the annealing temperature at 500 to 600°C (Figure 5b and 5c). A non-columnar formation can be observed and appear as a facet grain with a void at over 700°C (Figure 5d). At an annealing temperature up to 800°C, grains combine forming a polygon shape structure and increasing their void between grains (Figure 5e). Finally, for annealed at 900°C showed less voided but significant in grain coalescence (Figure 5f).

It can be confirmed that the TiCrN thin films in this research work were also shown the thermal oxidation resistance at 500°C. At a higher temperature of above 700°C, the cross-section structure of the TiCrN thin films was changed to an oxide structure owing to the thermal oxidation process. Moreover, it is clearly seen that after annealing, the cross-sectional transformation can be seen due to the higher annealing temperature, the grain mobility increases, and more the coalescence of the grain. Hence, the FE-SEM results in this work can visibly confirm that the annealing temperature can be influenced by the cross-sectional morphology of the films.

Suan Sunandha Science and Technology Journal
©2022 Faculty of Science and Technology, Suan Sunandha Rajabhat University

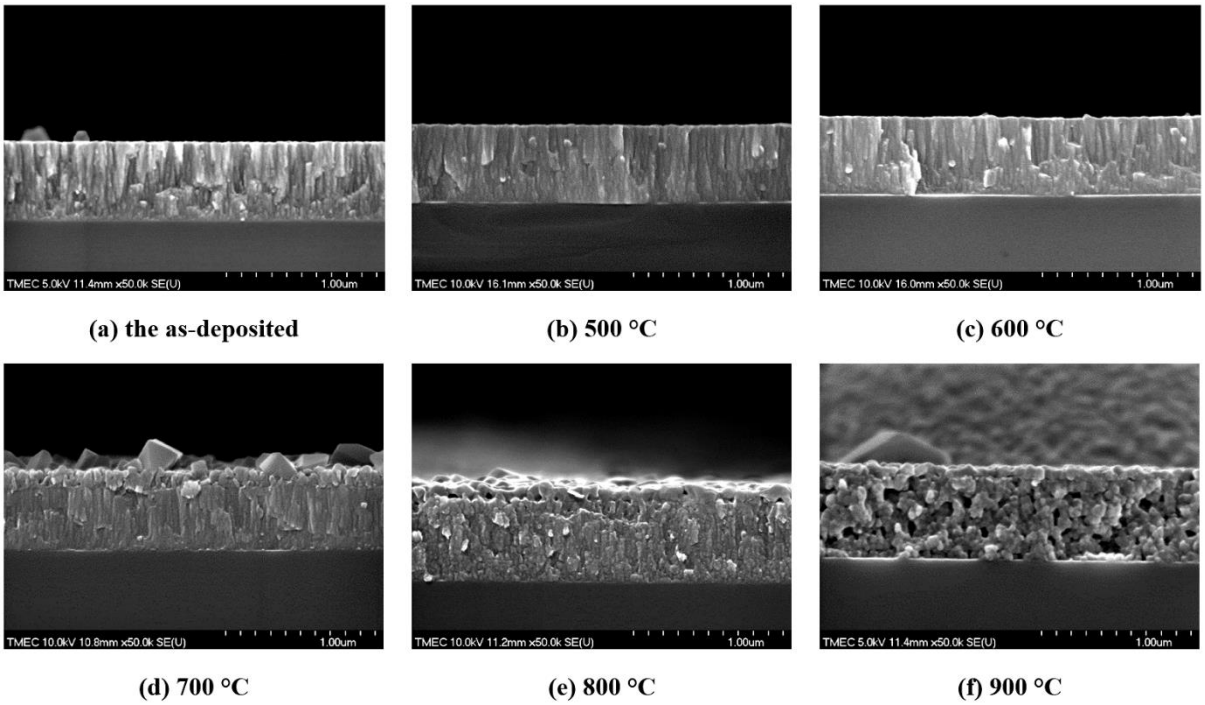

Figure 5 FE-SEM cross-section of TiCrN thin films annealed at different temperatures.

The oxidation rate, $k_p(T)$ at a given oxidation temperature of TiCrN thin film was obtained from the parabolic relation as shown in Table 3. It was revealed that the increase of oxidation rate from 4.05×10^{-15} to 1.36×10^{-13} cm^2/s as the annealing temperature increased from 700 to 900ºC. The activation energy (E_a) is evaluated from the Arrhenius equation. The Arrhenius plot of $\ln[k_p(T)]$ as a function of 1/1000 T for oxidized TiCrN thin film was shown in Figure 6. In this work, the activation energy of TiCrN thin film was calculated as 168 kJ/mol. It was found that the activation energy of TiCrN thin films in this study was different from other works. Otani and Hofmann have reported the activation energy of TiCrN films were the range of 120-140 kJ of annealing temperature ranging from 400 to 700°C for 10 and 300 min in the air (Otani & Hofmann, 1996). Nevertheless, the TiCrN films in their work were prepared by reactive magnetron co-sputtering technique at varied Ti/Cr ratios and the thickness of films was controlled at 2-3 µm. Therefore, the oxidation behavior may be depending on the stoichiometry or thickness of films.

Table 3. The film thickness, oxide thickness, and oxidation rate of the TiCrN thin films and after annealing in the air for 2 h at various temperatures ranging from 500 to 900°C.

Annealing Temperature (ºC)	Film thickness (nm)	Oxide thickness (nm)	Oxidation rate (cm^2/s)
As-deposited	532	-	-
500	534	-	-
600	540	-	-
700	556	108	4.05×10^{-15}
800	665	345	4.13×10^{-14}
900	627	627	1.36×10^{-13}

Suan Sunandha Science and Technology Journal
©2022 Faculty of Science and Technology, Suan Sunandha Rajabhat University

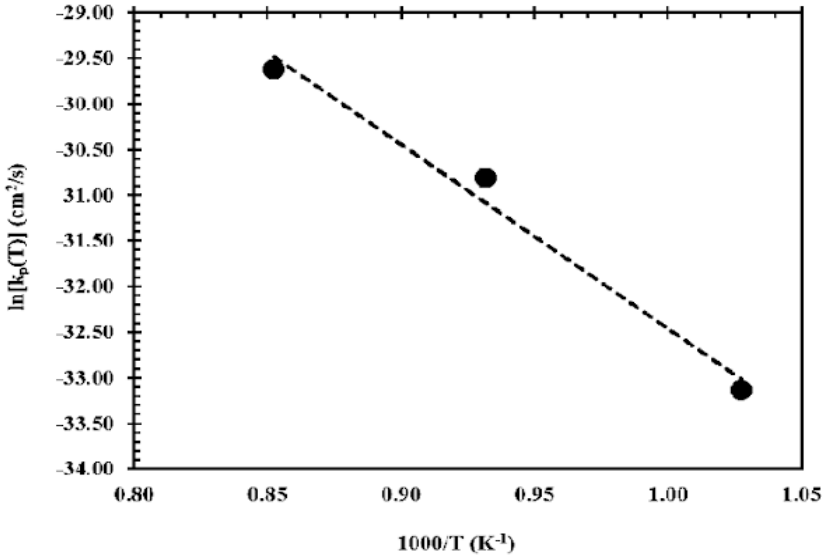

Figure 6. The Arrhenius plot of the TiCrN thin films oxidized at various annealing temperatures.

4. Conclusion

The structural and oxidation behavior of nanocomposite titanium chromium nitride (TiCrN) thin films, deposited on Si substrates by using the reactive DC magnetron sputtering technique from the mosaic target, was characterized between 500 and 900ºC in the air using XRD, EDS, and FE-EM techniques. It was found that the annealing temperature strongly influences the structure of the thin films. The transformation of polycrystalline TiCrN to TiO_2 and Cr_2O_3 structure, in which the relative intensity of these oxide peaks varied with the annealed temperatures, were obtained from XRD patterns. The changing of grains has resulted from the increase of annealing temperature as investigated from the FE-SEM. The cross-sectional results showed that the thin dense oxide layer occurred at 700°C and the oxide thickness increased gradually with the annealed temperature. Meanwhile, underneath the TiCrN grain grew above 700°C and become more void structure after annealing at 700°C. The oxide layer obviously grows inward indicating the oxidation of TiCrN thin films belongs to inward oxidation. The EDS result was also in good agreement with the XRD technique that the crystal structure, of the TiCrN films, changed which significantly increased of the O content but rapidly decreased and was constant of the Ti, Cr, and N contents when annealed the films from 700°C. The oxidation rate of the films was increasing from 4.05×10^{-15} to 1.36×10^{-13} cm^2/s with the increase of annealing temperature. The activation energy of the oxidation as evaluated by the Arrhenius-type relation was 168 kJ/mol.

5. References

Alaksanasuwan, S., Buranawong, A., & Witit-Anun, N. (2020). Effect of sputtering current on the structure of TiCrN thin films prepared from mosaic target by reactive DC magnetron sputtering. *Applied Mechanics and Materials*, *901*, 37-42. doi:10.4028/www.scientific.net/AMM.901.37

Alberdi, A., Marin, M., Diaz, B., Sanchez, O., & Galindo, R. E. (2007). Wear resistance of titanium-aluminium-chromium-nitride nanocomposite thin films. *Vacuum*, *81*, 1453-1456. doi:10.1016/j.vacuum.2007.04.024

Aliaj, F., Syla, N., Oettel, H., & Dilo, T. (2016). Thermal treatment in air of direct current (DC) magnetron sputtered TiN coatings. *Scientific Research and Essays*, *11*(21), 230-238. doi:10.5897/SRE2016.6456

Chang, Y.-Y., Yang, S.-J., & Wang, D.-Y. (2007). Characterization of TiCr(C,N)/amorphous carbon coatings synthesized by a cathodic arc deposition process. *Thin Solid Films*, *515*, 4722-4726. doi:10.1016/j.tsf.2006.11.028

Chen, H. Y., & Lu, F. H. (2006). Oxidation behavior of chromium nitride films. *Thin Solid Films*, *515*, 2179-2184. doi:10.1016/j.tsf.2006.06.039

Suan Sunandha Science and Technology Journal
©2022 Faculty of Science and Technology, Suan Sunandha Rajabhat University

Chen, S., Luo, D., & Zhao, G. (2013). Investigation of the properties of $Ti_xCr_{1-x}N$ coatings prepared by cathodic arc deposition. *Physics Procedia*, *50*, 163-168. doi:10.1016/j.phpro.2013.11.027

Chim, Y. C., Ding X. Z., Zeng, X. T., & Zhang, S. (2009). Oxidation resistance of TiN, CrN, TiAlN and CrAlN coatings deposited by lateral rotating cathode arc. *Thin Solid Films*, *517*, 4845-4849. doi:10.1016/j.tsf.2009.03.038

Choi, H. S., Han, D. H., Hong, W. H., & Lee, J. J. (2009). (Titanium, chromium) nitride coatings for bipolar plate of polymer electrolyte membrane fuel cell. *Journal of Power Sources*, *189*, 966-971. doi:10.1016/j.jpowsour.2008.12.060

Golosov, D. A., Melnikov, S. N., & Dostanko, A. P. (2012). Calculation of the elemental composition of thin films deposited by magnetron sputtering of mosaic targets. *Surface Engineering and Applied Electrochemistry*, *48*, 52-59. doi:10.3103/S1068375512010073

Jafari, A., Ghoranneviss, Z., Solar Elahi, A., Ghoranneviss, M., Fasihi Yazdi, N., & Rezaei, A. (2014). Effects of annealing on TiN thin film growth by DC magnetron sputtering. *Advances in Mechanical Engineering*, *2014*, 1-6. doi:10.1155/2014/373847

Komarov, F. F., Konstantinov, V. M., Kovalchuk, A. V., Konstantinov S. V., & Tkachenko, H. A. (2016). The effect of steel substrate pre-hardening on structural, mechanical, and tribological properties of magnetron sputtered TiN and TiAlN coating. *Wear*, *352-353*, 92-101. doi:10.1016/j.wear.2016.02.007

Krzanowski, J. E., & Foley, D. J. (2014). The effect of Cr content on the oxidation behavior of Ti-Cr-N films. *Coatings*, *4*, 308-319. doi:10.3390/coatings4020308

Mayrhofer, P. H., Willmann, H., & Mitterer, C. (2001). Oxidation kinetics of sputtered Cr-N hard coatings. *Surface and Coatings Technology*, *146-147*, 222-228. doi:10.1016/s0257-8972(01)01471-2

Otani, Y., & Hofmann, S. (1996). High temperature oxidation behaviour of $(Ti_{1-x}Cr_x)N$ coatings. *Thin Solid Films*, *287*, 188-192. doi:10.1016/s0040-6090(96)08789-5

Paksunchai, C., Denchitcharoen, S., Chaiyakun, S., & Limsuwan, P. (2012). Effect of sputtering current on structure and morphology of $(Ti_{1-x}Cr_x)N$ thin films deposited by reactive unbalanced magnetron co-sputtering. *Procedia Engineering*, *32*, 875-881. doi:10.1016/j.proeng.2012.02.026

Qi, Z. B., Liu, B., Wu, Z. T., Zhu, F. P., Wang, Z. C., & Wu, C. H. (2013). A comparative study of the oxidation behavior of Cr_2N and CrN coatings. *Thin Solid Films*, *544*, 515-520. doi:10.1016/j.tsf.2013.01.031

Rizzo A., Mirenghi, L., Massaro, M., Galietti, U., Capodieci, L., Terzi, R., … Valerini, D. (2013). Improved properties of TiAlN coatings through the multilayer structure. *Surface and Coatings Technology*, *235*, 475-483. doi:10.1016/j.surfcoat.2013.08.006

Santecchia, E., Hamouda, A. M. S., Musharavati, F., Zalnezhad, E., Cabibbo, M., & Spigarelli, S. (2015). Wear resistance investigation of titanium nitride-based coatings. *Ceramics International*, *41*, 10349-10379. doi:10.1016/j.ceramint.2015.04.152

Solis-Pomar, F., Nápoles, O., Vázquez Robaina, O., Gutierrez-Lazos, C., Fundora, A., Colin, A., … Melendrez, M. F. (2016). Preparation and characterization of nanostructured titanium nitride thin films at room temperature. *Ceramics International*, *42(6)*, 7571-7575. doi:10.1016/j.ceramint.2016.01.164

Thampi, V. V. A., Bendavid, A., & Subramanian, B. (2016). Nanostructured TiCrN thin films by pulsed magnetron sputtering for cutting tool applications. *Ceramics International*, *42*, 9940-9948. doi:10.1016/j.ceramint.2016.03.095

Uglov, V. V., Anishchik, V. M., Zlotski, S. V., Abadias, G., & Dub, S. N. (2005). Stress and mechanical properties of Ti-Cr-N gradient coatings deposited by vacuum arc. *Surface and Coatings Technology*, *200*, 178-181. doi:10.1016/j.surfcoat.2005.02.136

Vishnyakov, V. M., Bachurin, V. I., Minnebaev, K. F., Valizadeh, R., Teer, D. G., Colligon, J. S., … Yurasova, V. E. (2006). Ion assisted deposition of titanium chromium nitride. *Thin Solid Films*, *497*, 189-195. doi:10.1016/j.tsf.2005.05.005

Suan Sunandha Science and Technology Journal
©2022 Faculty of Science and Technology, Suan Sunandha Rajabhat University

Wang, F., Wu, M. Z., Wang, Y. Y., Yu, Y. M., Wu, X. M., & Zhuge, L. J. (2013). Influence of thickness and annealing temperature on the electrical, optical and structural properties of AZO thin films. *Vacuum*, *89*, 127-131. doi:10.1016/j.vacuum.2012.02.040

Wolfe, D. E., Gabriel, B. M., & Reedy, M. W. (2011). Nanolayer (Ti,Cr)N coatings for hard particle erosion resistance. *Surface and Coatings Technology*, *205*, 4569-4576. doi:10.1016/j.surfcoat.2011.03.121

Available online at http://www.ssstj.sci.ssru.ac.th

Suan Sunandha Science and Technology Journal
©2022 Faculty of Science and Technology, Suan Sunandha Rajabhat University

Simple Method to Synthesize g-C_3N_4 Doped Sn to Reduce Bandgap Energy (E_g)

Chumphol Busabok*, Wasana Khongwong, Piyalak Ngernchuklin

Expert Centre of Innovative Materials, Thailand Institute of Scientific and Technological Research,
35 Mu 3, Khlong Ha, Khlong Luang, Pathum Thani 12120, Thailand
***Corresponding author e-mail: chumphol@tistr.or.th**

Received: *21 February 2022* / **Revised**: *14 March 2022* / **Accepted**: *14 June 2022*

Abstract

Graphitic carbon nitride (g-C_3N_4) has been highlighted in its unique electronic structure with a medium bandgap, high thermal and chemical stability in the ambient environment. It is promoted as a photocatalytic material. To enhance photocatalytic properties, Sn-modified g-C_3N_4 was synthesized from urea and Sn powder. Firstly, urea was fired at 450-650°C in the air to synthesize g-C_3N_4 powder. Then such g-C_3N_4 powder was mixed with Sn powder for 0.1, 0.3, and 0.5 mole ratio and fired at 550°C in ambient. To investigate the phase formation and light absorption, XRD and light absorption spectrophotometers were performed, respectively. The light absorption value was used to calculate band gap energy (E_g). It was found that the XRD results of synthesized g-C_3N_4 were on the broad peak to narrow peak in synthesized temperatures 450-650°C. The light absorption of synthesized powder at 550°C was higher than others. Thus, synthesized powder at 550°C was chosen to mix with Sn powder. It observed that E_g of Sn-modified g-C_3N_4 decreased depending on the amount of Sn and synthesized temperatures.

Keywords: Graphitic carbon nitride, Bandgap energy, Light absorption

1. Introduction

Graphitic carbon nitride (g-C_3N_4) is a metal-free and conjugated polymeric with a formula of $(C_3N_3H)_n$ in which covalent C-N bonds called tri-s-triazine unit connected with planar amino acid groups in the layer and hold together with van der Waals forces. This structure makes it excellent in thermal and chemical stability and stable allotrope (Kong et al., 2021). It possesses an electronic structure with a narrow bandgap (2.7 eV.) and is responsible for visible light photocatalyst at 400-450 nm (Song et al., 2019). Since then, g-C_3N_4 has much attention in many applications including organic pollutants, remediation environment (Alulema-Pullupaxi et al., 2021), hydrogen evolution (Naseri, Samadi, Pourjavadi, Moshfegh, & Ramakrishna, 2017) and fuel cell (Zheng, Liu, Liang, Jaroniec, & Qiao, 2012), water spitting (Neelakanta Reddy et al., 2021) and antibacterial activity (Huang, Ho, & Wang, 2014; Neelakanta Reddy et al., 2021). However, pristine g-C_3N_4 shows less efficiency due to low surface area resulting in a low active site, high charge recombination rate and small harvest of solar energy (Wen, Xie, Chen, & Li, 2017). So, to obtain high photocatalytic activities, tailoring and customizing of the structures by doping with metallic (Shanmugam, Muppudathi, Jayavel, & Jeyaperumal, 2020; Van et al., 2022) and/or non-metallic elements (Li et al., 2014), and hybridization (Zhang, Yu, Sun, & Zheng, 2018) have been performed. Some researchers applied some solutions by reducing E_g with S-scheme heterojunctions (Van Viet et al., 2021). Therefore, the aim of this research was to study the effect of metallic Sn powder doped in g-C_3N_4 to reduce band gap energy (E_g). The mixing and calcination of urea and Sn powder were performed at 550°C in air atmospheric by tube furnace. The observation of synthesized g-C_3N_4 and Sn-doped g-C_3N_4 powders including phase analysis, crystal size, light absorption together with

Suan Sunandha Science and Technology Journal
©2022 Faculty of Science and Technology, Suan Sunandha Rajabhat University

photocatalytic efficiency such as calculated E_g and degradation of methylene blue were performed and discussed.

2. Materials and Methods

2.1 Synthesis of g-C_3N_4

The g-C_3N_4 powder was prepared by the simple method, the 20 g of urea powder was used as a precursor and placed in an alumina crucible and followed by heated up in a tube furnace at 400ºC-650ºC with the interval of 50ºC in air atmosphere for 0.5, 2 and 3 h. The synthesized powders were characterized by XRD (1.54 ºA Cu, Shimazu XRD6000). The crystal size was calculated from the main peak of g-C_3N_4 by measuring full-width half maximum (FWHM) and calculated by Scherrer's equation (1).

$$D = K\lambda/\beta\cos\theta \quad (1)$$

Where K = 1

D is crystal size

λ is the wavelength of the x-ray

β is FWHM

θ is diffraction angle

The light absorption of synthesized powder was measured by UV-Vis-NIR spectrophotometer (ES Avalight-DHS; Detector AvaSpec-2048L; UV/Vis/NIR range from 200 to 2500 nm). And band gap energies (E_g) of the synthesized powders were calculated from light absorption data as followed (2):

$$E_g\,(eV) = hC/\lambda = 1239.8/\lambda \quad (2)$$

Where *h* is Plank's constant

C is speed of light

λ is cut off wavelength

2.2 Synthesis of g-C_3N_4 doped Sn

For the Sn doping, the g-C_3N_4 powder with the best light absorption from 2.1 was doped with Sn powder for 0.1, 0.3 and 0.5 % by mole. The two materials were continued dry mixing and heated up at 550ºC in an air atmosphere for 0.5 h in an alumina crucible. The obtained Sn-doped g-C_3N_4 were examined phase, light absorption and calculated band gap energies (E_g) as the same equipment in section 2.1.

2.3 Methylene blue degradation testing

For methylene blue degradation testing, 50 mg of g-C_3N_4 or Sn doped g-C_3N_4 were dispersed in 5 ppm of methylene blue solution (50 ml.) and illuminated by 50 watts, 110 Ln/watt LED lamp for 1-12 hrs. The light absorption of methylene blue was measured by UV-Vis-NIR spectrophotometer to observe the degradation rate of methylene blue from decreasing concentration. The formula of the degradation was calculated as followed (3):

$$\text{Degradation (\%)} = [(C_0 - C)/C_0]x100\% \quad (3)$$

Where C_0 is the initial concentration of methylene blue

C is the concentration at a time t.

3. Results and Discussions

3.1 The effect of synthesized temperature on phase and light absorption of g-C_3N_4

The results of phase analysis, crystal size and light absorption by XRD and UV-Vis-NIR, respectively, of the obtained g-C_3N_4 powders at 400ºC-650ºC in the air atmosphere were demonstrated. XRD graph (Figure 1) showed that urea (CH_2N_2O) was gradually decomposed to ammeline ($C_3H_5N_5O$) at 400ºC and completely changed at 450ºC. After heating up to 500ºC and higher, ammeline was transformed to g-C_3N_4 phase according to JCPDS card number of 75-0454. The highest peak of XRD at 2θ of 27.8 was used to calculate crystal size by Full width-half max (FWHM) and equation (1). The obtained crystal size of g-C_3N_4 was increased by increasing temperature (Figure 2). However, the oxidation reaction occurred at 550ºC and higher, resulting in a small amount of g-C_3N_4 being yielded. The light absorptions of g-C_3N_4 at various synthesized temperatures (Figure 3) were not significantly different and all calculated

Suan Sunandha Science and Technology Journal
©2022 Faculty of Science and Technology, Suan Sunandha Rajabhat University

E_g of powders were approximately 2.82 eV. However, E_g of g-C_3N_4 at 550ºC was a little higher than other synthesized temperatures. Thus, such powder at 550ºC was used to study for tin-doped g-C_3N_4 in the further experiment.

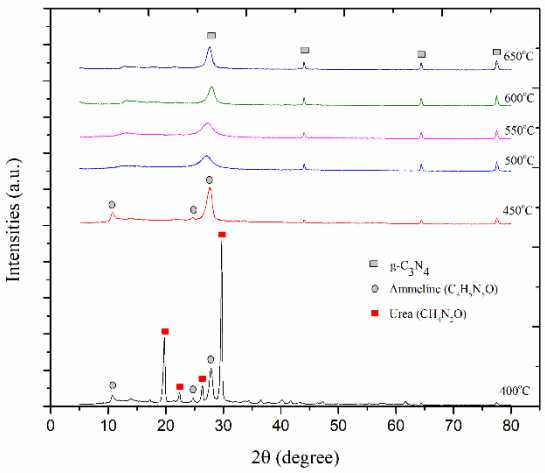

Figure 1. XRD patterns of the g-C_3N_4 powders calcined at temperatures of 400-650ºC.

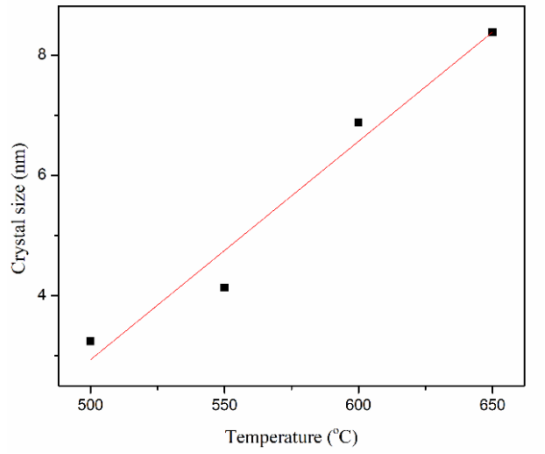

Figure 2. The relationship of g-C_3N_4 crystal sizes to calcination temperatures.

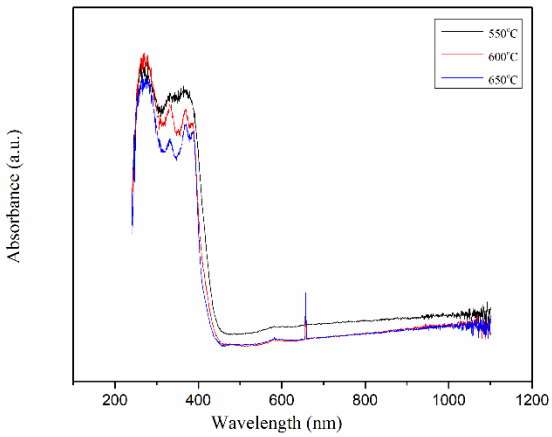

Figure 3. Light absorbance of g-C_3N_4 powders at different calcination temperatures.

3.2 The effect of soaking time on phase and light absorption of g-C_3N_4

From the previous section, the g-C_3N_4 powder calcined at 550ºC in the air atmosphere was chosen to study the effect of soaking time for 0.5, 2 and 3 hrs. The results of phase analysis, crystal size and light absorptions were shown in Figures 4-6, respectively. All samples showed absolutely g-C_3N_4 phase (Figure 4) without any residue precursor. The crystal size of the obtained g-C_3N_4 powders were increased when longer soaking time proceeded. The crystal size of 0.5, 2 and 3 hrs soaking was about 4.01, 4.32 and 6.75 nm, respectively (Figure 5). The light absorptions at various soaking times (0.5 and 3 hrs) (Figure 6) were not significantly different and calculated E_g were approximately 2.63 eV. Thus, the least soaking time of 0.5 h was used to study for tin-doped g-C_3N_4 in the further experiment.

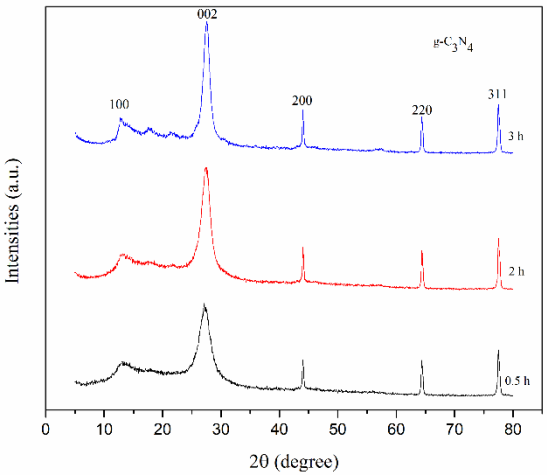

Figure 4. XRD patterns of the g-C_3N_4 powder at various soaking times.

Suan Sunandha Science and Technology Journal
©2022 Faculty of Science and Technology, Suan Sunandha Rajabhat University

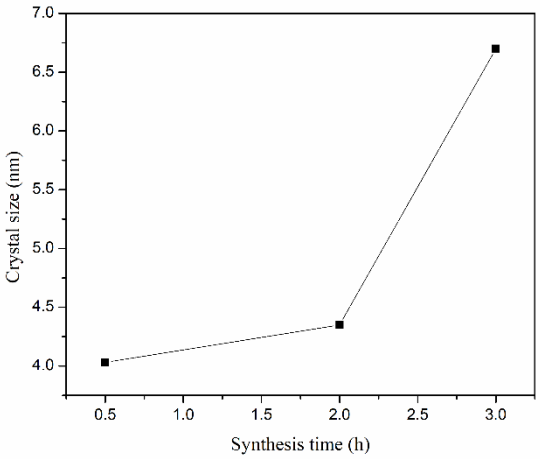

Figure 5. The relationship of g-C_3N_4 crystal size to the soaking time.

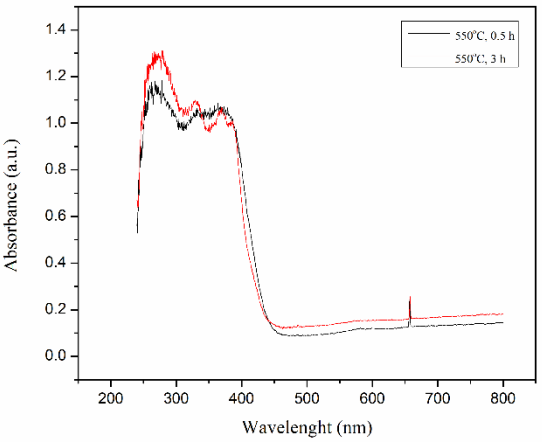

Figure 6. Light absorbance of g-C_3N_4 powder at various soaking times

3.3 The effect of Sn doped g-C_3N_4 on phase and light absorption

The g-C_3N_4 powder synthesized at temperature 550°C for 0.5 h. was doped with metallic Sn powder at 0.1, 0.3 and 0.5 mole percent, dry mixing and then heated up again at 550°C for 0.5 h in the air atmosphere. The results of phase analysis light absorption and calculated E_g were shown in Figures 7-10. Figure 7, XRD graph showed less crystalline g-C3N4 phase due to Sn substituted in the carbon position of the g-C_3N_4 structure. The more doping content, the higher the amorphous phase was obtained. The limitation of Sn doped was about 0.5 % by mole because some Sn was oxidized to form SnO_2 and so at this Sn content, g-C_3N_4 changed the structure. This could be observed by no sharp peak as found in Figure 4. The light absorption from the end of the ultraviolet to visible light range (280-400 nm) was increased in Figure 8. Moreover, light absorption had trended to higher by increasing the amount of Sn dopant. The calculated E_g (Figures 9 and 10) was reduced from 2.82 (g-C_3N_4) to 1.98 eV (doped 0.5 % mole Sn g-C_3N_4). The cause of decreasing in Eg can be predicted in two ways, first, when Sn was oxidized, it became SnO_2, which led to electron transfer from g-C_3N_4 to SnO_2 at interface heterojunction until the electric potential of Fermi level would be the same (Van et al., 2022). This phenomenon exhausts the electron region on g-C_3N_4 and electron deposition layer on SnO2 resulting in an internal electric field (IEF) directed from g-C_3N_4 to SnO_2. Second, Sn had substituted to the C-position in g-C_3N_4 structure, resulting in increased electrical conductivity and change in color to near red. Therefore, it could absorb visible light at an extended wavelength. In this case, there was a high probability that the two above possibilities could occur. The effect of Sn on altered properties of g-C_3N_4 was increasing the absorption of the visible light from 450 to 650 nm., covering to yellow, making it able to absorb light from the natural source (Solar) or LED lamps with the highest intensities in the blue to yellow as shown in Figure 11. The high light absorption of photocatalytic materials allows them to be better activated to the photocatalytic mechanism which the results of the experiment in section 3.4 can confirm this statement.

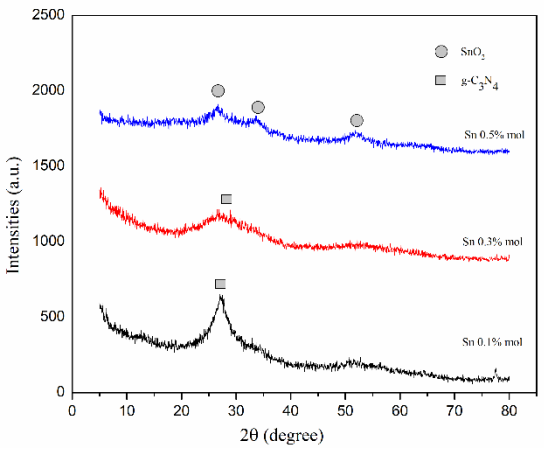

Suan Sunandha Science and Technology Journal
©2022 Faculty of Science and Technology, Suan Sunandha Rajabhat University

Figure 7. XRD patterns of the g-C_3N_4 powder with various amounts of Sn doping.

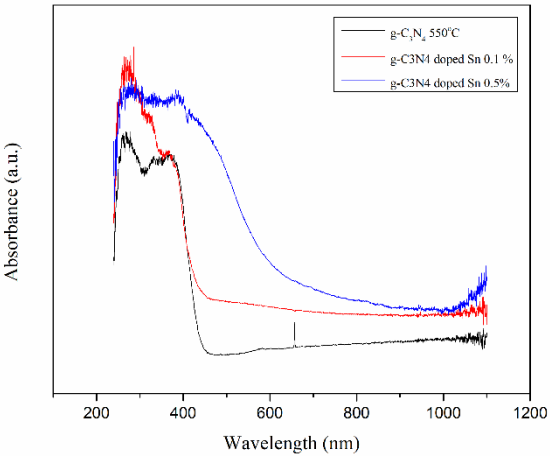

Figure 8. Light absorbance of g-C_3N_4 powder with various amounts of Sn doping.

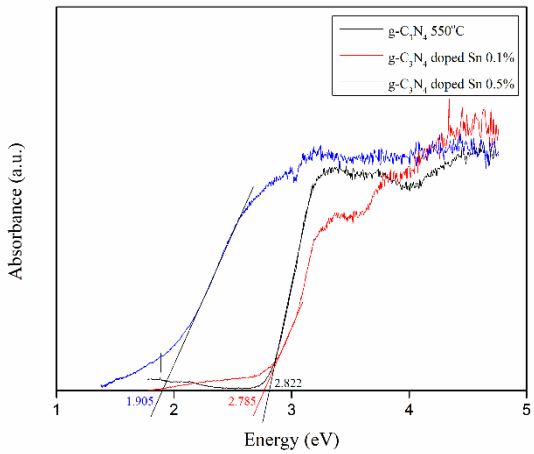

Figure 9. bandgaps of g-C_3N_4 with difference doped Sn.

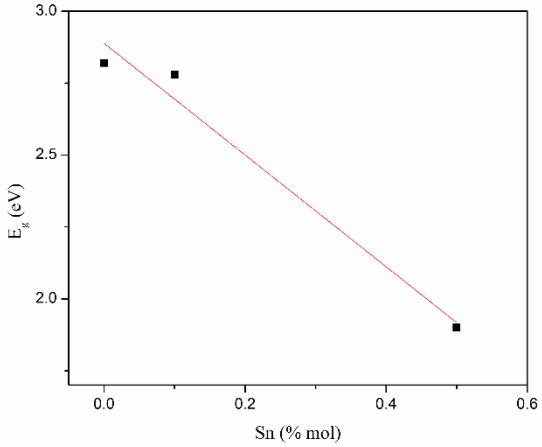

Figure 10. E_g of Sn doped g-C_3N_4 powders

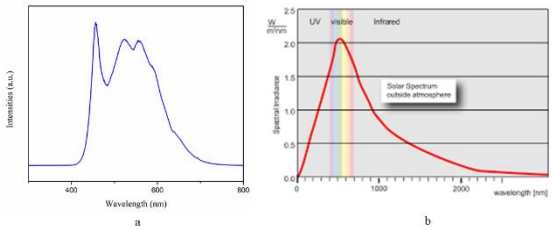

Figure 11. Light source spectrum (a) LED spectrum and (b) solar spectrum.

3.4 Methylene blue degradation testing results

The results of methylene blue degradation testing of g-C_3N_4 and 0.5 Sn-doped g-C_3N_4 were shown in Figures 12-14 and 15-17, respectively. By using visible light 500-700 nm to expose photocatalytic materials, it was found that the g-C_3N_4 absorbed more light when longer time radiation was exposed resulting in higher degradation of methylene blue. At the 12th h, methylene blue was completely clear color. While degradation 0.5 Sn-doped g-C_3N_4 was complete at the 8th h of light irradiation. From the two experiments, it could conclude that photocatalytic performance of 0.5 % mol Sn-doped g-C_3N_4 was more effective than g-C_3N_4 and its reaction was faster than that of g-C_3N_4 about 2.45 times.

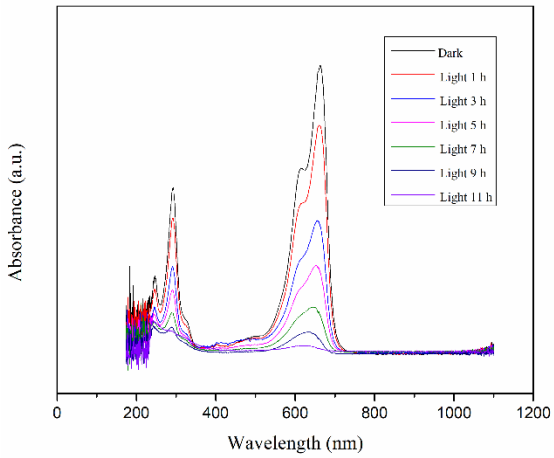

Figure 12. The light absorption of g-C_3N_4

Suan Sunandha Science and Technology Journal
©2022 Faculty of Science and Technology, Suan Sunandha Rajabhat University

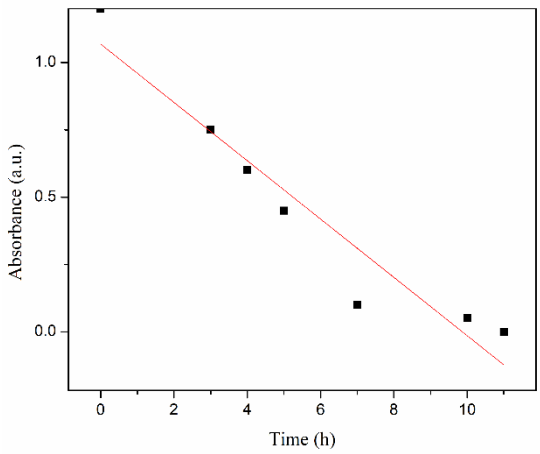

Figure 13. The light absorption at various times of g-C_3N_4

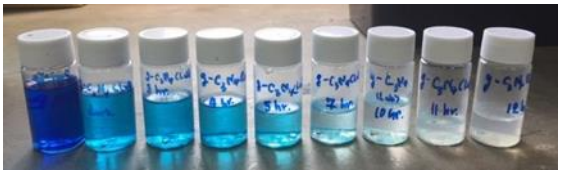

Figure 14. The degradation of MB of g-C_3N_4.

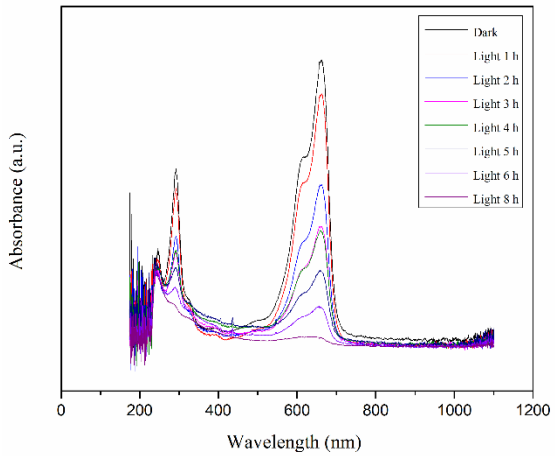

Figure 15. The light absorption of Sn doped g-C_3N_4.

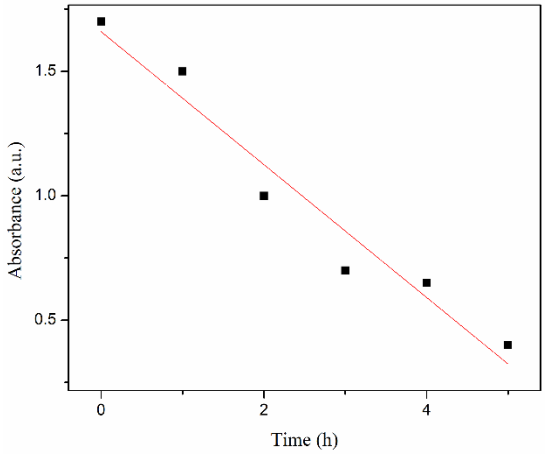

Figure 16. The light absorption at various times of Sn doped g-C_3N_4.

Figure 17. The degradation of MB of Sn doped g-C_3N_4.

4. Conclusions

Sn-modified g-C_3N_4 was synthesized from urea and metallic Sn powder. Firstly, urea was calcined at 450-650°C in the air atmosphere to synthesize g-C_3N_4 powder. Then such g-C_3N_4 powder was mixed with Sn powder for 0.1, 0.3, and 0.5 mole percent and fired at 550°C in ambient. The conclusion could be drawn as follow:

1. Sn was substituted in g-C_3N_4 structure and showed the high absorption of violet-blue and green colors to excite the photocatalytic activity.
2. E_g could obviously be reduced by 0.5 % mol Sn doped g-C_3N_4.
3. E_g down from 2.82 (g-C_3N_4) to 1.98 eV. (0.5 % mol Sn doped g-C_3N_4) which could reflect in the yellow light range.
4. The 0.5 % mol Sn doped g-C_3N_4 could degrade methylene blue faster than g-C_3N_4 about 2.45 times.

Suan Sunandha Science and Technology Journal
©2022 Faculty of Science and Technology, Suan Sunandha Rajabhat University

5. Acknowledgement

This work was partially funded by the National Research Council of Thailand (NRCT), the section of PM 2.5, in the project: Development of silicon carbide air filters from cellulose coated with photocatalyst, 2020.

6. References

Alulema-Pullupaxi, P., Espinoza-Montero, P. J., Sigcha-Pallo, C., Vargas, R., Fernandez, L., Peralta-Hernandez, J. M., & Paz., J. L. (2021). Fundamentals and applications of photoelectrocatalysis as an efficient process to remove pollutants from water: A review. *Chemosphere*, *281*, 130821. doi:10.1016/j.chemosphere.2021.130821

Huang, J., Ho, W., & Wang, X. (2014). Metal-free disinfection effects induced by graphitic carbon nitride polymers under visible light illumination. *Chemical Communications*, *50*(33), 4338-4340. doi:10.1039/C3CC48374F

Kong, X., Liu, X., Zheng, Y., Chu, P. K., Zhang, Y., & Wu, S. (2021). Graphitic carbon nitride-based materials for photocatalytic antibacterial application. *Materials Science and Engineering: R: Reports*, *145*, 100610. doi:10.1016/j.mser.2021.100610

Li, Y., Wu, S., Huang, L., Wang, J., Xu, H., & Li, H. (2014). Synthesis of carbon-doped g-C_3N_4 composites with enhanced visible-light photocatalytic activity. *Materials Letters*, *137*, 281-284. doi:10.1016/j.matlet.2014.08.142

Naseri, A., Samadi, M., Pourjavadi, A., Moshfegh, A. Z., & Ramakrishna, S. (2017). Graphitic carbon nitride (g-C_3N_4)-based photocatalysts for solar hydrogen generation: Recent advances and future development directions. *Journal of Materials Chemistry*, *5*, 23406-23433. doi:10.1039/C7TA05131J

Neelakanta Reddy, I., Veeranjaneya Reddy, L., Jayashree, N., Venkata Reddy, Ch., Cho, M., Kim, D., & Shim, J. (2021). Vanadium-doped graphitic carbon nitride for multifunctional applications: Photoelectrochemical water splitting and antibacterial activities. *Chemosphere*, *264*, 128593. doi:10.1016/j.chemosphere.2020.128593

Shanmugam, V., Muppudathi, A. L., Jayavel, S., & Jeyaperumal, K. S. (2020). Construction of high efficient g-C_3N_4 nanosheets combined with Bi_2MoO_6-Ag photocatalysts for visible-light-driven photocatalytic activity and inactivation of bacterias. *Arabian Journal of Chemistry*, *13*(1), 2439-2455. doi:10.1016/j.arabjc.2018.05.009

Song, Y., Gu, J., Xia, K., Yi, J., Chen, H., She, X., ... Xu, H. (2019). Construction of 2D SnS_2/g-C_3N_4 Z-scheme composite with superior visible-light photocatalytic performance. *Apply Surface Science*, *467-468*, 56-64. doi:10.1016/j.apsusc.2018.10.118

Van, K. N., Huu, H. T., Nguyen Thi, V. N., Le Thi T. L., Truong, D. H., Truong, T. T., ... Vasseghian, Y. (2022). Facile construction of S-scheme SnO_2/g-C_3N_4 photocatalyst for improved photoactivity. *Chemosphere*, *289*, 133120. doi:10.1016/j.chemosphere.2021.133120

Van Viet, P., Nguyen, H.-P., Tran, H.-H., Bui, D.-P., Hai, L. V., Pham, M.-T., ... Thi, C. M. (2021). Constructing g-C_3N_4/SnO_2 S-scheme heterojunctions for efficient photocatalytic NO removal and low NO_2 generation. *Journal of Science: Advanced Materials and Devices*, *6*(4), 551-559. doi:10.1016/j.jsamd.2021.07.005

Wen, J., Xie, J., Chen, X., & Li, X. (2017). A review on g-C_3N_4-based photocatalysts. *Apply Surface Science*, *391*(Pt B), 72-123. doi:10.1016/J.APSUSC.2016.07.030

Zhang, W., Yu, C., Sun, Z., & Zheng, S. (2018). Visible-light-driven catalytic disinfection of Staphylococcus aureus using sandwich structure g-C_3N_4/ZnO/stellerite hybrid photocatalyst. *Journal of Microbiology and Biotechnology*, *28*(6), 957-967. doi:10.4014/jmb.1712.12057

Suan Sunandha Science and Technology Journal
©2022 Faculty of Science and Technology, Suan Sunandha Rajabhat University

Zheng, Y., Liu, J., Liang, J., Jaroniec, M., & Qiao, S. (2012). Graphitic carbon nitride materials: Controllable synthesis and applications in fuel cells and photocatalysis. *Energy & Environmental Science*, *5*(5), 6717-6731. doi:10.1039/C2EE03479D

Available online at http://www.ssstj.sci.ssru.ac.th

Suan Sunandha Science and Technology Journal
©2022 Faculty of Science and Technology, Suan Sunandha Rajabhat University

Utilization of Zinc-doped Nickel Oxide Hole Transporting Materials to Improve Efficiency and Stability of Perovskite Solar Cells

Piyapond Makming[1], Saowalak Homnan[2], Pipat Ruankham[2], Duangmanee Wongratanaphisan[2], Yothin Chimupala[3], Fabrice Goubard[4], Antoine Adjaoud[4], Akarin Intaniwet[1,*]

[1]School of Renewable Energy, Maejo University, San Sai District, Chiang Mai 50290, Thailand
[2]Department of Physics and Materials Science, Faculty of Science, Chiang Mai University, Chiang Mai 50200, Thailand
[3]Department of Industrial Chemistry, Faculty of Science, Chiang Mai University, Chiang Mai 50200, Thailand
[4]Laboratory of Physicochemistry of Polymers and Interfaces, CY Cergy Paris University, Cergy-Pontoise Cedex 95000, France

*Corresponding author e-mail: a.intaniwet@hotmail.co.th

Received: *1 March 2022* / **Revised**: *17 March 2022* / **Accepted**: *14 June 2022*

Abstract

Currently, several techniques have been employed in order to obtain a better quality of perovskite solar cells (PSCs). In this research, we focus on the development of the hole transporting material (HTM) for the efficiency as well as the stability enhancement of the PSCs. Here, a hole transporting layer (HTL) was fabricated using zinc-doped nickel oxide (Zn-doped NiO_x) nanoparticles and the HTL was incorporated into the cesium-formamidinium (CsFA) based PSCs to improve the electrical properties. As a result, PSCs with 1% Zn-doped NiO_x demonstrated the highest power conversion efficiency (PCE) up to 14.72% with an open-circuit voltage (V_{OC}), a short-circuit current density (J_{SC}) and a fill factor of 1.02 V, 19.59 mA/cm^2 and 0.734, respectively. Moreover, the PSCs with Zn-doped NiO_x showed an enhancement in shelf-stability under aging conditions. The physical properties of the Zn-doped NiO_x were analyzed using X-ray photoelectron spectroscopy (XPS) and transmission electron microscopy (TEM). The morphological characteristics of the HTL surface were examined by scanning electron microscopy (SEM) and the photovoltaic properties were analyzed in more detail.

Keywords: Perovskite solar cells, Doping, NiO_x, Zn, Hole transporting layers

1. Introduction

Perovskite solar cells (PSCs) have attracted tremendous attention in the field of energy as an emerging photovoltaic device with a high potential to rival the Si-based solar cells since the power conversion efficiency (PCE) of the PSCs has been sharply increased from 3.8%-25.2% over a short period of time and the device also offers low fabrication cost (Sahoo, Manoharan, & Sivakumar, 2018; Shahiduzzaman et al., 2020; Zhou, Zhou, Tian, Zhu, & Tu, 2018). High PCE can be attributed to the unique optoelectrical properties of the perovskite such as high light absorption ability, low exciton binding energy (Miyata et al., 2015), long carrier diffusion length and lifetime, and power generation stability (Meng, You, & Yang, 2018; Song, Yin, Li, & Li, 2021).

A regular PSC has a device structure of anode/electron transporting layer (ETL)/perovskite/hole transporting layer (HTL)/cathode (Sahoo et al., 2018). The state-of-the-art PSCs mostly require organic HTL such as spiro-OMeTAD (Jeon et al., 2018). Although the air stability of spiro-OMeTAD-based PSCs has been extended up to several hours, the cost of spiro-OMeTAD (500 USD/gm) is extremely high and also the thermal stability and preparation methods remain unsolvable (Serhan et al., 2019). Alternatively, inorganic HTMs such as

Suan Sunandha Science and Technology Journal
©2022 Faculty of Science and Technology, Suan Sunandha Rajabhat University

CuI, pristine- or doped-NiO_x, Cu_2O, CuSCN, $CsSnI_3$, etc., have been employed as the HTL for PSCs (Kim et al., 2020; Yang & Park, 2019; Yin et al., 2016) owing to their low-cost. Interestingly, inorganic HTL materials offer advantages in terms of light and thermal stability, especially moisture stability. Though, crucial contributions are still needed to achieve long-term stability.

This study focuses on the application of zinc-doped nickel oxide (Zn-doped NiO_x) nanoparticles as the HTL to improve the efficiency and the stability of PSCs. Zn-doped NiO_x film was deposited from a colloidal solution of Zn-doped NiO_x nanoparticles in the non-polar isopropanol (IPA) solvent, which will not interact with the perovskite layer. The physical properties of the Zn-doped NiO_x were analyzed using X-ray photoelectron spectroscopy (XPS) and transmission electron microscopy (TEM). The crystal structure was determined using X-ray diffraction (XRD). The morphological characteristics of the HTL surface were examined by scanning electron microscopy (SEM). Finally, the devices were tested under the solar simulator to measure the current density-voltage (J-V) characteristics and the efficiency of the device was determined.

2. Experimental

2.1 NiO_x and NiO_x doped Zn nanoparticles preparation

Zn-doped NiO_x nanoparticles were prepared by a solvothermal method. In the beginning, 0.65 g of nickel acetylacetonate ($Ni(acac)_2$) and $Zn(C_5H_7O_2)_2{\cdot}H_2O$ (1.0 mol%) was added to 70 ml of *tert*-butanal in a conical flask [11]. The mixture was put on a hotplate and stirred at 70°C for 10 h. The resulting turbid green solution was transferred into a Teflon-lined stainless-steel autoclave with 100 ml capacity. Then the sample was kept in an oven at 210°C for 24 h. After cooling to room temperature, the resulting NiO_x colloidal solution was centrifuged. The precipitate was washed with absolute ethanol two times. Then, the NiO_x nanoparticles were dried at 75°C for 2 h in an oven. Finally, the NiO_x nanoparticles were sintered at 300°C for 2 h. It is noted that all processes were conducted in ambient air conditions.

2.2. Fabrication of perovskite solar cells

FTO-coated glass substrates were cleaned sequentially with Alconox, de-ionized (DI) water, acetone, and isopropanol using the ultrasonic sonicator for 30 min. Then, the FTO substrates were treated with UV-ozone for 15 min. An electron-transporting zinc-tin oxide (ZTO) layer was deposited by spin-coating a 0.3M solution of zinc acetate dihydrate and tin (II) 2-ethylhexanoate with equivalent molar of ethanolamine in 2-methoxyethanol onto the cleaned FTO-coated glass at 3000 rpm for 30 s. The as-deposited film was then annealed on a hotplate in the ambient atmosphere for 1 h at 450°C (Zhao et al., 2012). Next, the substrates were cooled to room temperature, and the ZTO films were treated with UV-O_3 to clean the surface.

A $Cs_{0.17}FA_{0.83}Pb(I_{0.83}Br_{0.17})_3$ or CsFA perovskite solution was prepared with the procedure reported in the literature (Schutt et al., 2019). The CsFA film was deposited via a two-step spin-coating process at 1000 rpm and 6000 rpm for 10 s and 20 s, respectively. During the second step, 120 µL of anisole was dripped on the spinning substrate 10 s before the end of the procedure. The samples were then annealed on a hotplate at 100°C for 15 min and were thermalized to room temperature. Subsequently, 60 µL of Zn-doped NiO_X nanoparticles solution (5 mg mL^{-1} in absolute isopropanol) was spin-coated at 3000 rpm for 30 s onto the CsFA perovskite layer and then 60 µL of CuSCN solution (35 mg mL^{-1} in diethyl sulfide) was coated at 2500 rpm for 30 s (Er, Icli, & Ozenbas, 2020; Zhao et al., 2012) to complete the HTL layer. Finally, the carbon electrode sheet was prepared by the ethanol solvent interacting process for 2 h, and then it was hot-pressed onto the CuSCN layer at 50°C for 3 min with pressure of 6 MPa (Passatorntaschakorn et al., 2021; Zhang et al., 2018) to finish the device. The other two PSCs were made to compare the result of different HTL compositions where only CuSCN and NiOx/CuSCN with similar coating conditions were used as the HTL.

2.3. Characterization

Elemental characterization was carried out for the NiO_x, NiO_x-Zn1% films using X-ray Photoelectron Spectroscopy (XPS) analysis and transmission electron microscopy (TEM) was used to observe the morphology. Moreover, the morphological characteristics of the HTL surface were examined by scanning electron microscopy

Suan Sunandha Science and Technology Journal
©2022 Faculty of Science and Technology, Suan Sunandha Rajabhat University

(SEM) on JEOL JSM-IT800. Current density-voltage (J-V) characteristics of PSCs were obtained from parameter analyzer (X200 source meter, Ossila) under AM 1.5 G (100 mW cm^{-2}) solar simulator. External quantum efficiency (EQE) spectra were measured using the QE-R quantum efficiency system (Enlitech) in a DC mode. The system was calibrated using a Si photodiode prior to the measurement. Electrochemical impedance spectra (EIS) were recorded using Auto lab PGSTAT 302 N and the equivalent circuit was used to fit the experimental data to extract the EIS parameters.

3. Results and Discussion

3.1 Physical properties

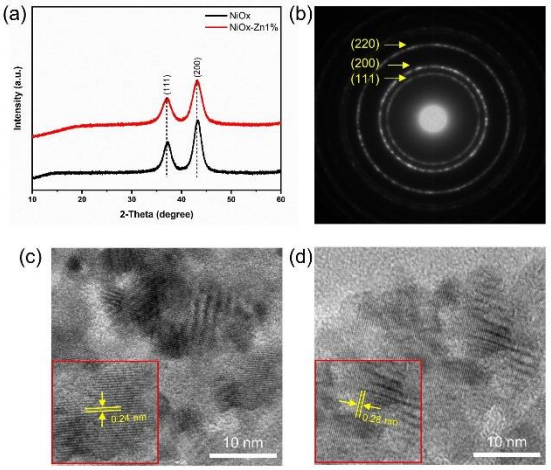

Figure 1. (a) XRD patterns of the as-synthesized NiO_x and NiO_x-Zn1%, (b) SAED pattern, TEM micrographs of (c) NiO_x and (d) NiO_x-Zn1% nanoparticles.

Figure 1a shows the XRD pattern of the as-synthesized NiO_x and NiO_x-Zn1% nanoparticles. It can be seen that two main NiO_x peaks at 37.24, and 43.4°, which refer to planes (1 1 1), and (2 2 0), and two main NiOx-Zn1% peaks at 37.01, and 43.19°, which refer to planes (1 1 1), and (2 2 0), are observed and the existence of the cubic bunsenite NiO_x phase is confirmed. Furthermore, X-ray diffraction results also indicate the presence of Zn in NiO_x since the peak of NiO_x-Zn1% is slightly shifted to the left. That means Zn can successfully be incorporated into the NiO_x nanoparticles without changing their structure (Mahmud Hasan et al., 2020; Xie et al., 2018). Selected-area electron diffraction (SAED) pattern and high-resolution TEM images of NiO_x and NiO_x-Zn1% are shown in Figure. 1b-d. The results demonstrate that NiO_x and NiO_x-Zn1% show a cubic crystalline structure with the distance between two successive bright fringes of 0.24 and 0.28 nm, respectively, which corresponds to the (111) plane of NiO_x (Nam et al., 2019).

Additionally, X-ray photoelectron spectroscopy (XPS) measurements were used to verify the doping result from the chemical composition of Zn-doped NiO_X films. Figure 2a shows the elemental composition and the survey XPS spectra of the films. It is noted that O and C elements are observed in every sample. The Zn element, on the other hand, is not detected in the film since only a small fraction of Zn (1%) was doped into the sample. Figure 2b exhibits the XPS spectrum of the Ni 2p peak in an undoped and doped Zn. The spectrum can be de-convoluted into six distinct peaks; 853.5, 854.8, 855.8, 871.1, 872.1, and 873.2 eV respectively (Chakrabarti et al., 2019), which indicate a normal state of Ni^{2+}. Figure. 2c shows the characteristic C 1s peak from the carbon film. All samples show four peak components centered at 284.4, 285.2, 286.7, and 288.6 eV, which correspond to the Ni–O, the interstitial Ni, C–C and C–H of acac ligand of residues of $Ni(acac)_2$ precursor, respectively. Furthermore, C–OH/C–O–C (286.7 eV) (Koshtyal et al., 2019) is slightly seen. Figure 2d shows the XPS spectrum for O 1s where four peaks can be de-convoluted from the spectrum centered at 529.0, 530.6, 532.6, and 531.8 eV respectively. The peak centered at 529.0 eV can be assigned to Ni-O octahedral bonding in NiO and the peak centered at 532.6 eV is likely due to the presence of nickel hydroxides or the surface adsorbed hydroxyl groups (Ratcliff et al., 2011).

Suan Sunandha Science and Technology Journal
©2022 Faculty of Science and Technology, Suan Sunandha Rajabhat University

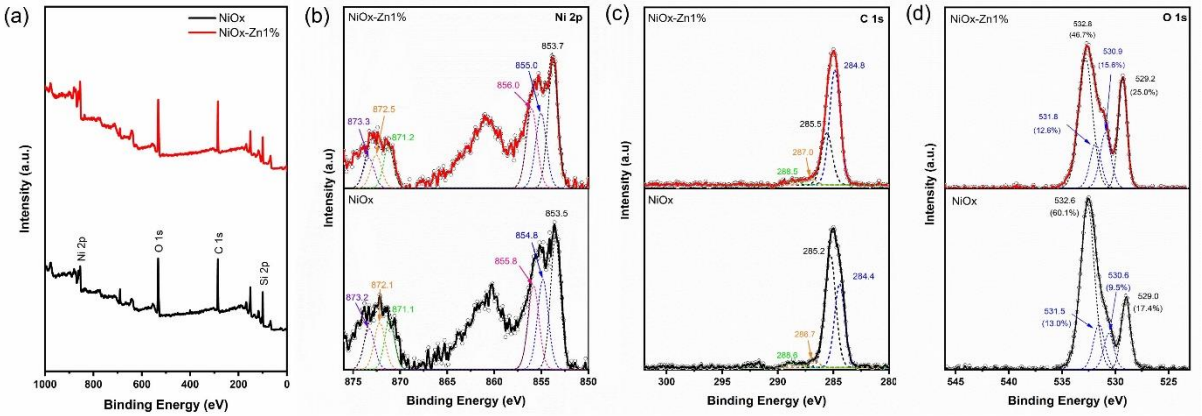

Figure 2. Compositional analysis of NiO_x and NiO_x-Zn1% nanoparticles. (a) Survey XPS spectra, and high-resolution XPS peaks of (b) Ni 2p, (c) C 1s, and (d) O 1s.

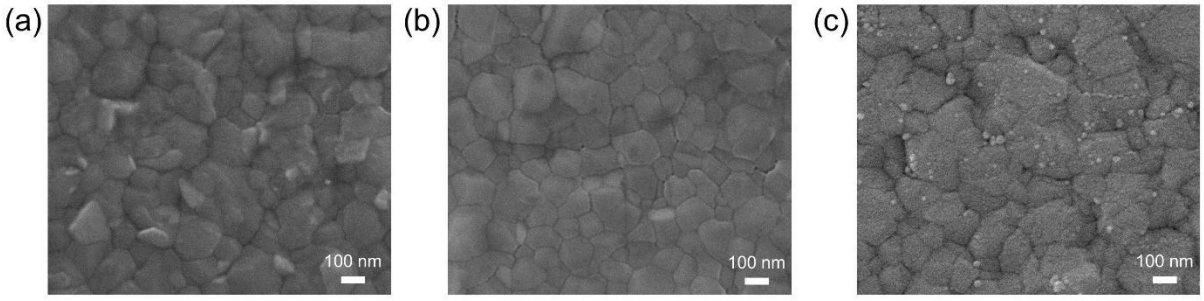

Figure 3. Top view SEM micrograph of (a) reference (CuSCN HTL) cell, (b) NiO_x/CuSCN HTL cell, and (c) NiO_x-Zn1%/CuSCN HTL cell.

Top view SEM surface morphology of different HTLs coated on perovskite layers presented in Figure 3a-c. The reference cell (Figure 3a), where only CuSCN was used for HTL, showed a rough and unsmooth surface with possible existence of pinholes. The NiO_x/CuSCN HTL (Figure 3b), on the other hand, provided a rather smooth surface layer with less grain boundary. Figure 3c shows the NiO_x-Zn1% film on a perovskite substrate. It can be seen that the surface layer was well covered, and the pinholes disappeared. The tiny white granule in the figure could be attributed to NiO_x-Zn1

Suan Sunandha Science and Technology Journal
©2022 Faculty of Science and Technology, Suan Sunandha Rajabhat University

3.2 Electrical properties

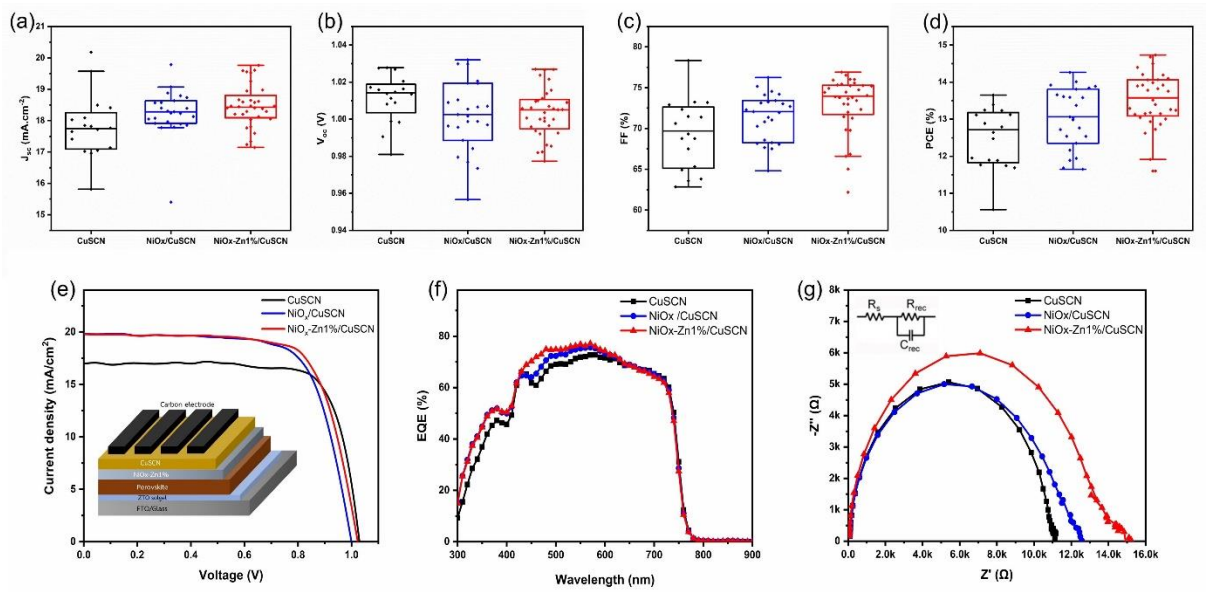

Figure 4. Box plots of photovoltaic parameters; (a) J_{SC}, (b) V_{OC}, (c) FF, and (d) PCE of PSCs fabricated based on conventional CuSCN, NiO_x/CuSCN and NiO_x-Zn1%/CuSCN HTLs; (e) J-V characteristics of the champion devices; (f) EQE curves of PSCs; (g) Nyquist plots under the forward bias of 0.85 V.

The photovoltaic parameters of the PSCs based on FTO/ZTO sol-gel/$Cs_{0.17}FA_{0.83}Pb(I_{0.83}Br_{0.17})_3$/$NiO_x$, NiO_x-Zn1%/CuSCN/carbon are displayed in Figure. 4(a-d) and in Table 1. The J-V curves of the champion PSCs are shown in Figure. 4e. The device with NiO_x-Zn1%/CuSCN film as HTL exhibited the best performance with the PCE values of 14.72%, short circuit current density (J_{sc}) of 19.59 mA /cm^2, open-circuit voltage (V_{oc}) of 1.02 V, and fill factor (FF) of 0.734 while the device with CuSCN, and NiO_x/CuSCN exhibited the maximum PCE values of 13.65%, and 14.26%, respectively. The PCE of the device with CuSCN as HTL was relatively low compared to other devices because there were still holes and uneven surface area, resulting in insufficient charge transport. However, with the addition of a Zn-doped NiO_x layer, the quality of the film seems to be improved and hence a higher conversion efficiency is acquired. Although, the maximum FF of 0.783, which was obtained from one time measurement from CuSCN device, is slightly higher than that of the champion NiO_x-Zn1%/CuSCN device (0.734) but the average photovoltaic parameters, as demonstrated in Table 1 in brackets, reveals that the device with Zn-doped NiO_x device offers the highest values. Figure 4f exhibits the EQE spectra obtained from devices. The EQE spectra show approximately 0.727, 0.757, and 0.771 respectively in the wavelength range of 500–800 nm. This results in a high J_{sc} which is in good agreement with the values obtained from the J–V measurement.

The electrochemical impedance spectroscopy (EIS) spectra was employed to further investigate the reason behind the photovoltaic parameter variation of the PSCs based on CuSCN, NiO_x/CuSCN, and NiO_x-Zn1%/CuSCN films. The Nyquist plots of the experimental data (Figure. 4g) were fitted using an equivalent circuit (inset of Figure. 4g) and EIS parameters, including series resistance (R_s), recombination resistance (R_{rec}), and chemical capacitance (C_{rec}). It was found that the R_{rec} of the PSCs based on NiO_x-Zn1%/CuSCN film (15.21 kΩ) was higher than both the PSCs based on CuSCN film (11.12 kΩ), and the PSCs based on NiO_x/CuSCN film (12.56 kΩ). Improving the interfacial region in the NiO_x-Zn1%/CuSCN device was probably the reason for the better photovoltaic parameters.

Suan Sunandha Science and Technology Journal
©2022 Faculty of Science and Technology, Suan Sunandha Rajabhat University

Table 1. Photovoltaic parameters of PSCs fabricated from CuSCN, NiO_x/CuSCN and NiO_x-Zn1%/CuSCN HTLs.

HTL	J_{sc} (mA/cm^2)	V_{oc} (V)	FF (%)	PCE (%)
CuSCN	16.95	1.027	78.33	13.65
	(17.82 ± 1.04)	(1.011 ± 0.013)	(69.31 ± 4.38)	(12.47 ± 0.84)
NiO_x/CuSCN	19.78	0.996	72.3	14.26
	(18.23 ± 0.78)	(1.001 ± 0.019)	(71.35 ± 2.96)	(13.03 ± 0.67)
NiO_x-Zn1%/CuSCN	19.59	1.023	73.42	14.72
	(18.46 ± 0.68)	(1.003 ± 0.013)	(72.96 ± 3.53)	(13.51 ± 0.74)

J_{sc}: short circuit current density, V_{oc}: open-circuit voltage, FF: fill factor, PCE: power conversion efficiency

The unencapsulated PSCs with the use of the CuSCN, NiO_x/CuSCN, and NiO_x-Zn1%/CuSCN HTL were tested in terms of shelf stability by measuring their photovoltaic properties of the devices stored in a desiccator with controlled environment (relative humidity of 40-50% and temperature of 25-30°C). As shown in Figure 5a and b, the PSC with the CuSCN HTL exhibits greater efficiency degradation when compared to the devices with NiO_x/CuSCN, and NiO_x-Zn1%/CuSCN HTLs. We note that there was a small increase of the PCE during the first few days of storing. We speculate that the surface stoichiometry of NiO_x might be modified by oxygen molecules in the air. This modification could facilitate the hole transport and extraction ability (Cao et al., 2017). In contrast, the efficiency of the PSCs with NiO_x/CuSCN or the NiO_x-Zn1%/CuSCN HTL decreased to less than 80% or 75% of its initial values after storing for 90 days (Figure. 5b). Although the slightly greater efficiency degradation was observed for the PSCs with NiO_x-Zn1%/CuSCN HTL when compared to the device without Zn doping. The actual average cell efficiency of NiO_x-Zn1%/CuSCN devices was comparable to that of the NiO_x/CuSCN devices. A reason behind this slightly larger efficiency degradation is still unclear. The investigation will be further performed. However, it can imply from the obtained results that the insertion of NiO_x or NiO_x-Zn1% nanoparticles between the perovskite layer and the CuSCN layer could significantly improve the shelf stability.

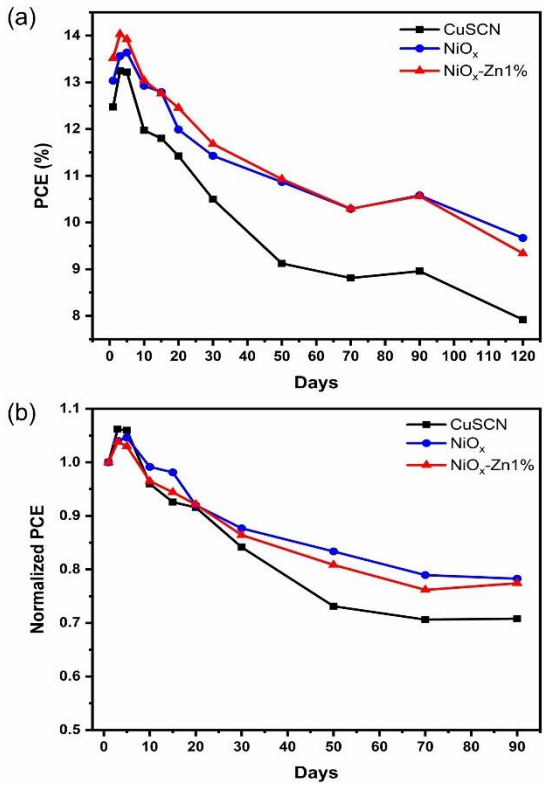

Figure 5. (a) Average PCE and (b) normalized PCE as a function of storage time for CuSCN-, NiO_x/CuSCN- and NiO_x-Zn1%/CuSCN-coated PSCs without encapsulation.

4. Conclusions

In conclusion, we have demonstrated that the Zn-doped NiO_x/CuSCN double inorganic material might be a promising material for holes extraction layer. PSC using Zn-doped NiO_x HTL reached a maximum PCE of 14.72%. The developed Zn-doped NiO_x non-polar interfacial layer could protect the perovskite layer during CuSCN deposition from the polar solvent. The air stability of the device under the ambient condition could be extended for more than 3 months with the efficiency

Suan Sunandha Science and Technology Journal
©2022 Faculty of Science and Technology, Suan Sunandha Rajabhat University

reduction of about 25%. The present study offers the alternative approach towards the development of highly air thermal stable, additive-free, low-cost based in real, cost-effective perovskite solar cells.

5. Acknowledgements

This work was financially supported by Maejo University and Chiang Mai University. The authors would like to thank the School of Renewable Energy, Maejo University, for the scholarship support and research grants for researchers.

6. References

Cao, J., Yu, H., Zhou, S., Qin, M., Lau, T. K., Lu, X., ... Wong, C. P. (2017). Low-temperature solution-processed NiO_X films for air-stable perovskite solar cells. *Journal of Materials Chemistry A*, *5*(22), 11071-11077. doi:10.1039/c7ta02228j

Chakrabarti, S., Carolan, D., Alessi, B., Maguire, P., Svrcek, V., & Mariotti, D. (2019). Microplasma-synthesized ultra-small NiO nanocrystals, a ubiquitous hole transport material. *Nanoscale Advances*, *1*, 4915-4925. doi:10.1039/c9na00299e

Er, U., Icli, K. C., & Ozenbas, M. (2020). Spin-coated copper(I) thiocyanate as a hole transport layer for perovskite solar cells. *Journal of Solid State Electrochemistry*, *24*, 293-304. doi:10.1007/s10008-019-04430-2

Jeon, N. J., Na, H., Jung, E. H., Yang, T. Y. Lee, Y. G., Kim, G., ... Seo, J. (2018). A fluorene-terminated hole-transporting material for highly efficient and stable perovskite solar cells. *Nature Energy*, *3*, 682-689. doi:10.1038/s41560-018-0200-6

Kim, J., Lee, Y., Gil, B., Yun, A. J., Kim, J., Woo, H., ... Park, B. (2020). A Cu_2O-CuSCN nanocomposite as a hole-transport material of perovskite solar cells for enhanced carrier transport and suppressed interfacial degradation. *ACS Applied Energy Materials*, *3*, 7572-7579. doi:10.1021/acsaem.0c01001

Koshtyal, Y., Nazarov, D., Ezhov, I., Mitrofanov, I., Kim, A., Rymyantsev, A., ... Maximov, M. (2019). Atomic layer deposition of NiO to produce active material for thin-film lithium-ion batteries. *Coatings*, *9*(5), 301. doi:10.3390/coatings9050301

Mahmud Hasan, A. K., Raifuku, I., Amin, N., Ishikawa, Y., Sarkar, D. K., Sobayel, K., ... Akhtaruzzaman, M. (2020). Air-stable perovskite photovoltaic cells with low temperature deposited NiOx as an efficient hole-transporting material. *Optical Materials Express*, *10*(8), 1801-1816. doi:10.1364/ome.391321

Meng, L., You, J., & Yang, Y. (2018). Addressing the stability issue of perovskite solar cells for commercial applications. *Nature Communications*, *9*, 5265. doi:10.1038/s41467-018-07255-1

Miyata, A., Mitioglu, A., Plochocka, P., Portugall, O., Wang, J. T. W., Stranks, S. D., ... Nicholas, R. J. (2015). Direct measurement of the exciton binding energy and effective masses for charge carriers in organic-inorganic tri-halide perovskites. *Nature Physics*, *11*, 582-587. doi:10.1038/nphys3357

Nam, V. B., Shin, J., Yoon, Y., Giang, T. T., Kwon, J., Suh, Y. D., ...Lee, D. (2019). Highly stable Ni-based flexible transparent conducting panels fabricated by laser digital patterning. *Advanced Functional Materials*, *29*(8), 1806895. doi:10.1002/adfm.201806895

Passatorntaschakorn, W., Bhoomanee, C., Ruankham, P., Gardchareon, A., Songsiriritthigul, P., & Wongratanaphisan, D. (2021). Room-temperature carbon electrodes with ethanol solvent interlacing process for efficient and stable planar hybrid perovskite solar cells. *Energy Reports*, *7*, 2493-2500. doi:10.1016/j.egyr.2021.04.031

Ratcliff, E. L., Meyer, J., Steirer, K. X., Garcia, A., Berry, J. J., Ginley, D. S., ... Armstrong, N. R. (2011). Evidence for near-surface NiOOH

Suan Sunandha Science and Technology Journal
©2022 Faculty of Science and Technology, Suan Sunandha Rajabhat University

species in solution-processed NiO_x selective interlayer materials: Impact on energetics and the performance of polymer bulk heterojunction photovoltaics. *Chemistry of Materials*, *23*, 4988-5000. doi:10.1021/cm202296p

Sahoo, S. K., Manoharan, B., & Sivakumar, N. (2018). Introduction: Why perovskite and perovskite solar cells? In S. Thomas, & A. Thankappan (Eds.), *Perovskite photovoltaics* (pp. 1-24). Academic Press. doi:10.1016/B978-0-12-812915-9.00001-0

Schutt, K., Nayak, P. K., Ramadan, A. J., Wenger, B., Lin, Y. H., & Snaith, H. J. (2019). Overcoming zinc oxide interface instability with a methylammonium-free perovskite for high-performance solar cells. *Advanced Functional Materials*, *29*(47), 1900466. doi:10.1002/adfm.201900466

Serhan, M., Sprowls, M., Jackemeyer, D., Long, M., Perez, I. D., Maret, W., ... Forzani, E. (2019). Total iron measurement in human serum with a smartphone. *AIChE Annual Meeting, Conference Proceedings*, *2019*. doi:10.1039/x0xx00000x

Shahiduzzaman, M., Fukaya, S., Muslih, E. Y., Wang, L., Nakano, M., Akhtaruzzaman, M., ... Taima, T. (2020). Metal oxide compact electron transport layer modification for efficient and stable perovskite solar cells. *Materials*, *13*(9), 2207. doi:10.3390/ma13092207

Song, J. X., Yin, X. X., Li, Z. F., & Li, Y. W. (2021). Low-temperature-processed metal oxide electron transport layers for efficient planar perovskite solar cells. *Rare Metals*, *40*, 2730-2746. doi:10.1007/s12598-020-01676-y

Xie, X., Gao, C., Du, X., Zhu, G., Xie, W., Liu, P., & Tang, Z. (2018). Improved optical and electrochromic properties of NiO_x films by low-temperature spin-coating method based on NiO_x nanoparticles. *Materials*, *11*(5), 760. doi:10.3390/ma11050760

Yang, G., & Park, S. J. (2019). Conventional and microwave hydrothermal synthesis and application of functional materials: A review. *Materials*, *12*(7), 1177. doi:10.3390/ma12071177

Yin, X., Liu, J., Ma, J., Zhang, C., Chen, P., Que, M., ... Shao, J. (2016). Solvothermal derived crystalline NiO_x nanoparticles for high performance perovskite solar cells. *Journal of Power Sources*, *329*, 398-405. doi:10.1016/j.jpowsour.2016.08.102

Zhang, H., Xiao, J., Shi, J., Su, H., Luo, Y., Li, D., ... Meng, Q. (2018). Self-adhesive macroporous carbon electrodes for efficient and stable perovskite solar cells. *Advanced Functional Materials*, *28*(39), 1802985. doi:10.1002/adfm.201802985

Zhao, Y., Dong, G., Duan, L., Qiao, J., Zhang, D., Wang, L., & Qiu, Y. (2012). Impacts of Sn precursors on solution-processed amorphous zinc-tin oxide films and their transistors. *RSC Advances*, *2*, 5307-5313. doi:10.1039/c2ra00764a

Zhou, D., Zhou, T., Tian, Y., Zhu, X., & Tu, Y. (2018). Perovskite-based solar cells: Materials, methods, and future perspectives. *Journal of Nanomaterials*, *2018*, 1-15. doi:10.1155/2018/8148072

Available online at http://www.ssstj.sci.ssru.ac.th

Suan Sunandha Science and Technology Journal
©2022 Faculty of Science and Technology, Suan Sunandha Rajabhat University

Sound Absorbing Panels from Poly(lactic acid) Non-woven Fabric and Natural Fibers

Mathurot Malimat[1], Nanjaporn Roungpaisan[2], Weraporn Pivsa-Art[3], Sommai Pivsa-Art[1]*

[1]Department of Materials and Metallurgical Engineering, Faculty of Engineering, Rajamangala University of Technology Thanyaburi, Pathum Thani 12110, Thailand

[2]Department of Textile Engineering, Faculty of Engineering, Rajamangala University of Technology Thanyaburi, Pathum Thani 12110, Thailand

[3]Department of Chemical and Materials Engineering, Faculty of Engineering, Rajamangala University of Technology Thanyaburi, Pathum Thani 12110, Thailand

***Corresponding author e-mail: sommai.p@en.rmutt.ac.th**

Received: *3 February 2022* / **Revised**: *30 March 2022* / **Accepted:** *17 June 2022*

Abstract

This research studied the utilization of biodegradable polymer for nonwoven fabric production and applied to fabricate a sound absorbing panel by corporate with natural fiber nonwoven fabric. PLA was used as a biodegradable polymer and hemp nonwoven was used as a natural fiber nonwoven fabric. PLA nonwoven fabric was prepared using a melt jet spinning process. The spinning process was carried out at 250 and 260°C with screw speed of 10 rpm and air blown pressure of 0.3 and 0.5 MPa. The die-to-collector of fabric production was studied at 30 and 60 cm to compare the nonwoven fabric product property. It was found that the process temperature, air pressure and die-to-collector distance have significant effects on the nonwoven fabric thickness, GSM, and fabric density. Air permeability decreased with high fabric thickness as well as fine fibers which supported the property of sound absorbing panels. Therefore, the suitable conditions for sound absorbing panel fabrication were processed at temperature of 260°C, air pressure 0.5 MPa and die-to-collector distance of 60 cm. Sound absorbing coefficient measurement revealed that GSM fabric thickness had an effect on increasing sound absorption. The effect of nonwoven sheet order and arrangement of PLA nonwoven and hemp nonwoven of 3 layers sandwich indicated that the layers order of PLA/PLA/Hemp had high sound absorbing coefficient that was comparable with PLA/PLA/PLA due to fiber size and arrangement.

Keywords: Sound absorbing panel, Poly(lactic acid), Nonwoven, Hemp fiber

1. Introduction

The environmental concern on pollution from plastic waste has a high impact on the utilization of bioplastics to replace the conventional petroleum-based materials. In the automotive industry, the effects of an increase in greenhouse gas emissions and a greater focus on environmental sustainability and vehicle end life management, have all contributed to this trend. Bioplastics are one of the best replacement materials for conventional plastics as well as metals (PricewaterhouseCoopers, 2007).

Noise is a major cause of industrial fatigue, irritation, and one of the major causes in reducing the productivity of industrial processing and one source of occupational accidents. It has been reported that continuous exposure of noise of 90dB or above is dangerous to hearing (Devi, 2014). Various kinds of acoustic materials have been used as either sound barriers or sound absorbers to reduce noise or sound in vehicles to a comfort level or silence. Solid and impermeable materials were used as a sound barrier which reflects the incoming sound in order to prevent sound transmission. On the other hand, porous materials, including foams and fibrous materials with internal pores, were effectively used as sound absorbers, especially in a high frequency range (Prahsarn, Klinsukhon, Suwannamek, Wannid, & Padee, 2020; Sengupta, 2010). Porous sound absorbing materials have been widely used in the construction of aircraft, spacecraft, cars, trucks, and ships (Chavan & Manik, 2008).

Nonwovens are fibrous materials assembled directly from fibers having high porous structures and high surface areas. From these properties

Suan Sunandha Science and Technology Journal
©2022 Faculty of Science and Technology, Suan Sunandha Rajabhat University

nonwovens are attractive for being used as sound absorbers for many technical applications. When the sound wave enters nonwoven, it moves through tortuous passages and contacts with the fiber surface, resulting in energy dissipation into heat loss (Benkreira, Khan, & Horoshenkov, 2011; Tascan & Vaughn, 2008; Zhu, Nandikolla, & George, 2015). Nonwovens offer advantages over foams as they can be recycled, and their manufacturing methods may have less environmental impact than conventional polyurethane sound absorbers. Compared with foams, nonwovens can absorb more sound over a wider range of frequencies (Yilmaz, Banks-Lee, Powell, & Michielsen, 2011).

Glass fibers have been used for sound absorbing material from their sound absorption characteristics and air flow resistivity among fibrous absorbers (Yilmaz, 2009). However, due to the potential risks posed by glass fibers such as being unsafe to handle, non-recyclable, and posing health risks when inhaled, natural fibers are increasingly gaining attention in diversified engineering end uses in place of glass fibers. The application of natural fibers and biodegradable polymer fibers for sound absorbing panels have been constantly studied (Korte & Staiger, 2008; Oh, Kim, & Kim, 2009). The effect of combination of natural fiber and nonwoven fabric on sound absorption proficiency has not been reported.

In this study, sound absorption of three-layered nonwoven consisting of single and multiple types of fibers were reported. The fiber layers consist of poly(lactic acid) (PLA) nonwoven panel and hemp fibers. The effect of processing conditions of PLA nonwoven fabric property and sequencing of the constituent layers on sound absorption were investigated.

2. Materials and Method

2.1 Materials

Poly(lactic acid) pellets are of Ingeo biopolymer 6100D, with a melt flow index of 24 g/10 min (210°C) and density of 1.24 g/cm^3 (Nature Works LLC). Hemp used in this research was obtained from Hempthai Co. Ltd. (Tak province, Thailand).

2.2 Sample preparation

PLA was dried in the oven at 80°C for 12 h. PLA nonwoven was fabricated by a melt jet spinning machine outfitted with a die with three 0.4 mm spinnerets and a hot air outlet at the center. PLA pellets were fed into the hopper and molten by the extruder process. The screw speed was set at 10 rpm. The nozzle has three holes of spinnerets with a diameter of 0.4 mm that are located above the hot air outlet. The nozzle temperatures were varied for 250 and 260°C. The air pressures were controlled from 0.3 and 0.5 MPa by the air pressure controller. The collector distance between the nozzle and the collector, which is referred to as the collector, was varied at 30 and 60 cm. The molten PLA was blown and stretched by the hot air flow. PLA nonwoven materials were collected on a roller mesh collector at different processing conditions. Three layers of webs from PLA and hemp nonwoven were stacked as given in Table 1 (Figure 1).

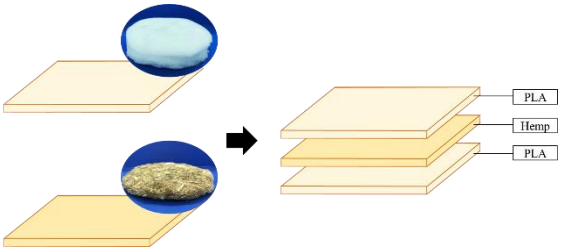

Figure 1. Schematic of multilayer structure of fiber webs.

Table 1. Layering of fiber webs.

Web number	Web code	Layer 1 (A)	Layer 2 (B)	Layer 3 (C)
1	HHH	Hemp	Hemp	Hemp
2	HLL	Hemp	PLA	PLA
3	LHL	PLA	Hemp	PLA
4	LLH	PLA	PLA	Hemp
5	LLL	PLA	PLA	PLA
6	LHH	PLA	Hemp	Hemp
7	HLH	Hemp	PLA	Hemp
8	HHL	Hemp	Hemp	PLA

Note: H = hemp, L = PLA

2.3 Thickness and mass per unit area (grams per square meter, GSM)

Mass per unit area of fabric sample of 1 cm x 10 cm for 10 pieces (g/m^2) were cut randomly and weighed in grams. The thickness of the fabric is ten measurements taken from each sample using a thickness gauge (Telclock Dial thickness gauge SM

Suan Sunandha Science and Technology Journal
©2022 Faculty of Science and Technology, Suan Sunandha Rajabhat University

112P).

2.4 Morphology and fiber diameter evaluation

Morphology of PLA fiber and hemp fiber was observed by optical microscopy technique (OM) (Olympus Microscope, CX41) beamed at 10 times magnification. Fiber diameters were examined from OM photographs using Image J software.

2.5 Air permeability

The fabric transport property that is most sensitive to fabric structure is air permeability, defined as the volume flow rate per unit area of a fabric when there is a specified pressure differential across two faces of the fabric. Air permeability of the samples were measured based on ASTM D737 Standard Test Method for Air Permeability of Textile Fabrics. The measurements were performed at a constant pressure drop of 100 Pa (20 cm^2 test area).

2.6 Sound absorption coefficients

Sound absorption coefficient was measured according to ASTM E 1050-08 standard test method by using an acoustic duct (SCIEN-9301, Korea) two microphones. Samples were cut into two different sizes (30 and 100 mm). The 30 mm tube was used to test the sound absorption coefficient at a (low) frequency between 125 to 1600 Hz. The sound absorption coefficient at a (high) frequency from 500 to 6300 Hz was tested using the 100 mm tube. The calibration was performed before conducting the test. Samples were mounted into the sample holder, which was clamped onto the tube for testing. For each material, three samples were tested in each tube size to cover the whole frequency range between 125 and 6300 Hz. The noise reduction coefficient (NRC) of all the materials were calculated according to Equation (1) (Mohammad, Nik Syukri, & Nuawi, 2019).

$$NRC = \frac{\alpha 250Hz + \alpha 500Hz + \alpha 1000Hz + \alpha 2000Hz}{4} \quad (1)$$

3. Results and Discussion

3.1 GSM and thickness of PLA nonwoven fabric

The effect of GSM and thickness on property PLA nonwoven fabric is shown in Figure 2 (a) and (b). The fiber was produced using air pressure of 0.3 and 0.5 MPa and die-to-collector distance of 30 and 60 cm. The die temperature was controlled for 250 and 260°C. Increasing die temperature resulted in high melting of polymer, and increasing in air pressure, and collector distance evolved significantly in GSM and fabric thickness. Numerous studies that dealt with sound absorption in porous materials have concluded that low frequency sound absorption has a direct relationship with thickness (Coates & Kierzkowski, 2002). It was observed that the samples with higher GSM showed higher thickness. It was reported that thicker materials showed better sound absorption values (Devi, 2014). The fabric GSM showed highest thickness (Figure 2) at temperature 260°C, air pressure 0.5 MPa and die-to-collector distance of 60 cm.

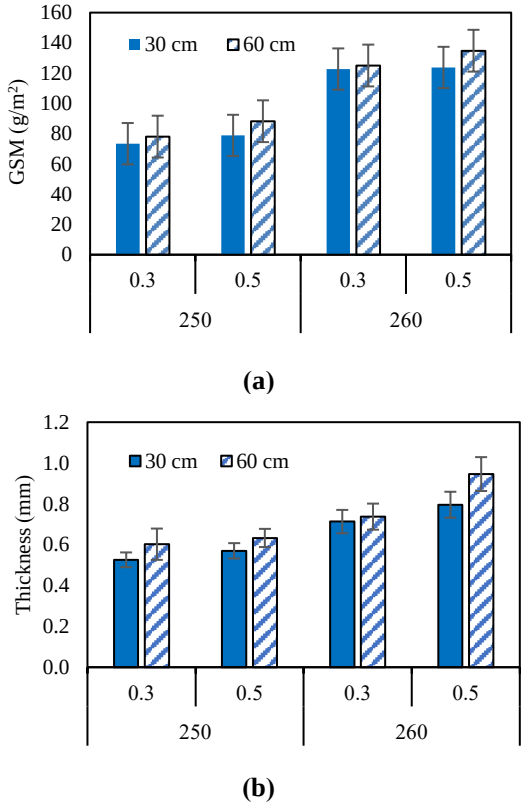

Figure 2. GSM and thickness of PLA nonwoven fabric (Nozzle temperature 250 and 260°C, air pressure 0.3 and 0.5 MPa, collector distance 30 and 60 cm) (a) GSM, (b) thickness.

3.2 Density of PLA nonwoven fabric

The material density is another factor to characterize the nonwoven fabric and is defined as mass per unit volume (g/cm^3). Density influences the acoustic impedance as the impedance determines the reflection of materials. It was reported that noise reduction coefficient increases with decrease in density (Wertel, 2000). In Table 2, increasing die temperature resulted in increasing of the nonwoven fabric density due to the thickness of material (Al-Shammari, Al-Fariss, Al-Sewailm, & Elleithy, 2011). However, with increasing air pressure and collector distance, the density of the nonwoven

Suan Sunandha Science and Technology Journal
©2022 Faculty of Science and Technology, Suan Sunandha Rajabhat University

fabric decreases. Therefore, the process at 0.5 MPa and die-to-collector distance of 60 cm was the most suitable condition for production of sound absorption panels.

Table 2. Density of PLA nonwoven fiber.

Temperature (°C)	Air pressure (MPa)	Collector distance (Cm)	Density (g/cm^3)
250	0.3	30	0.146 ± 0.007
		60	0.130 ± 0.009
	0.5	30	0.139 ± 0.011
		60	0.140 ± 0.008
260	0.3	30	0.176 ± 0.012
		60	0.169 ± 0.017
	0.5	30	0.155 ± 0.009
		60	0.141 ± 0.010

3.3 Morphology and fiber diameter of PLA nonwoven fabric

Figures 3 and 4 present the OM photograph and the distribution of the PLA fibers at 250 and 260°C, pressure of 0.3 and 0.5 MPa and collected at 30 and 60 cm. In Figure 3, the PLA fibers at 250°C are large with near die-to-collector distance while the fiber diameter decreases with long collected distance. The fiber sizes and the distributions were significantly decreased when increasing air pressures and collector distance. In Figure 4 the fibers size and fiber distribution of the nozzle temperatures at 260°C showed similar tendency with 250ºC. The PLA fibers size distribution at 260°C with air pressure of 0.5 MPa, 60 cm were smaller than the process at 250°C.

It could be considered that the molten PLA at 250°C was faster solidified than at 260°C which would result in large fiber size. Finer fibers were produced at higher air velocity and collector distance. Consequently, the increasing of the air pressure led to the declination of fiber diameter in PLA melt blown nonwoven fabrics (Chen & Huang, 2003; Chen, Wang, & Huang, 2004). In addition, it was attributed to viscosity of the molten PLA, which high viscosity of the molten PLA was difficult to blow by hot air at low processing temperature. Therefore, at 250°C PLA fibers sizes were large and exhibited broad distribution. Thus, at 260°C the molten PLA was continuously blown by hot air, which resulted in the reduction of the fiber size and the narrow fiber distribution (Ellison, Phatak, Giles, Macosko, & Bates, 2007; Lee & Wadsworth, 1990; Watanabe, Kim, & Kim, 2011). Ellison et al. reported that polymers in their melt blowing process showed a significant reduction in fiber diameter because of an increase in processing temperatures. It was attributed to an increment in the active temperature window that provided the fiber attenuation when processing temperatures increased. Thus, the polymer fibers remained in the melt state for longer periods of time at higher processing temperatures and encountered an additional attenuation before the polymer solidified via sufficient crystallization or became amorphous. In addition, increasing the temperature would result in a substantial decrease in viscosity (Ellison et al., 2007).

The sound absorption coefficient increased with the small fiber size in which smaller fiber had more porosity and more contact surface with the incident sound. Therefore, the suitable conditions for nonwoven PLA fabric fabrications were at the nozzle temperatures at 260°C, air pressure 0.5 MPa, and die-to-collector distance of 60 cm.

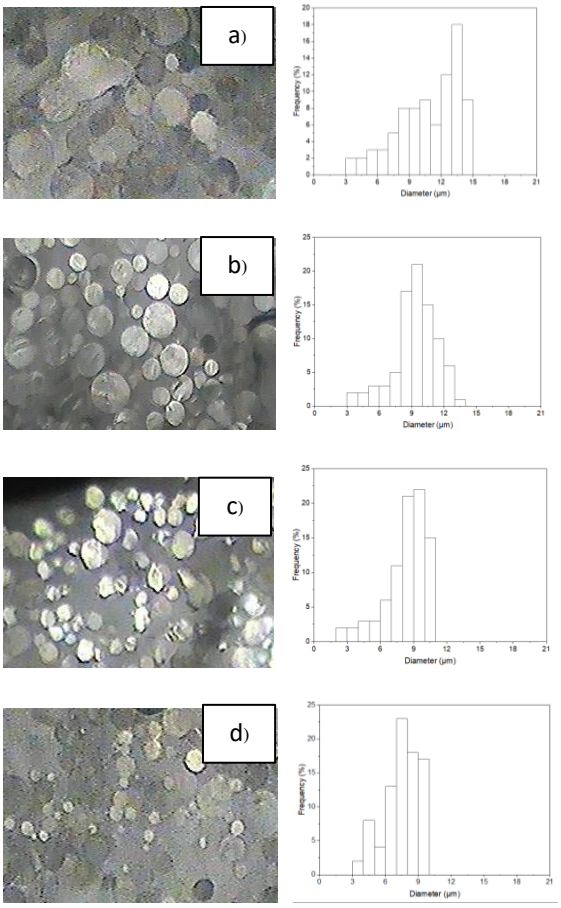

Figure 3. OM and distribution of PLA nonwoven cross section the nozzle temperatures at 250°C (pressure and collector distance): a) 0.3 MPa, 30 cm, b) 0.3 MPa, 60 cm, c) 0.5 MPa, 30 cm and d) 0.5 MPa, 60 cm.

Suan Sunandha Science and Technology Journal
©2022 Faculty of Science and Technology, Suan Sunandha Rajabhat University

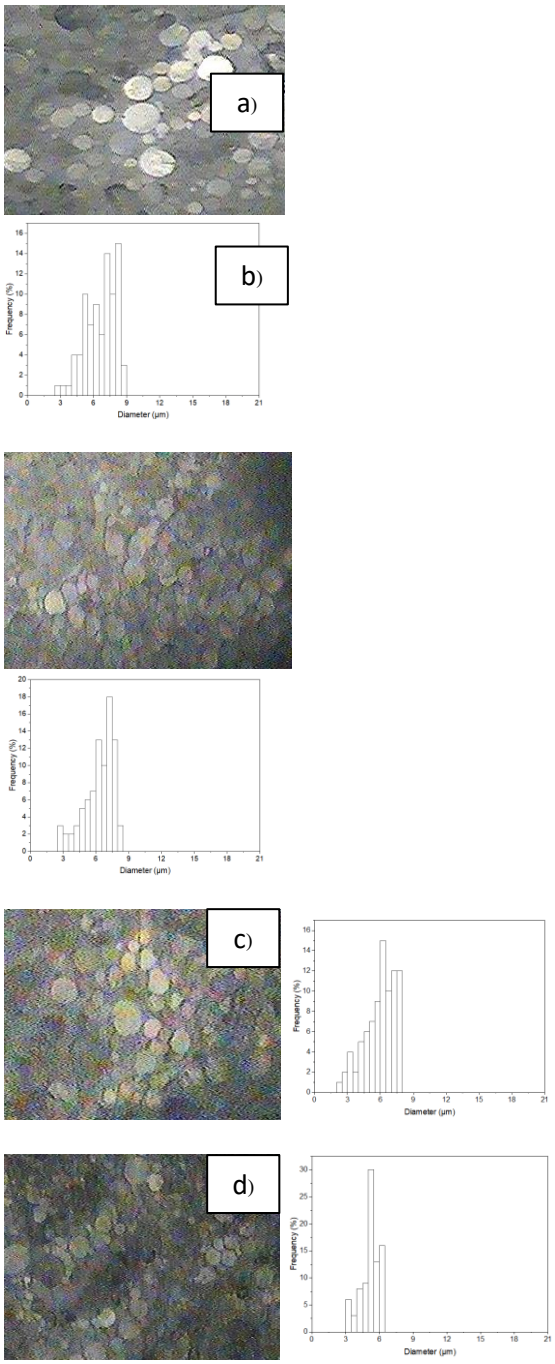

Figure 4. OM and distribution of PLA nonwoven cross section the nozzle temperatures at 260°C (pressure and collector distance): a) 0.3 MPa, 30 cm, b) 0.3 MPa, 60 cm, c) 0.5 MPa, 30 cm and d) 0.5 MPa, 60 cm.

3.4 Air permeability of PLA nonwoven fabric

In order to examine the effect of fiber deformation on the measured air permeability of PLA nonwovens fabric, different pressure gradients at 0.3 and 0.5 MPa were chosen to carry out air permeability testing. The measured air permeability is shown in Figure 5. Since the PLA nonwoven fabric is a loosely bonded fabric, the large spacing between fibers enables the majority of air to flow through these gaps. Obviously, in high nozzle temperatures, air pressures and collector distance present much significant lower air permeability. This is also attributed to their difference in GSM and fabric thickness. For PLA nonwovens fabric with higher GSM and fabric thickness, there is less porosity and air space in textile structure to allow air to go through (Yang et al., 2016). It is observed that air permeability of PLA nonwoven fabric tends to decrease with the increasing GSM and fabric thickness, which is similar to conventional textile fabrics. This is mainly due to the reduction in fiber diameter with increasing air pressure used during melt blowing. Finer fibers lead to reduction in pore size, better packing of the fibers, resulting in reduction in air flow rate through the webs (Broda & Baczek, 2020). Also fibers interlocking in nonwoven are the frictional elements that provide resistance to acoustic wave motion (Ren & Jacobsen, 1993).

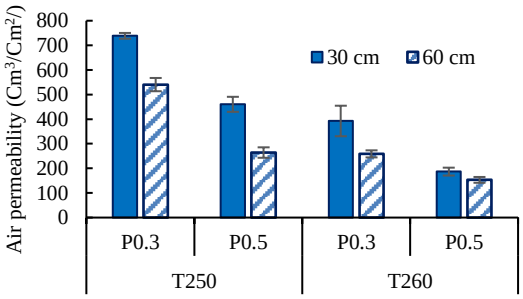

Figure 5. Air permeability of PLA nonwoven fabric (Nozzle temperature 250 and 260°C, Air pressure 0.3 and 0.5 MPa, Collector distance 30 and 60 cm).

3.5 Effect of GSM and thickness on sound absorption

The effect of GSM and thickness on the acoustic properties of PLA nonwoven fabric was investigated by fabricating PLA nonwoven fabric at processing conditions the nozzle temperatures at 260°C, air pressures at 0.5 MPa and collector distance at 60 cm with different thicknesses ranging from 6.50 to 14.75 mm, which was fabricated by melt jet spinning method with different area densities of 229 and 502 GSM. Table 3 shows the thickness and area density of the fabricated PLA nonwoven fabric and hemp nonwoven fabric. It was found that the sound absorption coefficient of the fabricated PLA nonwoven fabric and hemp

Suan Sunandha Science and Technology Journal
©2022 Faculty of Science and Technology, Suan Sunandha Rajabhat University

nonwoven fabric as shown in Figure 6, The PLA nonwoven fabric with the higher GSM and thickness resulted in better sound absorption coefficient compared with the lower GSM and thickness. It also showed a higher sound absorption coefficient compared to the hemp nonwoven fabric. GSM of nonwoven fabric refers to the number of fibers in a certain area, and higher area density indicates the presence of higher proportion of fibers in a specific area, which induces more resistance to the sound wave (Broda & Baczek, 2020; Qui & Enhui, 2018) and contributes to the higher sound absorption tendency (Ganesan & Karthik, 2016; Kucuk & Korkmaz, 2012; Putra, Khair, & Nor, 2015).

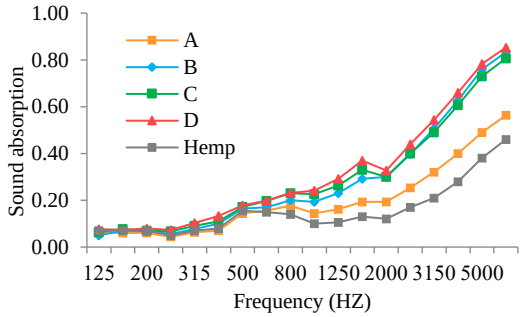

Figure 6. Sound absorption of PLA nonwoven fabric (Nozzle temperature at 260°C, Air pressure at 0.5 MPa, Collector distance at 60 cm) and hemp nonwoven fabric.

Table 3. Effect of GSM and thickness on sound absorption of PLA nonwoven fabric (Nozzle temperature 260°C, Air pressure 0.5 MPa, Collector distance 60 cm) and hemp nonwoven fabric.

Sample	Thickness (mm)	GSM (g/m^2)	NRC
A	6.50 ± 0.25	229 ± 3.35	0.13 ± 0.06
B	10.67 ± 0.58	384 ± 5.25	0.18 ± 0.09
C	13.92 ± 0.58	492 ± 6.03	0.19 ± 0.02
D	14.75 ± 1.75	502 ± 9.00	0.21 ± 0.01
Hemp	10.05 ± 0.19	1094 ± 24.84	0.11 ± 0.04

* NRC = Noise Reduction Coefficient

3.6 Effect of layering sequencing on sound absorption

The effect of layer sequencing on sound absorption was measured with three different placements of the reinforcement fiber layer, i.e., hemp fiber layer, in the composite ‘‘sandwich’’ structure. These three different positions of the reinforcement layer were front side (closest to the air flow source), back side (furthest away from it), or in the middle, as shown in Table 1. The fabrics where the reinforcement was nearest to (front side) or farthest away (back side) from the air flow source in fact were the same fabrics, just flipped to the other side for sound absorption coefficient testing. The material parameters of the fabrics with different layer sequencing are given in Figure 7 and Table 4. It is seen that the fabrics that had their reinforcement layer 1 layer (sample HLL, LHL, LLH), tended to have higher NRC values. In Table 4, the sequencing of each of the fabrics in the fabric group HLL, LHL, LLH had distinctively higher NRC values than the fabric group LHH, HLH, HHL. This suggests that the hemp layer had slightly higher resistivity than PLA layers, although the average diameter of hemp was slightly higher than those of PLA. The high variation in fiber diameter and the irregular shape of hemp fibers might have led to a higher tortuous path to frequency through the fabric layer. It was found that the sound absorption PLA/PLA/Hemp layers showed optimum results.

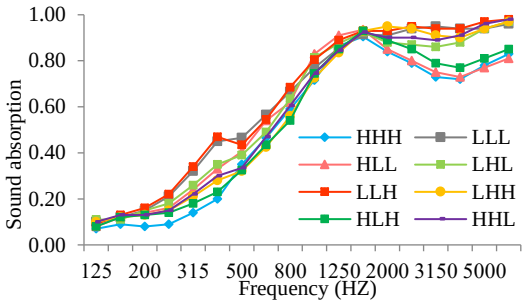

Figure 7. Effect of layering sequencing on sound absorption.

Table 4. Sound absorption coefficient and structure parameter information of webs with different sequencing.

Fabric	Thickness (mm)	GSM (g/m^2)	NRC
HHH	29.06 ± 0.50	3292 ± 38.70	0.50 ± 0.02
LLL	42.25 ± 0.71	1483 ± 33.83	0.59 ± 0.03
HLL	35.62 ± 0.82	2121 ± 34.69	0.56 ± 0.02
LHL	34.87 ± 0.62	2112 ± 23.12	0.57 ± 0.04
LLH	35.89 ± 0.64	2083 ± 36.67	0.60 ± 0.03
LHH	32.57 ± 1.57	3107 ± 44.20	0.54 ± 0.07
HLH	32.06 ± 1.50	3114 ± 38.56	0.53 ± 0.07
HHL	32.53 ± 0.94	3120 ± 26.86	0.53 ± 0.05

Suan Sunandha Science and Technology Journal
©2022 Faculty of Science and Technology, Suan Sunandha Rajabhat University

4. Conclusion

PLA nonwoven fabric was prepared using a melt jet spinning process. The spinning process was carried out at 250 and 260°C with screw speed of 10 rpm and air blown pressure of 0.3 and 0.5 MPa. The die-to-collector of fabric production was studied at 30 and 60 cm to compare the nonwoven fabric product property. The process temperature, air pressure and die-to-collector distance have significant effects on the nonwoven fabric thickness, GSM, and fabric density. Air permeability decreased with high fabric thickness as well as fine fibers which supported the property of sound absorbing panels. Therefore, the suitable conditions for sound absorbing panel fabrication were process temperature of 260°C, air pressure 0.5 MPa and die-to-collector distance of 60 cm. Sound absorbing coefficient measurement revealed that GSM fabric thickness showed effect on increasing sound absorption. The effect of nonwoven sheet order and arrangement of PLA nonwoven and hemp nonwoven of 3 layers sandwich indicated that the layers order of PLA/PLA/PLA showed higher sound absorbing coefficient than the Hemp/Hemp/Hemp due to fiber size and arrangement. However, the sheet layer order of PLA/PLA/Hemp showed a high sound absorbing coefficient comparable with PLA/PLA/PLA. Therefore, produced from biodegradable polymer and natural fiber can be effectively used for sound absorbing panels.

5. References

Al-Shammari, B., Al-Fariss, T., Al-Sewailm, F., & Elleithy, R. (2011). The effect of polymer concentration and temperature on the rheological behavior of metallocene linear low density polyethylene (mLLDPE) solutions. *Journal of King Saud University - Engineering Sciences*, *23*(1), 9-14. doi:10.1016/j.jksues. 2010.07.001

Benkreira, H., Khan, A., & Horoshenkov, K. V. (2011). Sustainable acoustic and thermal insulation materials from elastomeric waste residues. *Chemical Engineering Science*, *66*(18), 4157-4171. doi:10.1016/j.ces.2011.05.047

Broda, J., & Baczek, M. (2020). Acoustic properties of multi-layer wool nonwoven structures. *Journal of Natural Fibers*, *17*(11), 1567-1581. doi:10.1080/15440478.2019.1584078

Chavan, A. T., & Manik, D. N. (2008). Optimum design of vibro-acoustic systems using SEA. *International Journal of Acoustics and Vibrations*, *13*(2), 67-72.

Chen, T., & Huang, X. (2003). Modeling polymer air drawing in the melt blowing nonwoven process. *Textile Research Journal*, *73*(7), 651-654. doi:10.1177/004051750307300715

Chen, T., Wang, X., & Huang, X. (2004). Modeling the air-jet flow field of a dual slot die in the melt blowing nonwoven process. *Textile Research Journal*, *74*(11), 1018-1024 doi:10.1177/004051750407401114

Coates, M., & Kierzkowski, M. (2002). Acoustic textiles – Lighter, thinner and more absorbent. *Technical Textile International*, *11*(7), 15-18.

Devi, R. P. (2014). A study on acoustic properties of polyester and hollow polyester non woven fabrics. *International Journal of Advanced Technology in Engineering and Science*, *2*, 446-459.

Ellison, C. J., Phatak, A., Giles, D. W., Macosko, C. W., & Bates, F. S. (2007). Melt blown nanofibers: Fiber diameter distributions and onset of fiber breakup. *Polymer*, *48*(11), 3306-3316. doi:10.1016/j.polymer.2007.04.005

Ganesan, P., & Karthik, T. (2016). Development of acoustic nonwoven materials from kapok and milkweed fibres. *The Journal of The Textile Institute*, *107*(4), 477-482. doi:10.1080/ 00405000.2015.1045251

Korte, S., & Staiger, M. P. (2008). Effect of processing route on the composition and properties of hemp fibre. *Fibers and Polymers*, *9*, 593-603. doi:10.1007/ s12221-008-0095-0

Kucuk, M., & Korkmaz, Y. (2012). The effect of physical parameters on sound absorption properties of natural fiber mixed nonwoven composites. *Textile Research Journal*, *82*(20), 2043-2053. doi:10.1177/0040517 512441987

Lee, Y., & Wadsworth, L. C. (1990). Structure and filtration properties of melt blown polypropylene webs. *Polymer Engineering and Science*, *30*(22), 1413-1419. doi:10.1002/pen .760302202

Mohammad, M., Nik Syukri, N. I. R., & Nuawi, M. Z. (2019). Sound properties investigation of date palm fiber. *Journal of Physics: Conference Series*, *1150*(1). doi:10.1088/ 1742-6596/1150/1/012003

Oh, K. W., Kim, D. K., & Kim, S. H. (2009). Ultra-porous flexible PET/Aerogel blanket for sound absorption and thermal insulation. *Fibers and Polymers*, *10*(5), 731-737, doi:10.1007/ s12221-010-0731-3

Suan Sunandha Science and Technology Journal
©2022 Faculty of Science and Technology, Suan Sunandha Rajabhat University

Prahsarn, C., Klinsukhon, W., Suwannamek, N., Wannid, P., & Padee, S. (2020). Sound absorption performance of needle-punched nonwovens and their composites with perforated rubber. *SN Applied Sciences*, *2*(4). doi:10.1007/s42452-020-2401-4

PricewaterhouseCoopers. (2007). *The automotive industry and climate change*. Retrieved from http://www.pwc.com/th/en/automotive/assets/co2

Putra, A., Khair, F. A., & Nor, M. J. M. (2015). Utilizing hollow-structured bamboo as natural sound absorber. *Archives of Acoustics*, *40*(4), 601-608. doi:10.1515/aoa-2015-0060

Qui, H., & Enhui, Y. (2018). Effect of thickness, density and cavity depth on the sound absorption properties of wool boards. *Autex Research Journal*, *18*(2), 203-208. doi:10.1515/aut-2017-0020

Ren, M., & Jacobsen, F. (1993). A method of measuring the dynamic flow resistance and reactance of porous materials. *Applied Acoustics*, *39*(4), 265-276. doi:10.1016/0003-682X(93)90010-4

Sengupta, S. (2010). Sound reduction by needle-punched nonwoven fabrics. *Indian Journal of Fibre and Textile Research*, *35*(3), 237-242.

Tascan, M., & Vaughn, E. A. (2008). Effects of total surface area and fabric density on the acoustical behavior of needlepunched nonwoven fabrics. *Textile Research Journal*, *78*(4), 289-296. doi:10.1177/0040517507084283

Watanabe, K., Kim, B. S., & Kim, I. S. (2011). Development of polypropylene nanofiber production system. *Polymer Reviews*, *51*(3), 288-308. doi:10.1080/15583724.2011.594195

Wertel, S. J. (2000). Experimental analysis of noise reduction properties of sound absorbing foam. (Master's thesis). University of Wisconsin-Stout, Menomonie.

Yang, T., Xiong, X., Mishra, R., Novák, J., Chaloupek, J., Sanetrnik, F., & Militký, J. (2016). Investigation on acoustic behavior and air permeability of struto nonwovens. *Fibers and Polymers*, *17*(12), 2078-2084. doi:10.1007/s12221-016-6967-9

Yilmaz, N. D. (2009). *Acoustic properties of biodegradable nonwovens* (Doctoral dissertation). North Carolina State University, North Carolina.

Yilmaz, N. D., Banks-Lee, P., Powell, N. B., & Michielsen, S. (2011). Effects of porosity, fiber size, and layering sequence on sound absorption performance of needle-punched nonwovens. *Journal of Applied Polymer Science*, *121*(5), 3056-3069. doi:10.1002/ app.33312

Zhu, W., Nandikolla, V., & George, B. (2015). Effect of bulk density on the acoustic performance of thermally bonded nonwovens. *Journal of Engineered Fibers and Fabrics*, *10*(3), 39-45. doi:10.1177/155892501501000316

Available online at http://www.ssstj.sci.ssru.ac.th

Suan Sunandha Science and Technology Journal

©2022 Faculty of Science and Technology, Suan Sunandha Rajabhat University

Effect of Wet Spinning Parameters on Bamboo Cellulose Nanofiber Filament Preparation

Nawaporn Permsombut[1], Sommai Pivsa-Art[1], Natee Srisawasd[2], Weraporn Pivsa-Art[1*]

[1]Department of Chemical and Materials Engineering, Faculty of Engineering, Rajamangala University of Technology Thanyaburi, Pathum Thani 12110, Thailand

[2]Department of Textile Engineering, Faculty of Engineering, Rajamangala University of Technology Thanyaburi, Pathum Thani 12110, Thailand

***Corresponding author e-mail: weraporn.p@en.rmutt.ac.th**

Received: *22 February 2022* / **Revised**: *14 March 2022* / **Accepted:** *14 June 2022*

Abstract

Cellulose nanofibers (CNF) are materials synthesized from wood-based fibers having excellent mechanical properties due to their high crystallinity. In this research, the cellulose nanofibers were synthesized from bamboo fibers, as the abundant natural fibers available worldwide. The cellulose nanofibers had been synthesized using chemical processes of bleaching with acetic acid and sodium chloride, followed by alkaline treatment with sodium hydroxide, and acid hydrolysis with sulfuric acid combined with mechanical process in ultrasonic bath. Isolation of nanocellulose from bamboo scrap raw material was confirmed by different analysis methods. The morphology of CNF was characterized by using a scanning electron microscope (SEM). Fourier transform infrared spectrometer (FT-IR) and X-Ray Diffractometer (XRD) examined chemical structure and identified the crystallinity of nanocellulose materials. The monofilament of cellulose nanofibers was prepared by using a wet spinning process. The effects of coagulating solvent, water, methanol, acetone, and calcium chloride ($CaCl_2$) on monofilament formation were studied. Morphology study of CNF monofilament was carried out using a digital camera to observe the spinnability of the monofilament and the relationship with wet spinning process conditions. The thermal properties of the nanocellulose spun in methanol and acetone as coagulation solvent were analyzed by differential scanning calorimeter (DSC) and thermogravimetric analysis (TGA). Also, the measuring of degradation temperature of nanocellulose spun compared with the nanocellulose extracted.

Keywords: Cellulose nanofibers, Bamboo fibers, Wet spinning, Monofilament

1. Introduction

Recently, materials that are friendly to the environment and biodegradable have become more useful and more acceptable in worldwide application (Qiu et al., 2021). It is noteworthy to mention microplastic accumulation problems would affect different living organisms specially human and aquatic animals (Svensson, Ferreira, Hakkarainen, Adolfsson, & Zamani, 2021). The microplastic problems arise from plastic petroleum waste which have difficulty in decomposing and degrade for turning to nature (Chaichi, Hashemi, Badii, & Mohammadi, 2017; Nazrin et al., 2020). The effects reinforce the research and development of a new material, a composite material based on natural resources or agricultural wastes which can replace the plastic industry (Liminana, Garcia-Sanoguera, Quiles-Carrillo, Balart, & Montanes, 2018; Wu, Misra, & Mohanty, 2020). The general structure of plant fibers consists of cellulose, hemicellulose, lignin and other substances. The cellulose is the main constituent which is an organic substance that gives strength for the cell wall. The natural fiber is used in many applications, for example in the textile industry, in the pharmaceutics and in food packaging (Rostamitabar et al., 2021; Vanitha & Kavitha, 2021). Bamboo plant is popular and cultivated in many countries in Asia. The bamboo can grow rapidly and acclimate to several weather conditions. The bamboo has a great surface area and a high cross-linking property (Qian, Zhang, Yao, & Sheng, 2018). In addition, bamboo has a good property of high productivity and biomass density. The bamboo also shows anti-bacterial and UV protective

Suan Sunandha Science and Technology Journal
©2022 Faculty of Science and Technology, Suan Sunandha Rajabhat University

properties (Singla et al., 2017). Due to their ability, bamboo is applied in many industries including papermaking, furniture, construction materials, textile, musical instruments, etc. (Abdul Khalil et al., 2012; Silva, Menis-Henrique, Felisberto, Goldbeck, & Clerici, 2020). In addition, the bamboo is a popular plant that has a great deal for usage in the polymer composite sector (Abdul Khalil et al., 2012). Synthesis of cellulose from plant cell wall or agricultural residues can be prepared in different solutions such as mechanical, biological, chemical or combination techniques. The mixed chemical and mechanical are commonly used with application different treatment techniques. The treatment is necessary to remove non-cellulosic material (Joy et al., 2016). Many studies have been done to separate cellulose filaments such as, Homogenization, grinding, micro-fluidization, oxidation and acid hydrolysis. The cellulose fiber can be spun in suitable condition (Kafy et al., 2017). The usage of cellulose nanofibril and cellulose nanocrystals are more applicable in medical sectors (Benini, Voorwald, Cioffi, Rezende, & Arantes, 2018; Gupta, Revagade, Anjum, Atthoff, & Hilborn, 2006) and also in polymer nanocomposite (Qian et al., 2018). There are various types of polymers fiber forming process such as dry spinning, wet spinning and melt spinning (Gupta et al., 2006). In the wet spinning process, the polymer is injected in the coagulation bath which help solidification the spun fiber solution or gel to the spun fiber filament. This (The wet spinning) technique is suitable to produce small quantity samples for medical devices (Lundahl, Klar, Wang, Ago, & Rojas, 2017). In this research, the preparation of nanocellulose fiber from the bamboo using chemical and mechanical process was studied. The bamboo was treated with bleaching and alkaline treatments follow by acid hydrolysis process with ultrasonic to obtain nanocellulose. The chemical properties, physical properties, and morphology of prepared nanocellulose from bamboo were characterized by FTIR, XRD and SEM, respectively. The mono-nanocellulose filaments were prepared from extracted nanocellulose and formed by wet spinning process. We studied the effect of coagulants including methanol, water, calcium chloride and acetone. The mono-nanocellulose filaments were analyzed the spinnability and their thermal properties.

2. Materials and Methods

2.1 Materials

Bamboo fibers used for preparation of nanocellulose were received from Kanchanaburi province, Thailand. The fibers were sieving to size of 20-40 mesh. Acetic acid was purchased from VWR Chemical company. Sodium chloride, sodium chlorite and sodium hydroxide were purchased from Ajak Finechem. Sulfuric acid, acetone and methanol were obtained from RCI Lab Scan Limited.

2.2 Preparation of nanocellulose

The bamboo was first bleached with 10 ml acetic acid and 60 g of $NaClO_2$ at 75°C for 1 h. This step was repeated for three times until the color of bamboo became white or very light yellow. In the alkaline treatment process, the bleached bamboo was treated in 5 M NaOH solution for 24 h (change the NaOH solution for each of 4 h) at room temperature. The residual was filtered and rinsed several times until its pH became neutral. The acid hydrolysis process, 50 wt% H_2SO_4 was added in a sample that was subjected to an ultrasonic generator at 50°C for disintegration of nanocellulose fiber (Kwak, Lee, Lee, & Jin, 2018). After 1 h, the reaction was interrupted by adding 250 ml of cold deionized (DI) water. Finally, the residue was centrifuged and dialyzed with water until neutral pH was reached. The preparation steps of nanocellulose from raw material bamboo was presented in Figure 1.

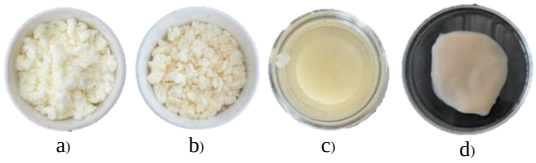

Figure 1. Products from nanocellulose extraction a) bleaching process b) alkaline treatment process c) acid hydrolysis process and d) nanocellulose.

2.3 Wet-spinning process of the bamboo nanocellulose

The nanocellulose suspensions were injected into the different coagulation baths (methanol, water, calcium chloride and acetone). The nanocellulose extracted previously was added in a 10 ml syringe, 14.5 mm of inner diameter equipped with 18G needle (1.2 mm of diameter). The syringe

Suan Sunandha Science and Technology Journal
©2022 Faculty of Science and Technology, Suan Sunandha Rajabhat University

was installed with a single syringe pump, NE-1000 model that was parameter volumetric flow at 3 ml/min. The flow rate value assumes a minimum continuous flow of the nanocellulose suspension. The different coagulation baths were filled in a glass plate with a 25 ml solution. The spun fiber was left in the solution for a while before collecting. Figure 2 shows the wet spinning process.

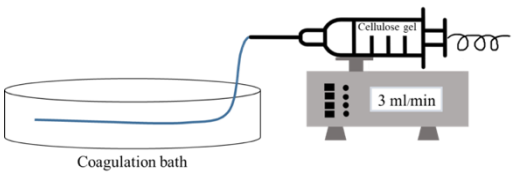

Figure 2. Wet spinning process.

2.4 Characterization

2.4.1 Chemical property of nanocellulose

The FTIR spectra of original bamboo, bleached bamboo, alkalied bamboo and nanocellulose were recorded using a Thermo scientific model Nicolet 6700 FTIR spectrometer with wavelength of 4,000-500 cm^{-1} at 1 cm^{-1} resolution and a frequency of 32 scans for each sample.

2.4.2 Crystallinity of nanocellulose

The crystallinity of the nanocellulose was characterized using Panalytical X'pert PRO, PW 3040/60 X-Ray diffractometer operated at Cu Kα radiation (λ= 1.54 ˚A), 30 kV and 20 mA, analyzed at 2θ from 5-80˚.

2.4.3 Morphology of nanocellulose

The morphological structure of original bamboo, bleached bamboo, alkalied bamboo and nanocellulose were investigated using a JSM 5410-LV Scanning Electron Microscope (JEOL, Japan). Samples were placed on carbon tapes and then coated with platinum (Pt) using a sputtering coater. The analysis of fiber surface characterized on vacuum system, 15 kV power at 100X and 500X magnification.

2.4.4 Thermal properties

The Thermal properties were analyzed with differential scanning calorimeter (DSC), Mettler Toledo model DSC 3 plus star system and thermogravimetric analysis (TGA), Mettler Toledo model TGA/DSC 3 plus. The thermal analysis was carried out by using STARe software. The sample tested their thermal properties with 20 ml/min nitrogen flow and heat rate of 10°C/min. The range of temperature study was between 25°C to 500°C which covers the cellulose decomposition temperature range.

2.4.5 Spinnability of fiber in coagulation bath

The spun nanocellulose monofilament in different coagulation baths was recorded with a digital camera OLYMPUS OM-D E-M10 Mark II which was used to observe and describe the spinnability of cellulose fiber.

3. Results and Discussions

3.1 Chemical structure analysis

Modification of chemical structure in different process treatments appears in Figure 3 which represents the relationship between wavelength and functional groups. The range of 2800-3500 cm^{-1} and 500-1800 cm^{-1} were two important absorbance peaks. Peaks at 3340 cm^{-1} represented a stretching vibration hydroxy group (O–H). The hydroxy group is generally found in cellulose, hemi-cellulose and lignin (Kwak et al., 2018) that can be observed in all samples. Also, the absorbance peak at 2900 cm^{-1} refers to -CH_2 that presents in the bamboo raw material and the treated bamboo (Xie et al., 2016). The absorbance peak at 1650-1700 cm^{-1} and at 1200 cm^{-1} are corresponded to carbonyl ring observed in hemi-cellulose and methoxyl groups (Theivasanthi, Anne Christma, Toyin, Gopinath, & Ravichandran, 2018), respectively. In cellulosic samples, curve after acid hydrolysis process, we could observe absence of peak 1600 cm^{-1} and reduction of peak 1230 cm^{-1} that represented chemical bond of lignin and lower content of hemi-cellulose after alkali treatment and acid hydrolysis. The peak at 1700 cm^{-1} became more obvious after bleaching and alkali treatments. It was observed obviously in the acid hydrolysis step which refers to the elimination of contaminants and lignin and partial hemi-cellulose.

Suan Sunandha Science and Technology Journal
©2022 Faculty of Science and Technology, Suan Sunandha Rajabhat University

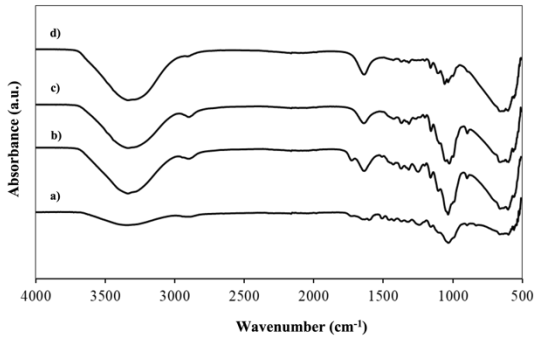

Figure 3. FT-IR results of original bamboo a), bleached fiber b), alkali-treated fiber c), and acid-hydrolyzed fiber d).

Table 1. The relationship between wavenumber and chemical function group.

Wavenumber (cm^{-1})	Function group	Reference
1200-1230	Methoxyl	Theivasanthi et al., 2018; Xie et al., 2016
1600	Methyl	Jiang et al., 2020
1650-1700	Carbonyl ring	Theivasanthi et al., 2018
2900	Methylene	Theivasanthi et al., 2018
3340	Hydroxy group	Kwak et al., 2018; Xie et al., 2016

3.2 Crystallinity

X-ray diffractogram of residue for each process was shown in Fig. 4. All diffractograms contained two 2 intense peaks, first at 16° and second at 22°. These peaks presented significance of cellulose crystalline structure. The peak at 2θ = 16° corresponded to crystallographic planes that is characteristic of crystallographic semi-crystalline materials such as lignocellulosic (Xie et al., 2016). The 2θ = 22° peak verified characteristic of crystalline cellulose. Increasing peaks in cellulose samples present dissolution and removal of non-cellulosic materials such as lignin and extractives from the amorphous regions. The crystallinity of cellulose increases with the next steps of the treatment process (Singh, Gaikwad, Park, & Lee, 2017). From the diffractogram, the peak of the acid hydrolysis process could present more evidence due to the reduction of the amorphous part of hemi-cellulose and lignin.

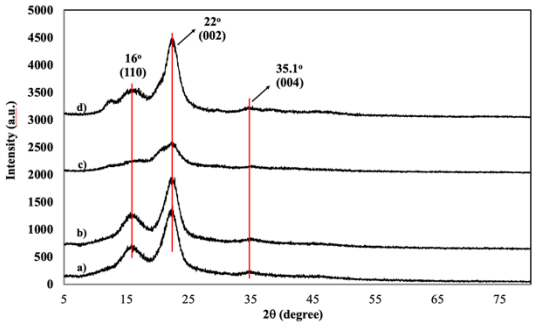

Figure 4. XRD results of original bamboo a), bleached fiber b), alkali-treated fiber c), and acid-hydrolyzed fiber d).

Table 2. The result from XRD data.

Peak position (degree)	Characteristic	Reference
16 (110)	semi-crystalline	Gong, Li, Xu, Xiang, & Mo, 2017; Theivasanthi et al., 2018; Xie et al., 2016
22 (002)	crystalline	

3.3 Morphology of nanocellulose

The scanning electron microscopy (SEM) in Fig.6 shows the morphology of different steps to isolate nanocellulose fiber from raw bamboo fiber. Fig.5 a), the original bamboo had a large size and rough surface. After the bleaching step, the impurities such as wax were eliminated. The surface area became more clear and smooth (Xie et al., 2016). Sizing of bleached fiber was not observed. The morphology of treated fibers with alkali solution 24 h shows in Figure 5 c), presented considerably smaller and longer fiber. The hemi-cellulose and lignin were removed from cellulose fibril. The morphology of residue from the acid hydrolysis process shows in Figure 5 d) with magnitude 500X suspension of nanocellulose diluted in water (Figure 5 d). Chemical and mechanical under ultrasonic technique induced the elimination of non-cellulosic compounds from original bamboo. The strong acid hydrolysis was used to fibrillate the micro cellulose sizing to nanocellulose (Kwak et al., 2018).

Suan Sunandha Science and Technology Journal
©2022 Faculty of Science and Technology, Suan Sunandha Rajabhat University

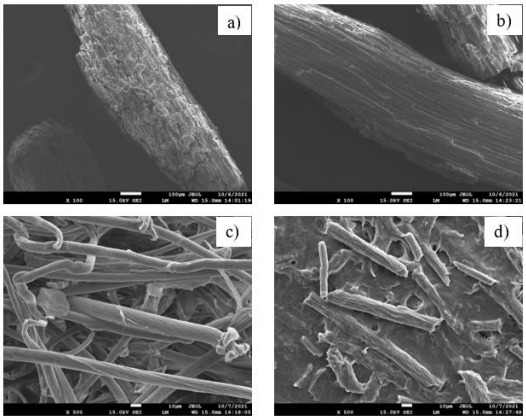

Figure 5. SEM images of original bamboo a), bleached fiber b), alkali-treated fiber c), and acid-hydrolyzed fiber d).

3.4 Spinnability of monofilament in different coagulation bath

Figure 3 shows spun fiber of different coagulation solvent selections. The spun cellulose filament in the $CaCl_2$ coagulation bath can spin easily differently from the other bath. The fiber injection in $CaCl_2$ solution, methanol solution and water as coagulation bath have a smooth and a uniform filament. However, the fiber in acetone was not a uniform filament. The acetone caused the cellulose suspension to dehydrate, encouraging the aggregation of cellulose spun and their retention in fibrous structures (Geng, Chen, Peng, & Kuang, 2017). The role of calcium chloride is ionic effect. The cellulose fiber created a crosslinking with Ca^{2+} ions and was solidified in filament (Kafy et al., 2017; Wang et al., 2019). In Figure 6, the fiber in methanol and $CaCl_2$ have continuity comparison to acetone bath, the fiber in acetone breaks easily and is discontinued. Furthermore, after leaving spun fiber in the solution, filament in water was dissolved in the water solution. The methanol and the acetone are completely evaporated and remaining only fibers.

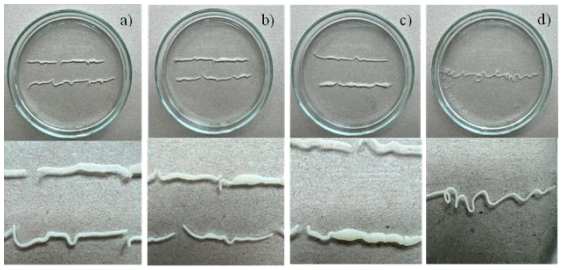

Figure 6. Spun cellulose monofilament in water a), methanol b), acetone c) and calcium chloride d).

3.5 Thermal properties

The thermal properties of monofilament injected in methanol bath, in acetone bath and in calcium chloride bath were compared with the cellulose extracted and presented in Figure 7 and Figure 8. The melting point of cellulose extracted was 210°C.

The DSC thermal curve of the cellulose and monofilaments were presented in Figure 7. The DSC curve present two temperatures observed in all samples; cellulose, C-Acetone (cellulose injected in acetone as coagulant), C-Methanol (cellulose injected in methanol as coagulant), and C-$CaCl_2$ (cellulose injected in calcium chloride as coagulant). The cellulose extracted from the bamboo with chemical and mechanical process had a degradation temperature at 210°C. The temperatures of spun cellulose were 221°C in acetone, 225°C in $CaCl_2$ and 228°C in methanol. The first peak of C-Methanol and C-$CaCl_2$ were observed at 108°C and 134°C, respectively, which presented the evaporation of moisture content in the sample.

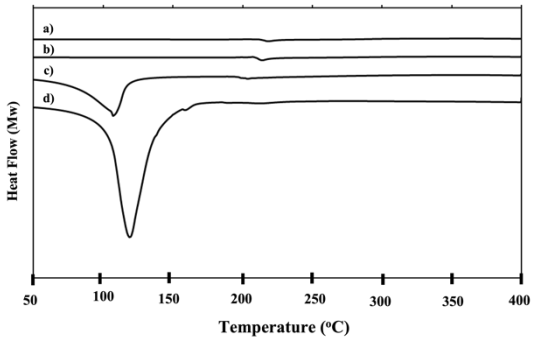

Figure 7. DSC thermal curves of cellulose a), monofilament injected in acetone bath b), in methanol bath c) and in $CaCl_2$ d).

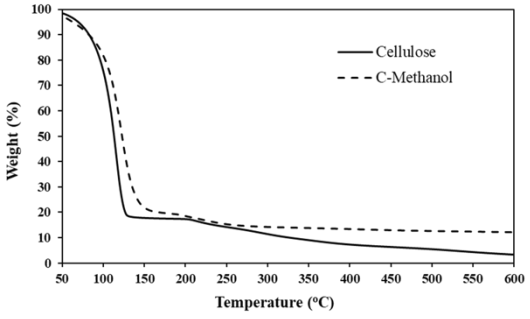

Figure 8. TGA thermal curves of the cellulose and the cellulose in methanol as coagulant.

Suan Sunandha Science and Technology Journal
©2022 Faculty of Science and Technology, Suan Sunandha Rajabhat University

In addition, TGA measured the change in percent weight of sample during heating from 30 to 500°C. From Figure 8, it shows the first phase of the decline in TGA curve that refers to the evaporation of the moisture content in the sample. The degradation temperature of the cellulose extracted began more quickly than the cellulose spun fiber in methanol. The data in Table 3 shows detail of temperature and residue sample weight. When the cellulose fiber heated to 144°C, the mass about 82.1% dissipated dramatically. That indicates a large amount of moisture in the cellulose fiber. In the second part, the weight change of mass was slightly. At the temperature 264°C, the residue is 13.6%. For the spun fiber in methanol, the mass loss was 80.2% at 168°C indicating the lower water molecule content in the spun fiber. And when the temperature reaches to 212°C, the residue of the spun fiber remains 17.6%.

Table 3. The degradation temperature of cellulose and the cellulose in different coagulant.

Sample	Temperature (°C)	Residue (%)
Cellulose	264	13.6
C-Methanol	212	17.6

4. Conclusion

The cellulose nanofibers (CNF) were extracted from bamboo fibers using chemical and ultrasonic processes. The bleaching, alkali treatment and sulfuric acid reach to disintegrate and eliminate non-cellulosic. The monofilament of cellulose nanofibers was prepared using a wet spinning process. The effect of coagulating solvent consisting of water, methanol, acetone and $CaCl_2$ on monofilament formation was studied. The monofilament of cellulose nanofibers was produced in methanol and calcium chloride coagulating solvent. Morphology study of CNF monofilament verified the relationship with wet spinning process conditions. The CNF monofilament prepared in methanol as coagulant showed higher thermal properties due to the degradation at high concentration of acid sulfuric on acid hydrolysis step and high temperature of ultrasonic under exothermic reaction.

5. Acknowledgement

This study was supported by Asst. Prof. Dr. Weraporn Pivsa-Art and involved faculty members who help to provide guidance, advice, and assistance in all aspects in the research.

6. References

Abdul Khalil, H. P. S., Bhat, I. U. H., Jawaid, M, Zaidon, A., Hermawan, D, & Hadi, Y. S. (2012). Bamboo fibre reinforced biocomposites: A review. *Materials & Design*, *42*, 353-368. doi:10.1016/j.matdes.2012.06.015

Benini, K. C. C. C., Voorwald, H. J. C., Cioffi, M. O. H., Rezende, M. C., & Arantes, V. (2018). Preparation of nanocellulose from *Imperata brasiliensis* grass using Taguchi method. *Carbohydrate Polymers*, *192*, 337-346.doi:10.1016/j.carbpol.2018.03.055

Chaichi, M., Hashemi, M., Badii, F., & Mohammadi, A. (2017). Preparation and characterization of a novel bionanocomposite edible film based on pectin and crystalline nanocellulose. *Carbohydrate Polymers*, *157*, 167-175. doi:10.1016/j.carbpol.2016.09.062

Geng, L., Chen, B., Peng, X., & Kuang, T. (2017). Strength and modulus improvement of wet-spun cellulose I filaments by sequential physical and chemical cross-linking. *Materials & Design*, *136*, 45-53. doi:10.1016/j.matdes.2017.09.054

Gong, J., Li, J., Xu, J., Xiang, Z., & Mo, L. (2017). Research on cellulose nanocrystals produced from cellulose sources with various polymorphs. *RSC Advances*, *7*, 33486-33493. doi:10.1039/C7RA06222B

Gupta, B., Revagade, N., Anjum, N., Atthoff, B., & Hilborn, J. (2006). Preparation of poly(lactic acid) fiber by dry-jet-wet-spinning. I. Influence of draw ratio on fiber properties. *Journal of Applied Polymer Science*, *100*(2), 1239-1246. doi:10.1002/app.23497

Jiang, S., Wei, Y., Hu, Z., Ge, S., Yang, H., & Peng, W. (2020). Potential application of bamboo powder in PBS bamboo plastic composites. *Journal of King Saud University - Science*, *32*, 1130-1134. doi:10.1016/j.jksus.2019.10.014

Joy, J., Jose, C., Varanasi, S. B., Mathew, P., Thomas, S., & Pilla, S. (2016). Preparation and characterization of poly(butylene succinate) bionanocomposites reinforced with cellulose nanofiber extracted from *Helicteres isora* plant. *Journal of Renewable Materials*, *4*, 351-364. doi:10.7569/JRM.2016.634128

Kafy, A., Kim, H. C., Zhai, L., Kim, J. W., Hai, L. V., Kang, T. J., & Kim, J. (2017). Cellulose long fibers fabricated from cellulose nanofibers and its strong and tough

©2022 Faculty of Science and Technology, Suan Sunandha Rajabhat University

characteristics. *Scientific Reports*, *7*, 17683. doi:10.1038/s41598-017-17713-3

Kwak, H. W., Lee, H., Lee, M. E., & Jin, H.-J. (2018). Facile and green fabrication of silk sericin films reinforced with bamboo-derived cellulose nanofibrils. *Journal of Cleaner Production*, *200*, 1034-1042. doi:10.1016/j.jclepro.2018.07.289

Liminana, P., Garcia-Sanoguera, D., Quiles-Carrillo, L., Balart, R., & Montanes, N. (2018). Development and characterization of environmentally friendly composites from poly(butylene succinate) (PBS) and almond shell flour with different compatibilizers. *Composites Part B: Engineering*, *144*, 153-162. doi:10.1016/j.compositesb.2018.02.031

Lundahl, M. J., Klar, V., Wang, L., Ago, M., & Rojas, O. J. (2017). Spinning of cellulose nanofibrils into filaments: A review. *Industrial & Engineering Chemistry Research*, *56*(1), 8-19. doi:10.1021/acs.iecr.6b04010

Nazrin, A., Sapuan, S. M., Zuhri, M. Y. M., Ilyas, R. A., Syafiq, R., & Sherwani, S. F. K. (2020). Nanocellulose reinforced thermoplastic starch (TPS), polylactic acid (PLA), and polybutylene succinate (PBS) for food packaging applications. *Frontiers in Chemistry*, *8*, 1-12. doi:10.3389/fchem.2020.00213

Qian, S., Zhang, H., Yao, W., & Sheng, K. (2018). Effects of bamboo cellulose nanowhisker content on the morphology, crystallization, mechanical, and thermal properties of PLA matrix biocomposites. *Composites Part B: Engineering*, *133*, 203-209. doi:10.1016/j.compositesb.2017.09.040

Qiu, S., Zhou, Y., Waterhouse, G. I. N., Gong, R., Xie, J., Zhang, K., & Xu, J. (2021). Optimizing interfacial adhesion in PBAT/PLA nanocomposite for biodegradable packaging films. *Food Chemistry*, *334*, 127487. doi:10.1016/j.foodchem.2020.127487

Rostamitabar, M., Subrahmanyam, R., Gurikov, P., Seide, G., Jockenhoevel, S., & Ghazanfari, S. (2021). Cellulose aerogel micro fibers for drug delivery applications. *Materials Science and Engineering: C*, *127*, 112196. doi:10.1016/j.msec.2021.112196

Silva, M. F., Menis-Henrique, M. E. C., Felisberto, M. H. F., Goldbeck, R., & Clerici, M. T. P. S. (2020). Bamboo as an eco-friendly material for food and biotechnology industries. *Current Opinion in Food Science*, *33*, 124-130. doi:10.1016/j.cofs.2020.02.008

Singh, S., Gaikwad, K. K., Park, S. I., & Lee, Y. S. (2017). Microwave-assisted step reduced extraction of seaweed (*Gelidiella aceroso*) cellulose nanocrystals. *International Journal of Biological Macromolecules*, *99*, 506-510. doi:10.1016/j.ijbiomac.2017.03.004

Singla, R., Soni, S., Patial, V., Kulurkar, P. M., Kumari, A., Mahesh, S., … Yadav, S. K. (2017). In vivo diabetic wound healing potential of nanobiocomposites containing bamboo cellulose nanocrystals impregnated with silver nanoparticles. *International Journal of Biological Macromolecules*, *105*, 45-55. doi:10.1016/j.ijbiomac.2017.06.109

Svensson, S. E., Ferreira, J. A., Hakkarainen, M., Adolfsson, K. H., & Zamani, A. (2021). Fungal textiles: Wet spinning of fungal microfibers to produce monofilament yarns. *Sustainable Materials and Technologies*, *28*, e00256. doi:10.1016/j.susmat.2021.e00256

Theivasanthi, T., Anne Christma, F. L., Toyin, A. J., Gopinath, S. C. B., & Ravichandran, R. (2018). Synthesis and characterization of cotton fiber-based nanocellulose. *International Journal of Biological Macromolecules*, *109*, 832-836. doi:10.1016/j.ijbiomac.2017.11.054

Vanitha, R., & Kavitha, C. (2021). Development of natural cellulose fiber and its food packaging application. *Materials Today: Proceedings*, *36*, 903-906. doi:10.1016/j.matpr.2020.07.029

Wang, L., Ago, M., Borghei, M., Ishaq, A., Papageorgiou, A. C., Lundahl, M., & Rojas, O. J. (2019). Conductive carbon microfibers derived from wet-spun lignin/nanocellulose hydrogels. *ACS Sustainable Chemistry & Engineering*, *7*(6), 6013-6022. doi:10.1021/acssuschemeng.8b06081

Wu, F., Misra, M., & Mohanty, A. K. (2020). Sustainable green composites from biodegradable plastics blend and natural fibre with balanced performance: Synergy of nano-structured blend and reactive extrusion. *Composites Science and Technology*, *200*, 108369. doi:10.1016/j.compscitech.2020.108369

Xie, J., Hse, C.-Y., De Hoop, C. F., Hu, T., Qi, J., & Shupe, T. F. (2016). Isolation and characterization of cellulose nanofibers from bamboo using microwave liquefaction combined with chemical treatment and ultrasonication.

Suan Sunandha Science and Technology Journal
©2022 Faculty of Science and Technology, Suan Sunandha Rajabhat University

Carbohydrate Polymers, *151*, 725-734.
doi:10.1016/j.carbpol.2016.06.011

Suan Sunandha Rajabhat University

Suan Sunandha Science and Technology Journals

SSSTJ

http://www.ssstj.sci.ssru.ac.th